Summer 8-20-2021

Quantifying Surface Changes on McMurdo Ice Shelf, Antarctica

Ann M. Hill
University of Maine, ann.hill@maine.edu

QUANTIFYING SURFACE CHANGES ON MCMURDO ICE SHELF, ANTARCTICA

By

Ann M. Hill

B.A. Skidmore College, 2018

A THESIS

Submitted in Partial Fulfillment of the

Requirements for the Degree of

Master of Science

(in Earth and Climate Sciences)

The Graduate School

The University of Maine

August 2021

Advisory Committee:

Kristin M. Schild, Research Assistant Professor of Earth and Climate Sciences, and Climate Change Institute, Advisor

Seth Campbell, Assistant Professor of Earth and Climate Sciences, and Climate Change Institute

Peter Koons, Professor of Earth and Climate Sciences, and Climate Change Institute

QUANTIFYING SURFACE CHANGES ON MCMURDO ICE SHELF, ANTARCTICA

By Ann Hill

Thesis Advisor: Dr. Kristin M. Schild

An Abstract of the Thesis Presented
in Partial Fulfillment of the Requirements for the
Degree of Master of Science
(in Earth and Climate Sciences)
August 2021

The amount of ice stored in Antarctica has the potential to raise sea level by almost 60 meters. Mass is primarily lost through glaciers draining the ice sheet and flowing into and ice shelves. Ice shelves float on the ocean and act as a resisting force to the flow of the glaciers, thereby modulating the flow of tributary glaciers, and consequently glacier contribution to global sea level rise. McMurdo Ice Shelf (MIS) buttresses four tributary glaciers, three of which will be discussed in this thesis, as well as the northwest corner of the faster flowing Ross Ice Shelf, which has tributary glaciers flowing from both East and West Antarctica. McMurdo Ice Shelf also serves as a runway for planes traveling to research bases on Ross Island. Therefore, if MIS were to thin, become unstable, or collapse, the results would not only impact the rate of sea level rise, but also Antarctic science logistics. This thesis quantifies changes in surface elevation and surface velocity to better understand the relationship between MIS and its tributary glaciers. I isolated the surface elevation change resulting from accumulation and ablation, and tracked ice shelf retreat across the study region. I differenced high resolution digital elevation models (DEMs, 2011 – 2015) in the Hut Point region of Ross Island, first correcting for errors introduced in DEM processing, and then removing the tidal and atmospheric pressures across the ice shelf region. These results revealed variable elevation change across the ice shelf (± 2 m) and across the ice on Hut Point Peninsula (± 5 m) as well as ice shelf front retreat (up to 1 km). While both the ice shelf thinning and the frontal

retreat contribute to the instability of MIS, the retreat is immediately concerning as it threatens to cut off Ross Island from the runways via Pegasus Road, thereby necessitating that a relocation of the road be considered. To further explore this system, I focused on evaluating velocity changes, and deriving strain rates across the glacier-ice shelf system on both seasonal and annual timescales by combining NASA velocity products with newly constructed geospatial velocity maps, utilizing Landsat imagery. These results revealed speeds as high as 225 m a^{-1} on the glaciers and 215 m a^{-1} on the ice shelf, with higher speeds occurring during the summer months. Two relationships between MIS and its tributary glaciers emerge: (1) seasonal velocity fluctuation of both the ice shelf and the tributary glacier, and (2) fluctuation of only MIS velocity and consistent velocity on the adjacent glaciers between seasons. These two relationships suggest spatial variability in the system's driving forces, and necessitate future work focusing on resolving these drivers. Results from this thesis are the first of their kind to use remote sensing to evaluate the relationship between tributary glaciers and MIS, and bridge a gap between *in situ* surveys and modeling projections.

ACKNOWLEDGEMENTS

First and foremost, I would like to thank my advisor, Dr. Kristin M. Schild for her constant support, guidance, and advice. I would also like to thank my committee member, Dr. Seth Campbell, for always encouraging me, and indulging my curiosity, regardless of how off-topic my question. I always value your patience while helping me. Also, thank you to my committee member, Dr. Peter Koons, especially for guiding me through strain rate calculations. I greatly appreciate your kindness, understanding, and how you always listen to my thought process and reasoning, even if the logic is false.

Thank you to Dr. Chris Gerbi for taking me on as a research assistant during my first year, despite my lack of background in Python.

Thank you to Dr. Laurie Padman for your assistance in running the Tidal Model Driver in the McMurdo Ice Shelf region to eliminate the tidal signal when differencing digital elevation models.

Thank you to my funding sources, the National Science Foundation Office of Polar Programs grant 1842021, and the University of Maine. Also, thank you to the Dan and Betty Churchill Exploration Fund, and the Geological Society of America Graduate Student Research Grant for providing funding for fieldwork in Patagonia, despite its cancelation due to COVID-19.

Thank you to Dr. Greg Gerbi, Dr. Meg Estapa, and Jennifer Cholnoky for your guidance, support, and encouragement in the graduate school application process, and for your work in preparing me for graduate school. You guys believed in me when I didn't, which has been more impactful than I could ever express.

Thank you so much to the amazing friends I have made here in Maine; I am so grateful for all of our adventures, dinners, and game nights, which helped foster a healthier work-life balance than I have ever had before. I am so lucky to have your support and encouragement, and I cannot wait for our future expeditions!

Finally, and most importantly, I am so fortunate to have parents as dedicated, kind, supportive, encouraging, and awesome as mine! Regardless of what wild idea I am pursuing, I know you will both do anything to see me succeed, whether it be studying abroad in a High Arctic archipelago of which you have never heard, or completing an extended backpacking trip. I don't know where I would be without you two, but I do know it would not be very far.

TABLE OF CONTENTS

LIST OF TABLES

LIST OF FIGURES

LIST OF ABBREVIATIONS

AASW	Antarctic Surface Water
CDW	Circumpolar Deepwater
COSI-Corr	Co-registration of Optically Sensed Images and Correlation
DEM	Digital Elevation Model
EAIS	East Antarctic Ice Sheet
GoLIVE	Global Land Ice Velocity Extraction
GPR	Ground Penetrating Radar
GSSI	Geophysical Survey Systems, Inc.
HPP	Hut Point Peninsula
ICESat-2	Ice, Cloud and land Elevation Satellite-2
InSAR	Interferometric Synthetic Aperture Radar
ITS_LIVE	Inter-Mission Time Series of Land Ice Velocity and Elevation
MEaSUREs	Making Earth System Data Records for Use in Research Environments
MIS	McMurdo Ice Shelf
NDLI	Normalized Difference Lake Index
NOAA	National Atmospheric and Oceanic Administration
RIS	Ross Ice Shelf
SAR	Synthetic Aperture Radar
TMD	Tidal Model Driver
TWTT	Two Way Travel Time
TZ	Transition Zone
WAIS	West Antarctic Ice Sheet

CHAPTER ONE

INTRODUCTION

1.1. Motivation: Why study ice shelf - glacier interactions?

As global average greenhouse gas concentrations continue to rise in the atmosphere, and consequently atmospheric temperatures, the scientific community expects to see continued sea level rise due to both thermal expansion and contribution from land-based ice. If all of the grounded ice on Earth melted, Antarctica would contribute 57.9 ± 0.9 m to sea level rise (Morlighem et al., 2020), Greenland would contribute 7.42 ± 0.05 m (Morlighem et al., 2017), and all other glaciers and ice caps would contribute 0.32 ± 0.08 m (Farinotti et al., 2019). Specific rates of sea level rise vary by source, and can range from 1.56 ± 0.33 mm a^{-1} (Frederikse et al., 2020), to 3.07 ± 0.37 mm a^{-1} (Cazenave et al., 2018). While current rates of sea level rise are dominated by contributions from smaller mountain glaciers and ice caps, Antarctica has the potential to contribute far more to raise sea level rise over a prolonged period of time than any other region (e.g. Bulthuis et al., 2019; DeConto & Pollard, 2016; Edwards et al., 2019; Hanna et al., 2020; Levermann et al., 2014; Meier et al., 2007; Pattyn & Morlighem, 2020; Zemp et al., 2019). Therefore, I focus this thesis on the controls of Antarctic sea level contribution.

The size of the Antarctic Ice Sheet is determined by its mass balance, which is calculated by subtracting the annual ablation from the annual accumulation (Rignot et al., 2008). The Transantarctic Mountains divide Antarctica. East Antarctic Ice Sheet (EAIS) has remained in a steady state, with some mass gain found around along the coast, while the discharge of the West Antarctic Ice Sheet (WAIS) has exceeded that of its surface accumulation (Rignot et al., 2019), resulting in a negative mass balance. The Ross Ice Shelf lies between WAIS and EAIS, and consequently drains ice from glaciers on both sides of the Transantarctic Mountains (Tinto et al., 2019). The location of Ross Ice Shelf makes it an essential component of the dynamics of this region.

Ice shelves form when glaciers flow off of their bedrock and float on the ocean, which must be cold enough so the ice does not immediately melt. Ice shelves play an essential role in reducing the amount of discharge from tributary glaciers by slowing their flow, thereby reducing the rate of mass transfer from land to sea. Following the retreat of ice shelves, glaciers can accelerate and drain mass rapidly. This relationship was observed following the collapse of the Larson A Ice Shelf, located on the northwest side of the Antarctic Peninsula, where its tributary glaciers underwent a 450% velocity increase over the following 8 months (Royston & Gudmundsson, 2016), thereby increasing the ice discharge rate and subsequent sea level rise. Ross Ice Shelf is the largest ice shelf in the world and drains much of WAIS, a marine-based ice sheet, meaning it rests on bedrock that sits below sea level (Horgan et al., 2011). As glaciers and ice shelves interact as a system, changes in one location can propagate, altering the behavior up-glacier or down-glacier onto the ice shelf, a process known as teleconnection (Reese et al., 2018). As most of WAIS is marine-based, when water flows between the ice and the bed, the ice floats on the water, prying the ice apart from the bed, which consequently allows more water to flow farther under the ice and floating more of the glacier. This compounding process is known as a positive feedback loop, and the resulting reduced bed coupling enhances the effects of up-glacier teleconnections (Reese et al., 2018). Glaciers and ice shelves are highly responsive to small changes in their environment, such as increasing oceanic or atmospheric temperatures. Due to this sensitivity, quantifying the relationship between ice shelves and their tributary glaciers is vital in understanding future sea level rise. In this thesis, I explore the relationship between McMurdo Ice Shelf (MIS) and its tributary glaciers.

1.2. Background: The ice shelf - glacier system

As ocean and atmospheric temperatures continue to increase, the contribution of glaciers to the mass balance of ice shelves is of particular importance. While glacier contribution may help to thicken and stabilize ice shelves, once ice flows from tributary glaciers across the grounding line into the ice shelf, that mass contributes to sea level rise. Many external environmental factors can affect the interplay between ice

shelves and glaciers, and these operate on timescales ranging from daily to decadal. Drivers of short-term fluctuations include tides and atmospheric pressure, which can cause velocity and elevation shifts over a matter of hours or days. Annual-scale impacts include precipitation, surrounding sea ice concentrations, ocean current variability, and atmospheric and oceanic temperature changes. Decadal-scale, and longer, impacts on the behavior of glaciers and ice shelves include the Pacific decadal oscillations, which influence the ocean temperature at the ice-ocean interface (Rignot et al., 2019). These factors can contribute to changes to the glacier-ice shelf system on seasonal to annual timescales, and are highlighted in the remainder of section 1.2.

1.2.1. Force balance in an ice shelf – glacier system

The ice shelf helps to buttress its tributary glaciers by, together with the ocean, providing a resisting force against the driving force of the glacier, ultimately slowing the glacier's velocity (Fig. 1.1). Therefor the thicker and larger the ice shelf, the more effective it will be at reducing mass transfer from land to ice shelf (Fig. 1.1 A). When ice shelves shrink due to mass loss, the resisting force that acts against the driving force of the glacier decreases, allowing the glacier velocity to increase (Fig. 1.1 B). Finally, when the ice shelf is absent, the ocean provides the only resisting force against the flow of the glacier, and the glacier velocity increases further (Fig. 1.1 C). Mechanisms of mass loss include the sub-ice shelf circulation of warm ocean water, as well as surface melt resulting from above-freezing atmospheric temperatures (Fig. 1.1 D). Even though changes in the size and dynamics of an ice shelf indicate future changes in the velocity and mass balance of the tributary glaciers, uncertainties exist surrounding how much ice shelf change is required to incite changes in the glaciers, and what facets of change are the most impactful. Therefore, this thesis focuses on quantifying changes across the McMurdo Ice Shelf (MIS) and its tributary glaciers using remote sensing techniques.

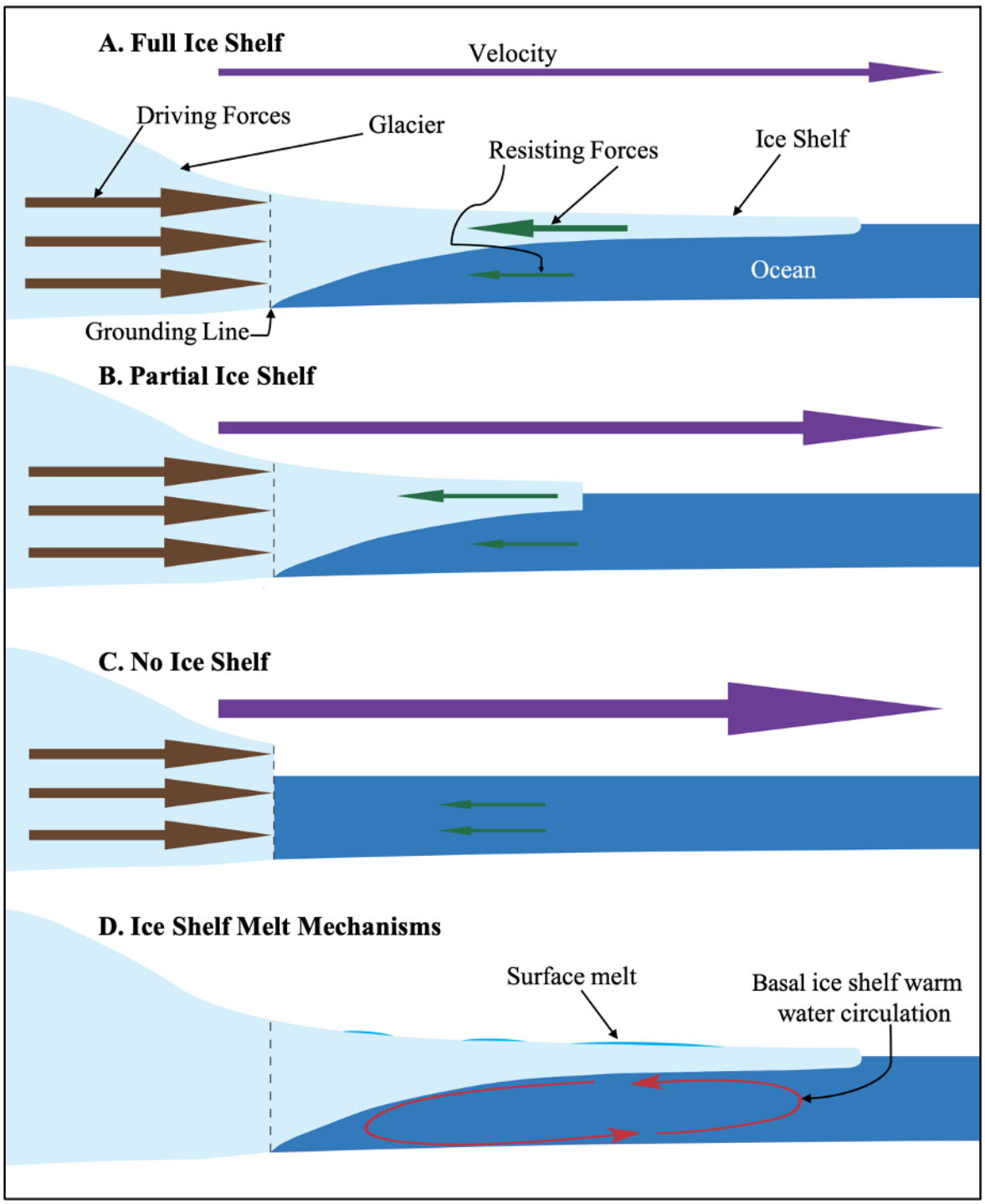

Figure 1.1. Driving versus resisting forces in a simple glacier-ice shelf system. Ice shelves act as a buttress to glaciers. Together the ice shelf and the ocean act as resisting forces (green arrows) against the driving force (brown arrows) of the glacier. As shown in the full ice shelf scenario (A), the velocity of the glacier is relatively slow due to the large ice shelf. In the partial ice shelf scenario (B), some of the ice shelf has disintegrated, reducing the resisting force and increasing the glacier velocity. When no ice shelf remains (C), the ocean provides the only resisting force, and the glacier velocity increases more. Also shown are mechanisms of ice shelf melt (D) including basal ice shelf melt due to warm water circulation, and high

summer surface melt due to intrusion of Antarctic Surface Water (AASW) and high quantities of surface sediment.

1.2.2. Oceanic and atmospheric forcings

Warming of both the ocean and the atmosphere is tied to glacier acceleration and retreat, as seen in the Antarctic Peninsula where glaciers in the southwest experience more retreat than those located in the northwest (Cook et al., 2016). This difference in glacier behavior results from the southernmost Antarctic Peninsula glaciers interacting with the warmer Circumpolar Deepwater (CDW), while those in the north experience the colder surface water circulation (Cook et al., 2016). Spence et al. (2017) attribute this warming to changes in wind patterns reducing circulation and trapping warm water along the coast. Additionally, not all glaciers along the Antarctic Peninsula have ice shelves, making those more vulnerable to change in response to oceanic conditions.

1.2.3. Tidal influence

Tides can impact the behavior of glaciers and ice streams from the terminus to over 80 km up glacier from the grounding line through dynamic coupling (Anandakrishnan et al., 2003; de Juan et al., 2010). Observations of glacier dynamics in relation to tides suggest that ice shelves and ice streams behave as a single system, where changes in the tidal height incite changes in the glacier velocity (Brunt et al., 2010; Doake et al., 2002). However, there is a lag between peak ice shelf velocity values and the maximum and minimum tidal heights. The ice shelf reaches its maximum velocity after the maximum tide height, as the tide is dropping, and the glacier reaches its minimum velocity after the minimum tide height, as the tide is rising. This delay is also observed as far as 80 km up glacier from the grounding line (Anandakrishnan et al., 2003). Additionally, higher strain rates measured near the front of the glacier, in comparison to those up glacier, indicate that the tidal effects become muted when moving farther from the terminus (Podolskiy et al., 2016). Conversely, on Greenland glaciers the maximum tidal velocity often occurs at low tide, instead of partway between falling and rising tide, suggesting this difference is associated with the presence of

large ice shelves in Antarctica that are absent in Greenland (Sugiyama et al., 2015). Overall, the ice shelves appear to buffer the tributary glaciers, acting as a barrier between the ocean and the glaciers, delaying the impact of the tides on the tributary glaciers.

1.3 Present state

While at present Antarctica is not the main contributor to sea level rise, the previously mentioned forcings do contribute both to its behavior and its mass balance. From 1993 – 2018, Antarctica contributed 0.25 mm a^{-1} to sea level rise out of 3.07 ± mm a^{-1} total annual sea level rise for this period (Cazenave et al., 2018), and from 2012 – 2016 Antarctica contributed 0.53 mm a^{-1} to sea level rise, 0.48 mm a^{-1} of which originated in West Antarctica (Bamber et al., 2018). As the Antarctic atmospheric temperature is almost always below freezing, surface melt comprises a very small portion of the mass loss from Antarctica, and most mass loss stems from mass transfer across the groundling line (Bamber et al., 2018). However, the small amount of surface melt that does occur can have other negative impacts on the glacier-ice shelf system. For instance, surface melt decreases the albedo, meaning more energy is absorbed by the surface and less is reflected back to the atmosphere than snow or ice. In East Antarctica, the lower albedo caused by surface melt makes it approximately three times easier for further melt to follow (Jakobs et al., 2019). Additionally, when the water refreezes, the snow has a lower albedo than the new snow (Jakobs et al., 2021). Surface meltwater can also incite hydrofracturing. As water is slightly denser than ice, if surface melt is sustained its pressure can propagate cracks to the glacier bed (van der Veen, 2007). Therefore, on ice shelves, hydrofracturing can accelerate calving (DeConto & Pollard, 2016), a process believed to have contributed to the breakup of Larson B Ice Shelf (Banwell et al., 2013; Scambos, 2004). Furthermore, the fastest Antarctic ice velocities are found along the coast on ice shelves (600 m a^{-1} – 1000 m a^{-1}) and outlet glaciers (300 m a^{-1} – 600 m a^{-1}), while the slowest velocities are towards the center of the continent (near 0 m a^{-1}). These high velocities result in rapid mass loss into the ocean, and increased surface melt would only amplify this process.

1.4. Thesis overview

1.4.1. Study site

For this thesis, I will focus on ice shelf-glacier interactions at McMurdo Ice Shelf, a critical and vulnerable location in Antarctica. The McMurdo Ice Shelf covers ~1,500 km^2, borders the Transantarctic Mountains to its west (Banwell et al., 2017), and provides a buttress to four glaciers, Koettlitz, Terror, Aurora, and Skelton, as well as the northwest corner of the much larger Ross Ice Shelf (~500,809 km^2) (Fig. 1.2; Rignot et al., 2013). In comparison to other ice shelves in Antarctica, MIS is relatively thin, varying greatly from approximately 6-200 m across the ice shelf (Arcone et al., 2016; Campbell et al., 2017; Glasser et al., 2006). MIS also experiences unusually high surface melt, reaching four times that seen on other Antarctic glaciers, but experiences little calving (Glasser et al., 2006). The upward direction of ice flow around Black Island transports basal sediment to the surface, which is then further exposed by ablation, leading this area to have the highest sedimentation rates across the ice shelf (Glasser et al., 2006). During the summer season, approximately 25% of the surface becomes flooded with streams and ponds, mostly concentrated in this area (Glasser et al., 2006). The surface hydrology redistributes the debris across the ice shelf (Glasser et al., 2006). Conversely, high accumulation rates, up to 1.5 m a^{-1}, are found in Windless Bight, near the grounding lines of Terror Glacier and Aurora Glacier (Fig. 1.2; Heine, 1967).

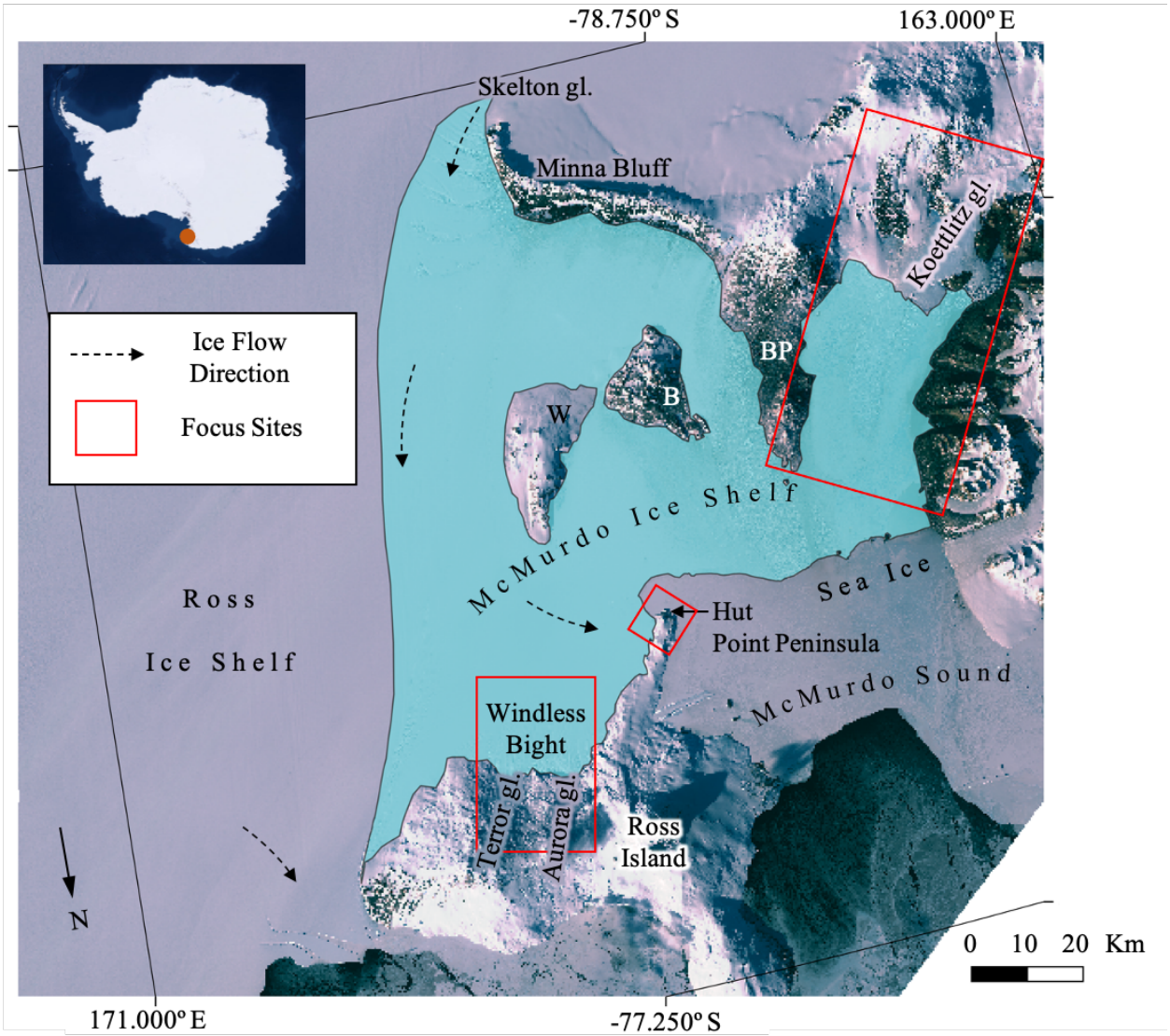

Figure 1.2. Map showing study region and focus study sites with major geographic points noted. The MIS (inset, orange circle; turquoise shading) is bound by the Ross Ice Shelf, and McMurdo Sound. Noted are the locations of White Island (W), Black Island (B) and Brown Peninsula (BP). The red boxes define the focus study sites of Terror and Aurora Glaciers flowing into Windless Bight, Hut Point Peninsula, and Koettlitz Glacier and its adjacent ice shelf. Ice flow directions are denoted by dashed arrows (Campbell et al., 2017) with tributary glaciers (gl.) labeled. Background image from Sentinel-2, collected on 11 October 2019.

While MIS can be difficult to measure, the existing research concludes that MIS is particularly vulnerable to collapse, more so than any area of RIS (Rack et al., 2013; Stern et al., 2013; Tinto et al., 2019). If MIS collapses, a potential retreat of RIS could follow. This reliance on MIS by RIS for stability is particularly concerning because RIS buttresses both East and West Antarctic drainage basins. Furthermore, modeling found MIS to experience tele-buttressing, whereby ice shelf thinning induces immediate acceleration of

MacAyeal and Bindschadler Ice Streams over 900 km away, across the grounding line (Reese et al., 2018). Currently, the thickness, and therefore a component of the resistive force of MIS, is controlled by the balance of mass input from tributary glaciers and melt from oceanic and atmospheric forcings. However, recent studies have found inconsistent results concerning thinning rates of the MIS region collected using the same airborne radar program, suggesting challenges in data interpretation. Tinto et al. (2019) found that warm sub-ice shelf circulation results in summer melt rates of 10 m a^{-1} in the MIS region, while the neighboring RIS predominantly experiences summer melt rates of <2 m a^{-1}. Das et al. (2020) isolated the basal melt rate, and calculated a loss of <2 m a^{-1} in the MIS region; however, they also calculated a negative strain rate around Ross Island and Minna Bluff, suggesting contraction, which is typically found in conjunction with ice shelf thickening.

High submarine melt rates found on MIS result from the intrusion of warm AASW, which is found in the top of the water column and can flow under the thinner MIS, but not the thicker RIS (Tinto et al., 2019). If the MIS were to collapse, there would no longer be a buffer between the warm ocean intrusion and Ross Ice Shelf, therefore providing a more direct route to RIS, potentially threatening its stability. During the summer, warm surface water is pulled under the MIS from the east, causing ocean-induced basal melting (Heine, 1967). Melting also occurs in the upper part of the water column from wind and the tides pushing warm surface water against the ice shelf front (Stern et al., 2013). At mid-depths along the front of the ice shelf, CDW intrudes, which can be 4° C warmer than the melting point at the bottom of the water column (Stern et al., 2013). Melting at depth results from highly saline surface water forming as a result of brine rejection during sea ice formation (Stern et al., 2013). This warmer, dense water sinks into the colder, deeper water where it sits adjacent to the ice shelf, at its pressure melting point. During the winter, the opposite occurs. Surface water moves northward, away from the MIS, resulting in upwelling of supercooled basal water, which refreezes to the underside of the ice shelf (Rack et al., 2013).

McMurdo Ice Shelf is also logistically important for both the U.S. Antarctic Program and the New Zealand Antarctic Program, whose bases (McMurdo Station and Scott Base, respectively) lie adjacent to MIS on Ross Island. The ice runways on MIS are the primary access point for the two bases, with Pegasus Road connecting the runways to Ross Island. Due to the complex positioning, Pegasus Road crosses the boundaries between MIS, sea ice, and Ross Island. This region of Pegasus Road experiences folding and faulting, which forms as the ice shelf buttresses against the sea ice and rock. Thinning of MIS could lead to retreat and destabilization of MIS, ultimately threatening the logistics of these two field programs.

1.4.2. Research questions

The behavior of Koettlitz, Terror, and Aurora Glaciers is modulated by MIS, and therefore, their longevity is interconnected. However, few studies examine changes in glacier dynamics from a coupled glacier-ice shelf behavior perspective (Smith et al., 2020). In this thesis, I will address this gap by answering the question, *what is the relationship between both surface elevation and surface velocity on the tributary glaciers and McMurdo Ice Shelf?* To answer this question, I will address the following specific objectives:

1. Quantify large-scale spatial elevation by calculating the change in elevation over time on MIS and Ross Island

2. Quantify changes in the glacier-ice shelf relationship by establishing a time series of surface velocity and strain rate of MIS and tributary glaciers

Each objective will be addressed in its own chapter of this thesis, as outlined in the following section.

1.5. Thesis structure

This thesis consists of an introduction chapter (Chapter one), two scientific papers (Chapters two and three), a summary and next steps chapter (Chapter Four), a complete list of references used throughout this thesis, and an appendix with the remainder of data not included in the scientific papers. The two scientific papers

are presented in their submitted (Chapter two) or in preparation (Chapter three) versions. The only modifications to the papers were those needed to comply with the University of Maine Graduate School thesis requirements: the references for each paper have been combined into one complete list of references for this thesis, and figure captions, chapter sections, and the in-text citation formatting is uniform throughout the thesis. Each of the two scientific chapters begins with an abstract, and follows the common journal format of an introduction, methods, results, discussion, conclusion, and acknowledgements. Below are the summaries for each scientific chapter.

1.5.1. Chapter two

Chapter two, "Recent Stability of the McMurdo Ice Shelf and Hut Point Peninsula Glaciers in West Antarctica", uses a combination of remote sensing imagery, *in situ* measurements, and modeling results to identify changes in the McMurdo Ice Shelf region, and how the stability could impact Hut Point Peninsula based logistics. This study used Digital Elevation Models (DEMs), from the Polar Geospatial Center for 2011 and 2015, to quantify ice thickness changes across MIS and Hut Point Peninsula. Given that this region is critically important for the operation of the US and New Zealand Antarctic bases, and is a region in flux, additional *in situ* surveys were performed as reconnaissance for the potential rerouting of the current ice road. The *in situ* surveys and numerical models investigated the ice shelf stability at a structural level. The *in situ* surveys included Ground Penetrating Radar (GPR) profiles collected adjacent to the current ice road to measure ice structure, and GPS velocity surveys in the same region. Using these *in situ* measurements, a numerical model was established to evaluate the long-term stability and maintenance of this proposed new road region. Major findings of the project showed variable thinning of the ice shelf in this region, and substantial retreat of the ice shelf front adjacent to Hut Point Peninsula between 2011 and 2015, ultimately threatening the longevity of the current Pegasus Road.

This manuscript was submitted to the peer-reviewed journal *Cold Regions Science and Technology* on 23 April 2021. My co-authors are Dr. Seth W. Campbell and Dr. Kristin M. Schild, both at the University of

Maine. This chapter includes information on the method I developed to difference DEMs across McMurdo Ice Shelf and Hut Point Peninsula. I was responsible for developing the differencing method, as well as differencing the DEMs, conducting error analysis, creating some of the figures, and writing the scientific portion of the manuscript. Dr. Campbell collected and processed the *in situ* measurements (GPR and GPS), created and ran the numerical model, and wrote the resulting CRREL technical report. Dr. Schild combined the technical report and the scientific portion into a cohesive manuscript, updated figures, and oversaw the DEM differencing method development. The manuscript is currently in review.

1.5.2. Chapter three

The third chapter, "Quantifying Temporal and Spatial Surface Velocity Changes Across the McMurdo Ice Shelf System", further explores the relationship between ice shelves and their tributary glaciers through quantifying the surface velocities and strain rates of Terror, Aurora, and Koettlitz Glaciers and their adjacent ice shelf regions. McMurdo Ice Shelf helps buttress a region of the much larger Ross Ice Shelf, making it vital to understand the region's flow regime through time. I calculated the surface velocity using Landsat 8 imagery spanning 2013 – 2020 with the program COSI-Corr, and also used existing surface velocity datasets (GoLIVE and ITS_LIVE) to capture the surface velocity across the glacier-ice shelf transition. Additionally, I captured changes in glacier surface flow by calculating the strain rate in the study regions using the COSI-Corr surface velocity results. Together, these pieces of information provide insight into the stability of this system and how it is evolving over time. Main findings include higher velocity values in the Terror and Aurora region than the Koettlitz region, greater velocity values in the summer than the winter, and more annual variability in the velocity values calculated on the ice shelf than those calculated on the glaciers. This manuscript will be submitted to a peer-reviewed journal following additional edits.

CHAPTER TWO

RECENT STABILITY OF THE MCMURDO ICE SHELF AND HUT POINT PENINSULA GLACIERS IN WEST ANTARCTICA

2.1. Abstract

McMurdo Ice Shelf (MIS) and associated land masses act as lateral margins and pinning points, respectively, to Ross Ice Shelf in West Antarctica. Thinning or collapse of MIS could therefore have sizeable detrimental teleconnections across West Antarctica. The collapse of MIS would also be catastrophic to Antarctic research logistics, as both the United States and New Zealand Antarctic Programs operate on MIS and the adjacent Hut Point Peninsula (HPP) of Ross Island. Here, we assess the vulnerability of the MIS and HPP regions by calculating recent ice surface elevation change using Worldview-derived digital elevation models acquired between 2011-2015. We also use ground-penetrating radar and GPS surveys in 2015-2016 to calculate glacier ice thickness and flow velocities of the glacierized HPP Transition Zone (TZ) hillside which is being considered as a new access road between MIS and HPP that both Antarctic programs would rely upon. Results show ice thinning across the TZ Hillside southeast-facing slope on HPP, and no change to moderate thickening on the TZ Hillside northwest-facing slope. Surface lowering also occurred on southern MIS near its terminus, whereas minimal change occurred on MIS near Ross Island. We attribute the complicated elevation changes to spatial variability of surface melt and accumulation. Broader surface velocity measurements and oceanographic observations are needed to rule out the influence of dynamic thinning, thickening, or basal melt. However, our preliminary results suggest moderate concern for long-term stability near the terminus of MIS.

2.2. Introduction

Ice shelves, floating ice tongues extending from a grounded tidewater glacier, surround over 75% of Antarctica's coastline (e.g., Rignot et al., 2013) and provide critical stability to the Antarctic Ice sheet primarily through tributary glacier buttressing. Due to their flat, thick nature, ice shelves can also be a pivotal logistic resource, serving as a runway for large planes (e.g., Haehnel et al., 2019), a road for overland convoys (e.g., Lever & Thur, 2014), and a staging location for scientific operations (e.g., Millan et al., 2013). McMurdo Ice Shelf (MIS) is one such location that is critical for both glacier stability and field logistics. Skelton, Terror, Aurora, and Koettlitz Glaciers are all buttressed by MIS, which also acts as a lateral shear margin to the adjacent Ross Ice Shelf (RIS), which drains both East (EAIS) and West Antarctic Ice Sheets (WAIS). The thinning or collapse of MIS could trigger a retreat of the RIS, inducing thinning and potential acceleration of ice streams over 900 km away (e.g., MacAyeal and Bindschadler Ice Streams; Reese et al., 2018). MIS also serves as the primary logistics hub for the United States (McMurdo Station) and New Zealand (Scott Base) Antarctic Programs (Fig. 2.1). Therefore, due to the prominent role of MIS in both ice sheet stability and Antarctic infrastructure, understanding the stability of MIS is critically important.

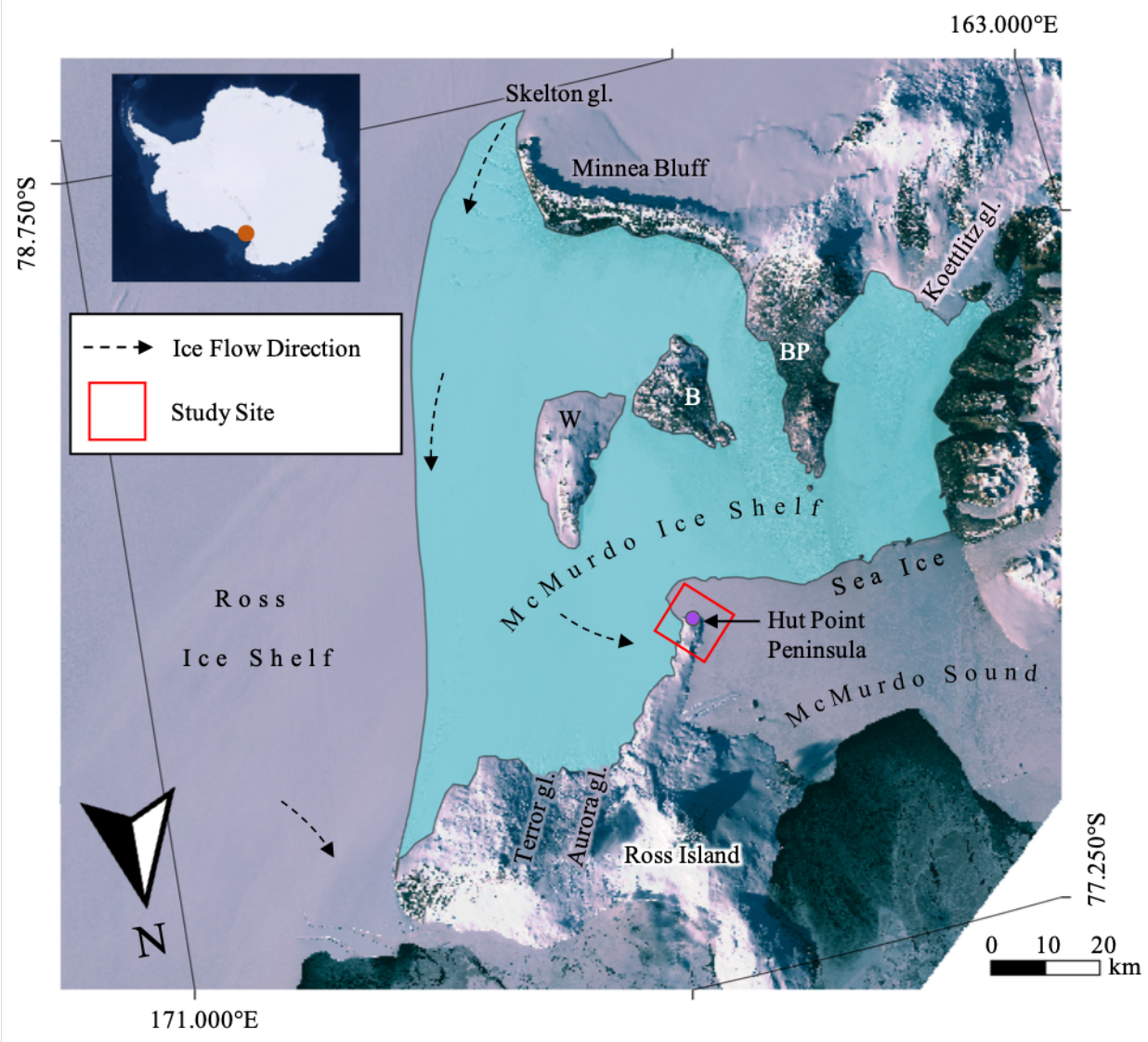

Figure 2.1. Map showing study region and focus study sites with major geographic points noted. The McMurdo Ice Shelf (MIS) and Hut Point Peninsula (HPP) study region (inset, orange circle), where MIS (turquoise shading) is bound by the Ross Ice Shelf, and McMurdo Sound. Noted are the locations of the NOAA AWS (purple circle), White Island (W), Black Island (B) and Brown Peninsula (BP). Ice flow directions are denoted by dashed arrows (Campbell et al., 2017) with tributary glaciers (gl.) labeled. Background image from Sentinel-2 on 11 October 2019.

The stability of an ice shelf is directly related to its margins and its mass balance. Lateral ice shelf margins resist ice flow either by friction against bedrock or via lower moving lateral ice (e.g. MacGregor et al., 2012). Therefore, thinning or collapse of these margins decreases or removes a primary resistance to ice flow. Ice shelves also resists tributary glacier flow by providing a buttressing force, therefore any reduction in ice shelf mass results in a decrease in buttressing force, and can enable up-glacier tributary glacier

speedup and dynamic thinning (e.g. Scambos et al., 2004; Hulbe et al., 2008). Ice shelf mass gain in Antarctica occurs through snowfall, tributary glacier discharge, and basal freeze-on of marine ice. Unfortunately, most ice shelves in Antarctica are losing more mass than they are gaining, primarily through a complex combination of calving icebergs, surface melting, and basal melting (e.g. Depoorter et al., 2013; Rignot et al., 2013; Bell et al., 2017; Kingslake et al., 2017; Smith et al., 2020). While ice shelves can range in thickness from 2000 m at the grounding line to 100 m at the ice shelf terminus, the MIS is thinner than most, ranging between ~6–200 m thick (Glasser et al., 2006; Campbell et al., 2017). Additionally, the MIS is particularly susceptible to basal melting due to the routing of warm AASW directly under this region (Rack et al., 2013; Stern et al., 2013; Tinto et al., 2019). This AASW routing results in melt rates of MIS (~10 m a^{-1}) being disproportionately high in comparison to the neighboring RIS (<2 m a^{-1} at RIS; Tinto et al., 2019). Additionally, MIS experiences unusually high surface melt, spatially ranging from 43–441 mm w.e. during a summer melt season, resulting in approximately 25% of the region around Black Island becoming flooded with streams and ponds during this time (Glasser et al., 2006). Concerningly, a thinned ice shelf with abundant surface water may not require much tidal flexure to bypass a rapid disintegration threshold (Banwell et al., 2013; Banwell et al., 2019). As atmospheric and oceanic temperatures continue to warm, continued evaluation of MIS stability is essential for both scientific and logistic concerns.

Several “single-point failures” in the MIS-HPP system would jeopardize the feasibility of using MIS and HPP for U.S. and New Zealand Antarctic logistics (Augustine et al., 2012). One such failure would be reduced access between HPP, where Scott Base and McMurdo Station are located, and MIS, where all runway and aircraft operations are located. Currently, the primary road connecting MIS to HPP is by the Pegasus Ice Road, which crosses the Transition Zone (TZ) (Fig. 2.2, blue arrows). The TZ is a triaxial point of stress where MIS buttresses against HPP at the ice shelf–sea ice transition. This buttressing of ice leads to compression folds, severe fracturing, and complex ice dynamics (Campbell et al., 2017; Fig. 2.2). Meltwater runoff from the nearby hillside of HPP has caused severe ponding in the TZ. Although the ponding is partially alleviated by drain holes into the relatively porous fractured ice shelf (Shoop et al.,

2014), the subsurface influence of meltwater on the ice, and complex dynamics in this area, are concerning for long-term stability and longevity of Pegasus Ice Road.

In this study we analyze recent rates of ice elevation change across the TZ and surrounding region and explore a proposed new road location on the TZ Hillside which would link MIS with HPP and replace Pegasus Ice Road in the event the current route becomes unpassable (Fig. 2.2, white line). To address changing conditions and determine if there is any evidence of instability, we difference satellite-derived digital elevation models (DEMs) collected several years apart to spatially measure elevation changes (inferring ice thickness changes) across HPP and MIS. To explore the proposed new road location on the TZ Hillside, we completed ground-penetrating radar (GPR) and GPS surveys to measure ice thicknesses and ice flow velocities, respectively. We then used three-dimensional finite element numerical modeling to calculate ice flow flux on the TZ Hillside and estimate potential ice flow impacts to the proposed new road location.

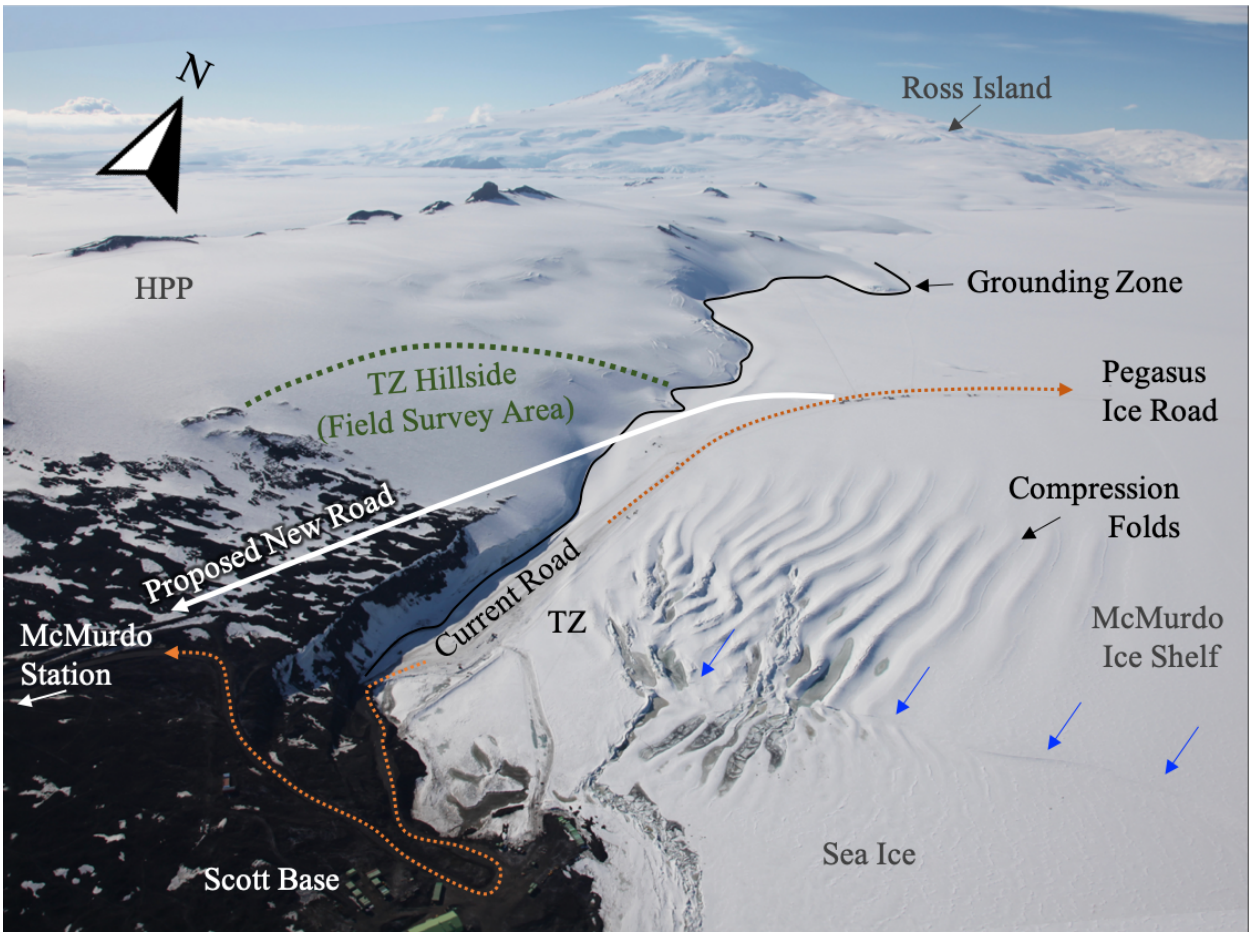

Figure 2.2. Airborne image of Hut Point Peninsula (HPP), part of Ross Island. Noted are the locations of the transition zone (TZ), the McMurdo Ice Shelf (MIS) terminus (blue arrows), the grounding zone (black solid line), the Pegasus Ice Road (orange dotted line), which is the current road from MIS onto HPP, the proposed new road between MIS and HPP (white solid line), and the GPR and GPS field survey area on the TZ Hillside (green dotted area).

2.3. Methods

2.3.1. Ice thickness changes

To quantify the change in ice thickness across HPP and MIS, we differenced two WorldView DEMs, collected on 6 February 2011 and 25 November 2015. In order to isolate variability in the TZ region due solely to changes in ice thicknesses, we removed confounding variables, including tidal phase and amplitude, atmospheric pressure, and shifts in the DEM during processing (e.g., Kulshrestha et al., 2020). To account for these contributing variables, we developed a processing method using remote sensing

imagery, numerical modeling, and *in situ* data, which is schematically depicted (Fig. 2.3) and described in the following sections (2.2.1.1. – 2.2.1.3.).

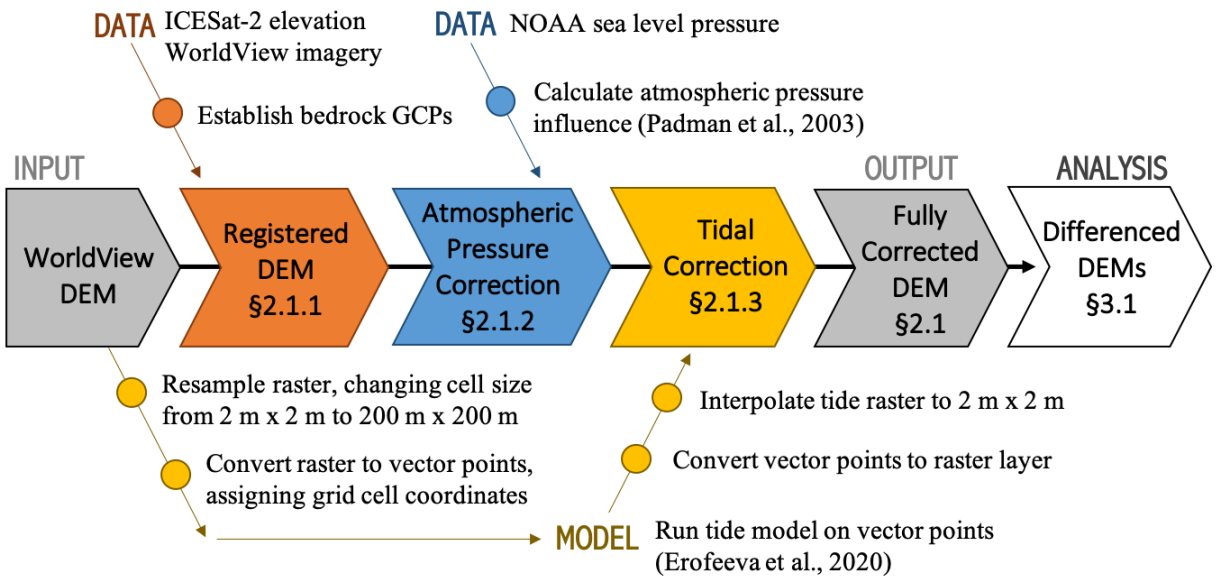

Figure 2.3. Schematic diagram outlining the steps and data sets used in the developed method to correct each DEM prior to differencing. This method accounts for variability in DEM processing (orange), and differences in atmospheric pressure (blue) and tidal amplitude (yellow) between DEMs.

2.3.1.1. Vertical DEM correction

We used DEMs developed by the Polar Geospatial Center (Saint Paul, Minnesota, USA), where stereo methods were applied to commercially available WorldView-2 (2011 and 2015) and Worldview 3 (2015) satellite imagery. During DEM processing, a vertical offset can be induced by a DEM shift (Nuth & Kääb, 2011). To correct for this, we established a series of bedrock ground control points (GCPs) across the study area using ICESat-2 (ATL06) as our vertical datum reference frame (method as in Nuth & Kääb, 2011). We selected ICESat-2-derived GCPs in regions of exposed bedrock in low slope terrain (defined as a single pixel, and the surrounding eight pixels, all measuring slopes ≤ 5°), as steeper slopes are associated with vertical errors > 1 m (Harding et al., 1994). We used these GCPs (3–4 per DEM) to calculate the average

offset between the ICESat-2 elevation and DEM elevation (2011: 1.59 ± 0.1 m; 2015: 3.46 ± 0.1 m), then vertically adjusted the DEMs to more closely match the ICESat-2 vertical datum reference frame.

2.3.1.2. Atmospheric pressure correction

The freeboard of a freely floating ice shelf is impacted by changes in atmospheric pressure. To remove the impact of atmospheric pressure, we used the ice shelf correction established in Padman et al. (2003), where a pressure difference of 1 hPa between the measured value and standard atmospheric pressure (1013.25 hPa) results in 0.82 cm adjustment in elevation. To determine atmospheric pressure, we used the National Oceanic and Atmospheric Administration's (NOAA) National Centers for Environmental Information site (https://www.ncei.noaa.gov/products), located adjacent to McMurdo Station (Fig. 2.1, purple circle), at the closest measurement in time (± 24 min) to the average image collection date. We then adjusted the ice shelf in each DEM to standard atmospheric pressure.

2.3.1.3. Tidal correction

Ice shelf elevation is also impacted by the tidal signal; without correction, differences in tidal phase and amplitude between DEM collection periods would result in erroneous measurements of ice shelf thickness change. To remove the tidal signal from each DEM, we calculated the tidal height and phase using the Tidal Model Driver (TMD) (Erofeeva et al., 2020) CATS2008 model and then subtracted the tide from the ice shelf region of each DEM scene. As each DEM is a compilation of several individual scenes, and therefore several tidal heights and phases, we tested two methods to establish a single representative tidal correction for each DEM. In the first method, we calculated the tidal height and phase using the average collection time of the contributing images (6 contributing images for 2011; 30 contributing images for 2015), calculated the tidal height and phase for the average time, and then adjusted the DEM based upon the output tidal height. In the second method, we calculated the tidal height and phase for each contributing scene and then averaged the tidal corrections and applied the average correction to each DEM. In comparing the two

approaches, we found the tidal corrections to be nearly identical (± 0.00335 m), therefore we use the former method as it involves fewer steps and opportunities to propagate uncertainties. Additionally, due to the small degree of spatial variability in the tidal signal ($\leq$ 0.0055 m over 159 km^2), we ran the tidal height model at a down-sampled (200 m) spatial resolution to expedite tide and atmosphere corrections. After the TMD model produced a tidal height for each ice shelf pixel, we then applied a nearest neighbor interpolation to acquire tidal height at a spatial resolution of 2 m, matching the spatial resolution of the original DEMs. We then applied the correction, thus removing the tidal signal from the ice shelf portion of the DEM.

2.3.2. Subsurface ice structure

To measure the subsurface structure of Pegasus Ice Road and evaluate the possibility of relocating the road to the TZ Hillside, we performed GPR surveys in both of these regions. We collected three 840 m parallel GPR transects (2.5 km total), spaced ~10 m apart, on Pegasus Ice Road in January 2016 using a 400MHz antenna, as well as four parallel and one cross-cutting transect on the TZ Hillside in November 2016 (5.5 km of 100 MHz and 4.7 km of 400 MHz). To perform these GPR surveys, we used a Geophysical Survey System Incorporated (GSSI) SIR-4000 control unit coupled with a GSSI model 3207AP 100 MHz antenna and GSSI model 50400 400 MHz antenna. We recorded scans for 1000–1400 ns, with a two-way travel time (TWTT) at 24 scans s^{-1}, and 2048 samples per scan. High and low pass finite impulse response filters were used during data collection; between 100–800 MHz for the 400 MHz antenna and between 25–300 MHz for the 100 MHz antenna. The GPR was synced with a handheld Garmin GPSMap78, recording GPS position at 1 Hz. The GPR antennas were hand-towed at approximately 0.25 m s^{-1} resulting in traces approximately every 1 cm and GPS positions every 0.25 m. Estimated horizontal precision of GPR profiles from the handheld GPS was ±2 m.

To convert TWTT to depth, we first calculated the velocity of the radio waves through the substrate, using the equation, $V = \frac{c}{\sqrt{\dot{\varepsilon}}}$, where $\dot{\varepsilon}$ is permittivity, V is the radio wave velocity in m ns^{-1}, and c is the speed of light. For depth calibration of the Pegasus Ice Road and the TZ Hillside, we used different values for

permittivity ($\dot{\varepsilon}$) as the surface types varied from snow and firn (Pegasus Ice Road) to solid ice (TZ Hillside). For the Pegasus Ice Road transects, we used a permittivity value of 2.8, based on depth-density results from a shallow core collected within the TZ region (Campbell et al., 2017), which shows that dense firn ($\dot{\varepsilon}$~ 2.2) is overlying meteoric and marine ice ($\dot{\varepsilon}$~3.1). For the TZ Hillside, we used the relative permittivity of ice ($\dot{\varepsilon}$ = 3.1) for depth calculations, as the TZ Hillside was primarily composed of bare ice with only 20–50 cm of snow cover. Based on the TWTT and calculated wave velocity (0.169–0.179 m ns^{-1}), we recorded ~60 samples per m depth, which is more than sufficient for a smooth waveform given the frequencies used. The GPR profiles were processed using GSSI commercial software (RADAN v. 7.0), and processing included time-zero correction, horizontal filtering to remove ringing, and stacking to improve signal-to-noise ratios and visualization of englacial structure.

2.3.3. TZ Hillside ice velocity

2.3.3.1. *In situ* surveys

To calculate regional ice velocity and rates of deformation at a potential site for a new road, we placed 22 bamboo stakes (2 m in length) in a grid configuration on the TZ Hillside. Stakes were installed by hand drilling 1m holes using a Kovacs auger. We then performed a kinematic GPS survey using a roving Trimble NetR7 and Zephyr Geodetic Antenna unit, with an identical geodetic GPS base station established at McMurdo Station (2–2.6 km from survey grid). We first surveyed the stakes on 12–15 November 2016 and then resurveyed the stakes on 2 January 2017 (47–51 days between surveys). Using changes in position, we estimated ice flow velocities and rates of deformation for this TZ Hillside region. Systematic position uncertainty from the processed baselines was 1.9 ± 0.01 cm in the horizontal and 4.7 ± 1.9 cm in the vertical. We also assumed 1 cm of bias uncertainty due to the stake hole size relative to the distance measured and leveling of the survey rod. Combining systematic and bias uncertainty, our total horizontal positional error is 2.1 cm at each measurement.

2.3.3.2. Numerical modeling

To better resolve the rates of deformation on the TZ Hillside, and determine the region's suitability for a new road, *in situ* GPS and GPR measurements were used to constrain a three-dimensional numerical model. We used surface elevation and ice thickness measurements from the GPS and GPR surveys, respectively, to develop raster layers, which we merged to constrain top and bottom surfaces of a finite element numerical model in COMSOL Multiphysics (v. 5.2a). Model boundary conditions included a no-slip (frozen) bed, normal surface stress, and open boundaries at the inlet (top of the hillside) and outlet (bottom of the hillside near the grounding zone). We set the model to have minimal snow and/or firn cover, which allowed for a constant density (ρ) of ice, and used a cold-ice viscosity (μ) of ~1×10^{15} Pa s (Marshall, 2005). Given the prescribed boundary conditions and rheology, ice flow was driven by gravitational forcing and internal ice deformation. Model results of surface velocity were compared to stake-derived surface velocities to analyze model accuracy and robustness; we found the model to be comparable within ±0.1 m a^{-1}. The model was then used to estimate ice volume flux across the TZ Hillside along the proposed new road location.

2.4. Results

2.4.1. Spatial variability of HPP region

After correcting and differencing the 6 February 2011 and 25 November 2015 DEMs, we found general thinning along the ice shelf terminus, retreat of the ice shelf terminus, and variable elevation change across the MIS-HPP region. The elevation loss at MIS terminus ranges from ~0–4 m, and the region of thinning aligns with the area of ice shelf retreat (Fig. 2.4). The region of compression folds shows both increasing and decreasing elevation change, highlighting the troughs and peaks of the surface topography and suggesting a migration of the folds. The ice shelf region neighboring the TZ shows elevation increase (0–3 m), with the exception of Pegasus Ice Road, where we observe thinning reaching 5 m a^{-1}. In the northern-central region of HPP, the elevation increased slightly (~0–1.5 m), while the northwest side experienced

greater elevation increase, surpassing 5 m in places. The southern portion of HPP displays the greatest range of values > ±5 m found in adjacent locations. This overall assessment across HPP and MIS aligns with previous findings using different methods (Campbell et al., 2018) suggesting that our study robustly captures surface elevation changes.

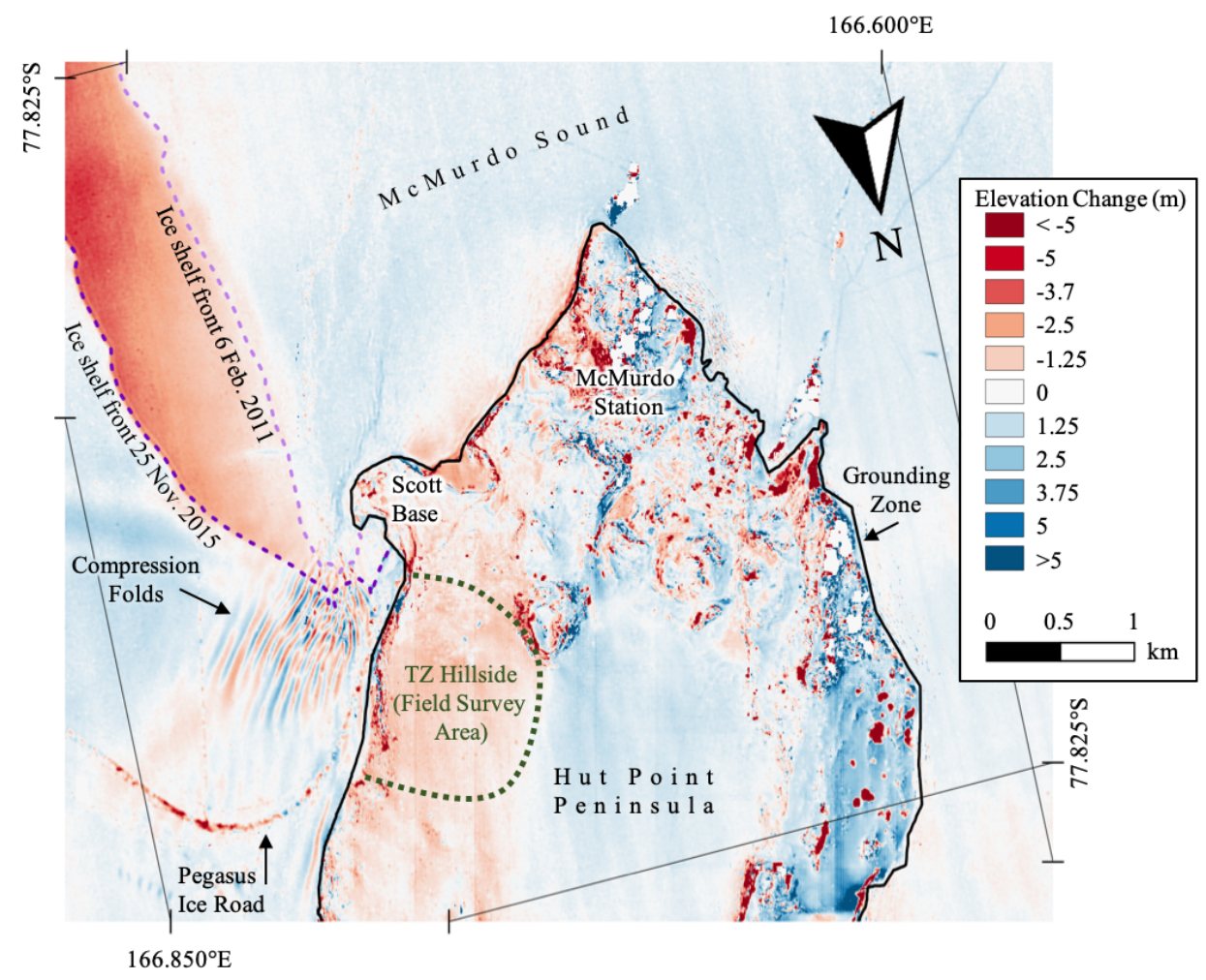

Figure 2.4. Surface elevation change on McMurdo Ice Shelf (MIS) and Hut Point Peninsula (HPP) between 6 February 2011 and 25 November 2015. This corrected DEM differencing shows thinning and retreat (light and dark purple dashed lines) along the ice shelf terminus, and variable elevation change across HPP.

2.4.2. Ice structure

2.4.2.1. Pegasus Ice Road structure

The GPR profiles collected on the Pegasus Ice Road (Fig. 2.5) reveal structure to ~20 m depth and surface conformable stratigraphy in the top 3–5 m. Thicker conformable stratigraphy is visible within syncline folds crossing the road. Below the surface conformable stratigraphy, heavily deformed, discontinuous, and dipping horizons are present. At 12–15 m depth, a series of stratified and discontinuous layers are prevalent. The near-surface stratigraphy is likely recent accumulation and firn reworked during yearly road construction over heavily deformed and fractured ice. The strong GPR horizons at 12–15 m depth likely represents discontinuous marine ice frozen onto the bottom of meteoric ice (e.g. Campbell et al., 2017). Vertical noise bands originate from specific horizons near 5 m depth. We interpret this noise to be caused by laterally continuous water tables within the firn. These horizons occur near the base of the surface-conformable stratigraphy, which supports our interpretation that the conformable stratigraphy is composed of permeable firn and the discontinuous layers below are likely impermeable meteoric glacier ice. This geophysical response to water in glacier snow or firn is a well-documented phenomenon (e.g., Campbell et al., 2012; Forster et al., 2014).

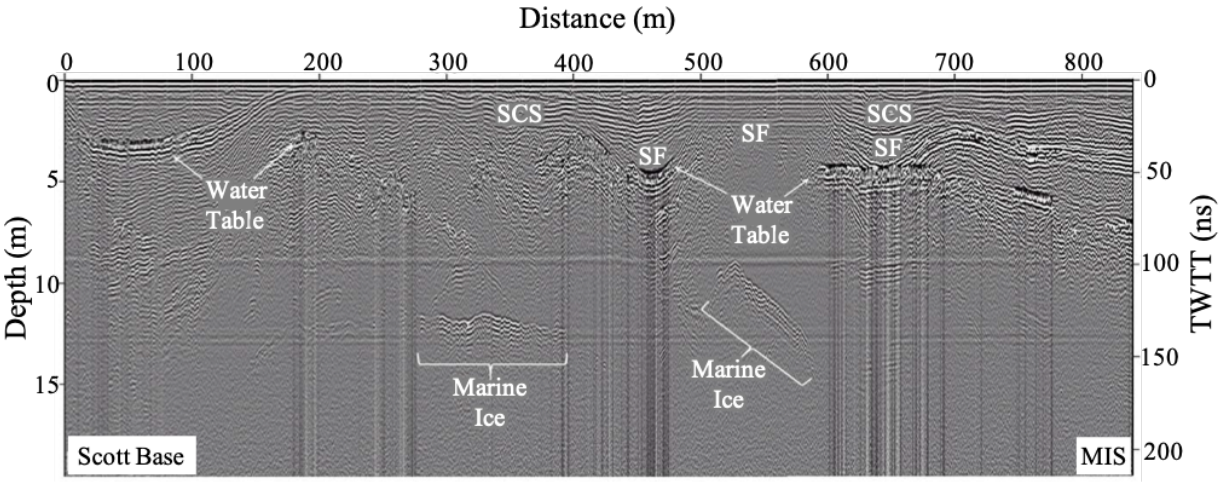

Figure 2.5. A 400 MHz GPR profile collected along the Pegasus Ice Road in January 2015. Profile shows near-surface conformable stratigraphy (SCS), complex syncline folds (SF), discontinuous stratified marine ice below, and vertical noise bands, which we interpret to be caused by water resting on the firn–ice transition. This GPR transect is displayed from Scott Base (SB) on left to MIS on right (location is shown in Fig. 2.7).

2.4.2.2. TZ Hillside ice structure

The 400 MHz and 100MHz antennas were both used to survey the TZ Hillside and quantify subsurface stratigraphy. Both antennas successfully imaged bedrock to ~65 m depth on the TZ Hillside, with greater thicknesses near the top of the hill and shallower depths located near the bottom, just above Pegasus Ice Road (~40-50 m thick). Profiles collected along the proposed new road on the TZ Hillside show relatively flat subglacial topography and ice thicknesses reaching 40 m depth. At the top of the hill, a buried symmetrical bedrock feature rises to within 25 m of the surface (Fig. 2.6). Substantial noise, high attenuation rates, and limited or no stratigraphy occurs within the radar data above the bedrock rise. Similar complex stratigraphy and noise has been observed in GPR profiles from temperate glaciers where snow, firn, or ice has been thermally altered thereby destroying stratigraphic horizons via chemical diffusion (Campbell et al., 2012). Elsewhere across the TZ Hillside, conformable stratigraphy is visible to 20–25 m depth in both the 400 MHz (Fig. 2.6a) and 100 MHz (Fig. 2.6b) data.

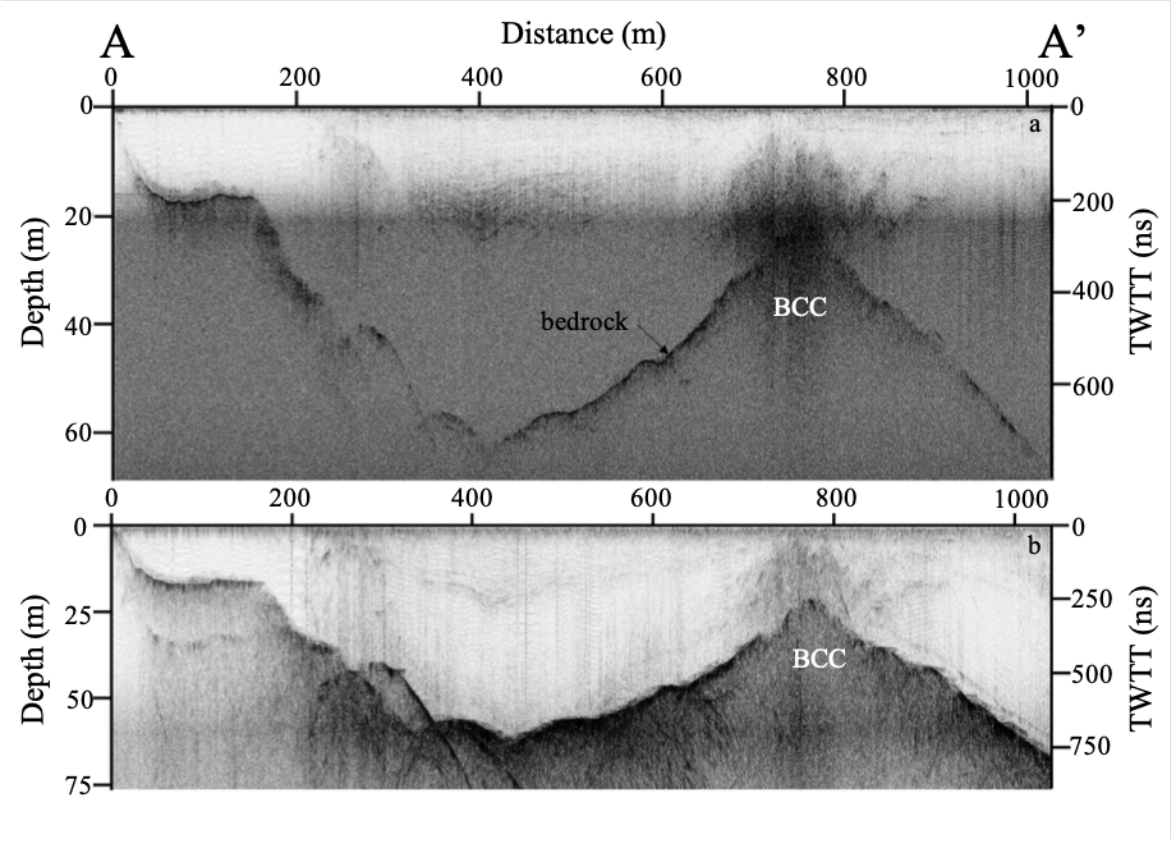

Figure 2.6. One of the parallel GPR transects on the TZ Hillside (location noted in Fig. 2.7). The 400 MHz profile (a) and the 100 MHz profile (b) with the bedrock topography and potentially buried cinder cone (BCC) noted. The complex stratigraphy above the cone is similar to noise imaged by GPR within temperate glaciers, suggesting that the ice has been thermally altered above the cone. Therefore, we suggest that ice has been situated overtop of the cone since its initial formation or at least, since recent thermal activity.

2.4.3. Ice velocity profiles

2.4.3.1. *In situ* surveys

Repeat kinematic GPS surveys of the 22 bamboo poles installed on the TZ Hillside revealed average ice-flow velocities from 0.1–1.1 ± 0.167 m a^{-1} with the highest velocities located in the eastern corner of the grid and near the bergschrund above the TZ (Fig. 2.7). While velocities were measured over austral summer, we assume these average velocities are maintained during the winter as the bed is likely frozen, due to the average annual temperature being near −20.7°C (Monaghan et al., 2005) and ice thicknesses being < 75 m. The velocity gradients result in tensile stresses towards the east and south, which match locations of

observed crevassing. The velocity profiles along the proposed road range from 0.29 m a^{-1} near exposed bedrock towards the west to 0.88 m a^{-1} closer to the eastern boundary of the grid (Fig. 2.7).

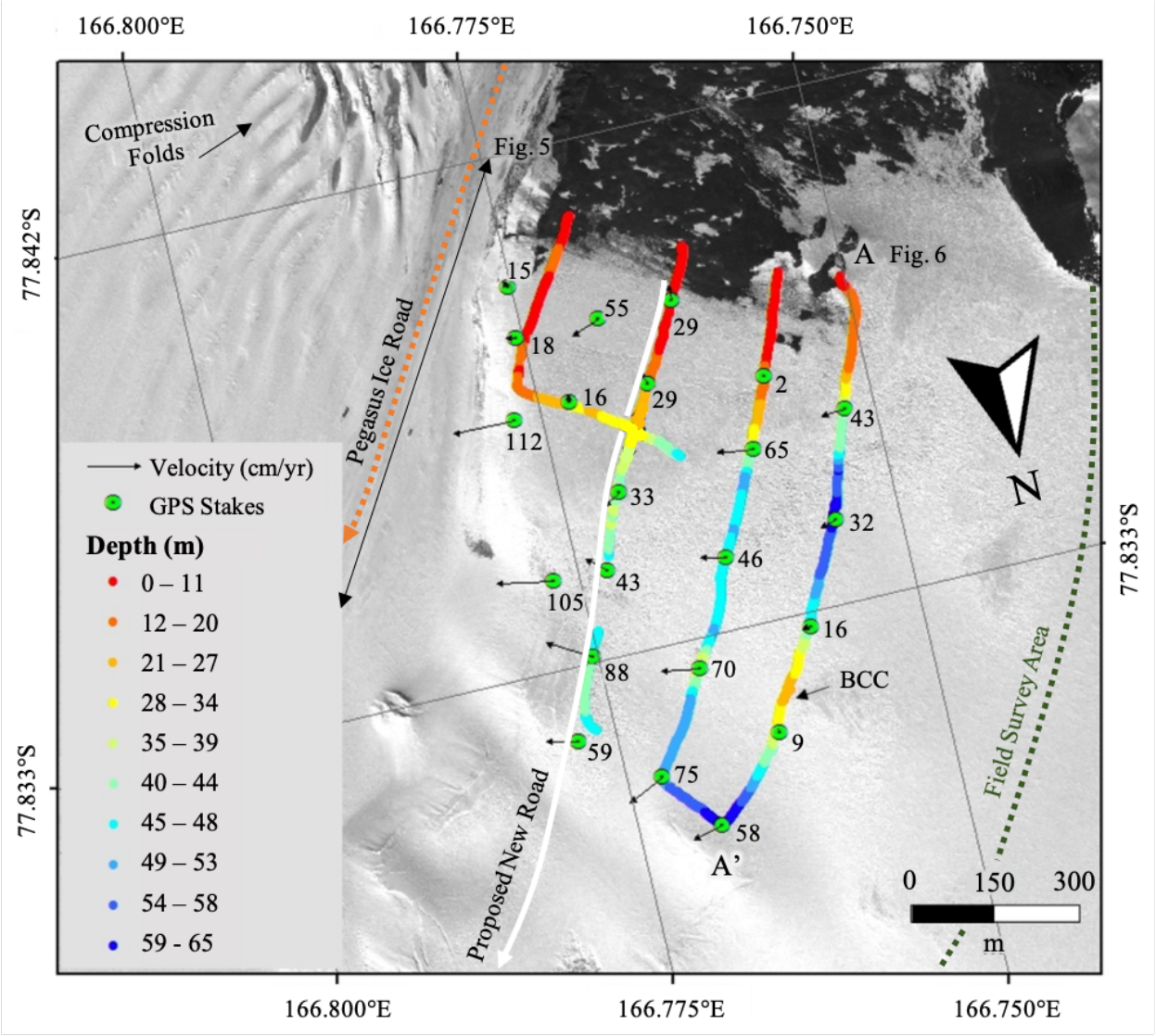

Figure 2.7. The field survey area (inside green dotted line) of the TZ Hillside. Noted are the locations of the January 2016 GPR transects and the 2015-2016 repeat GPS survey stake locations (green circles). Transect colors indicate measured ice thicknesses and arrows indicate ice-flow velocities (magnitude and direction) measured by kinematic GPS surveys in November 2015 and January 2016. Also notes are the buried cinder cone (BCC), Pegasus Ice Road (orange dotted line), the approximate proposed road location (white solid line), and specific GPR transects shown in Figs. 2.5 and 2.6.

2.4.3.2. Numerical modeling

Three-dimensional numerical modeling was performed across the TZ Hillside, specifically focusing on ice velocities around the proposed new road location. Modeling results show ice-flow velocities between 0.1 and 1.2 m a^{-1} across the hillside (Fig. 2.8). The average modeled ice velocity across the proposed road transect is 0.35 m a^{-1}. Velocities are slowest near the western glacier margin where ice thicknesses approach 0 m depth and over the buried cinder cone (BCC) near the top of the TZ Hillside where velocities are on the order of 0.1 m a^{-1}. Model velocity result patterns align well with GPS-measured velocities (±0.1 m a^{-1}), but are conservative in magnitude. We calculate the annual volume of ice crossing the road at the proposed road slice (Fig. 2.8) and find that over 204 ±24 m^3 (164,000–205,000 kg) of ice would need to be quarried annually from ice flowing downhill to maintain a bedrock road.

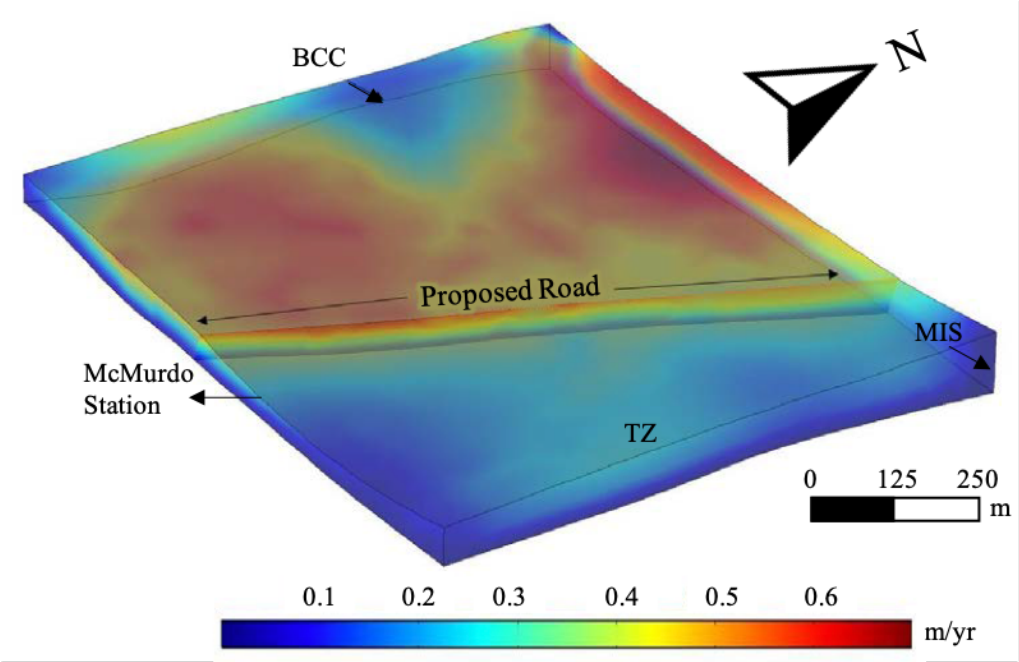

Figure 2.8. Temporal snapshot of the 3-D TZ Hillside finite element numerical model showing modeled ice flow velocities (m a^{-1}) and a slice across the proposed road. McMurdo Station is to the left/west and McMurdo Ice Shelf (MIS) and Grounding Line / Transition Zone (TZ) to the right/south of the model. Model dimensions are based on GPR measured ice thickness and GPS measured elevation. Model velocities closely match observed velocities (±0.1 m a^{-1}), including low velocities over the buried cinder cone (BCC). The proposed road slice was used to integrate annual ice volume crossing the proposed road region.

2.5. Discussion

The differencing of corrected DEMs highlights elevation change in the region, however, some variables could not be accounted for before differencing. The DEMs in 2011 and 2015 were constructed from imagery acquired during different seasons, which would contribute to some of the calculated elevation differences. The 2011 DEM was collected in the summer (January) at least halfway through the melt season, when winter snow would have already begun melting, whereas the 2015 DEM was collected in the early spring (November), when snow cover would be at its maximum. Ideally, both DEMs would be collected at the same time of year (e.g. both DEM's acquired in late summer during maximum melt); however, the limited availability of high-resolution satellite imagery precluded this option. Due to this imagery limitation, elevation differences presented here represent a conservative measurement of elevation change between 2011 and 2015 and future investigations should include elevations captured at the end of multiple melt seasons, thereby reducing seasonal impacts. Below, we consider the stability of both MIS (i.e. floating ice) and HPP (i.e. grounded ice) over our study period.

2.5.1. McMurdo Ice Shelf stability

In comparing DEM differences in MIS elevation between 2011 and 2015, we find that MIS does not reveal any clear signal of consistent elevation decrease, but instead variable change across the study area. The MIS terminus retreat occurring between 2011 – 2015 was accompanied by a predominant surface elevation decrease. Upstream from the MIS terminus, surface elevation change is more variable with areas gaining and losing ±1 m. We attribute the pocket of elevation loss in the region near the 90° bend of Pegasus Ice Road to be from excavators quarrying snow in this area to maintain the road or shifting snow drifts. The remainder of the flat MIS region exhibits very minor elevation gain (0-1.25 m). The most dramatic change in ice elevation occurs in the compression folds, aligning perpendicular to ice flow velocities (Fig. 2.4), suggesting that the pattern of alternating elevation gain and loss stems from shifting positions of peaks and

troughs. As this is a highly dynamic region, influenced by controlling variables such as accumulation, ablation, and ice flow, movement of compression fold peaks over an ~4 year period is a likely conclusion.

While we were able to resolve overall ice shelf elevation (freeboard) decreases in MIS between 2011 and 2015, we were not able to resolve the nature of MIS thinning; specifically, if the freeboard change resulted in a change of the ice shelf composition (percent of marine ice, glacier ice, accumulation), which is critical to ice shelf stability. Previous MIS studies suggest that marine ice reaches up to a third of the total MIS thickness, but the distribution of marine ice under MIS (and most other ice shelves) is currently unknown. This is, in part, due to the difficulties of measuring ice shelf composition using GPR, as conductive attenuation prevents GPR from penetrating the full ice shelf thickness (e.g. Arcone et al., 2016). Other studies suggest significant annual thinning of MIS via basal melt, which would counter significant marine ice freeze-on (e.g., Rack et al., 2013; Stern et al., 2013; Tinto et al., 2019). This discrepancy between freeze-on/melt and a lack of marine ice thickness observations is perhaps one of the greatest unknowns to MIS stability. To better resolve ice shelf stability, future marine ice thickness measurements are critical in order to contextualize changes in ice shelf elevation and associated freeboard.

The distribution pattern of surface elevation change across MIS is predominantly positive, therefore MIS terminus retreat currently appears to be more of a threat than surface or basal melt. Previous GPR surveys across MIS revealed higher accumulation rates near HPP on MIS than towards Black and White Islands (Campbell et al., 2017). These high accumulation rates near HPP likely counter any summer surface or basal melting which suggests that the logistical use of MIS may continue safely as long as the MIS terminus does not retreat to the TZ. However, MIS-HPP logistical concerns still exist, as meltwater within the TZ is pooling at the firn-ice transition, which we expect to persist, and potentially increase, as melt on the TZ Hillside continues. Therefore, Pegasus Ice Road may eventually need to be moved depending on future meltwater flux, thinning, or retreat of the MIS terminus into the TZ.

2.5.2. Hut Point Peninsula stability

While HPP is itself bedrock, roads leading from MIS to both Scott Base (New Zealand) and McMurdo Station (United States) cross onto HPP by way of crossing the TZ, a region experiencing a change in stability. Therefore, establishing potential alternative routes, which remove the TZ crossing, is critical to uninterrupted Antarctic science logistics. Surface elevation decreases on the south facing slope of HPP near the TZ is prominent, with an average elevation loss between 1–3 m. We interpret this surface lowering to be largely due to surface melt, and propose that this surface lowering is the primary source of meltwater runoff pooling on the TZ, since the hillside is primarily composed of impermeable ice (e.g. Shoop et al., 2014). The south TZ Hillside also shows some regions of 5 m elevation decrease; we propose that this elevation change could result from a combination of either poor vertical datum alignment in this region of the DEM and/or collapsed cornices, which form annually on this steep hillside.

The GPR profiles and GPS surveys collected across the TZ Hillside evaluated a potential alternative new road location. To install a road across the TZ Hillside, either blasting of ice to place the road on solid ground, or grooming an ice road over the current surface, would need to occur. Both options have major construction challenges, and each would require sizeable annual maintenance. The hillside is predominantly ice, therefore minimal firn is readily available to quarry for ice road maintenance. This does not account for the far greater volume of ice that would need to be excavated to create an initial bedrock-based road. The model results suggest that a bedrock-based road would be more problematic to initially build and maintain, if not impossible, due to the sizeable volume of annual ice removal that would be required, due to the dynamic hillside. However, the steep slope of the TZ Hillside would also make for potentially treacherous ice road conditions. These scenarios would need to be considered in design, building, and maintenance strategies prior to moving the current Pegasus Ice Road to the TZ Hillside.

2.6. Conclusion

The MIS-HPP region serves as the primary logistics hub for both the United States and New Zealand Antarctic Programs. The MIS also buttresses several tributary glaciers and is critical to the stability of RIS. Problematically, MIS is disproportionately susceptible to potential disintegration, due to high surface and basal melt rates, meltwater pooling, and tidal flexure. If MIS were to weaken or collapse, the United States and New Zealand Antarctic science programs would also incur sizeable logistics challenges. Here we focused on measuring the changes in ice elevation across MIS and HPP, and assessing a potential new access road between MIS and HPP. Through differencing DEMs collected in February 2011 and November 2015, we identified regions of large elevation change (± 5 m), as well as variability in the compression folds region, and MIS terminus retreat. The GPR surveys along Pegasus Ice Road found that the TZ crossing maintains pooled meltwater at the firn-ice transition, which can weaken the ice in this triaxial confluence of the HPP, MIS, and McMurdo sea ice. Additionally, GPR and GPS surveys on the TZ Hillside, as well as a resulting numerical model, explored the possibility of relocating the Pegasus Ice Road to bypass the TZ crossing. Results from the GPR, GPS, and numerical model showed that installation of a bedrock road or ice road would require either sizeable glacier ice excavation or complex engineering on steep glacier terrain, respectively, to bypass the current TZ crossing. Both scenarios would also require sizeable annual maintenance due to glacier ice creep and melt. While changes in ice elevation across the MIS-HPP region indicate no immediate need for rerouting Pegasus Ice Road to avoid the TZ crossing, GPS, GPR and modeling results also did not suggest a straightforward immediate road rerouting solution. However, due to increasing ocean and atmospheric temperatures, combined with the vulnerability and importance of MIS to Antarctic logistics, continued remote sensing and *in situ* monitoring of this region is essential in order to continue searching for alternative MIS-HPP access points. More broadly, MIS has important teleconnections across both East and West Antarctica and these results suggest that elevation, velocity, and ice thickness (including basal marine ice thickness) should be quantified and monitored more extensively across this region to capture potential dynamical changes which could have far-reaching consequences.

2.7. Acknowledgements

Financial support for fieldwork was provided by NSF to EPOLAR (at CRREL) award number EP-ANT-16-32. We thank the Polar Geospatial Center for providing GIS mapping support and the DEMs included in this work; UNAVCO for providing GPS support; those that assisted with fieldwork data collection and processing, including Nate Lamie, John Fegyveresi, Chris Simmons, Jim Mediatore, Evan Miller, John Stone, Perry Spector, and Trevor Hillebrand.

CHAPTER THREE

QUANTIFYING TEMPORAL AND SPATIAL SURFACE VELOCITY CHANGES ACROSS THE ICE SHELF-GLACIER INTERFACE

3.1. Abstract

The stability of McMurdo Ice Shelf (MIS) is especially important as it acts as a buttress to the much larger Ross Ice Shelf, into which mass from both East and West Antarctica flows. If MIS were to thin or collapse, its tributary glaciers and the abutting Ross Ice Shelf could also accelerate, thin, and potentially collapse, however this relationship between ice shelves and glaciers is not well quantified. Here I use surface velocity to quantify the interplay between the ice shelf and its tributary glaciers focusing on Terror, Aurora, and Koettlitz Glaciers, and the adjacent ice shelf areas from 2013 – 2020. With the exception of one date, the greatest surface speeds occur on the glaciers instead of the ice shelf (Terror Glacier: 201 m a^{-1}; Aurora Glacier: 142 m a^{-1}; Koettlitz Glacier: 94 m a^{-1}). Analyzing the speed across these focus sites using three methods revealed two different relationships between the ice shelf and its tributary glaciers: one in which both the ice shelf and tributary glacier both speed up during the summertime, and the other where the ice shelf fluctuates with the seasons and the tributary glacier remains consistent, suggesting spatial variability of driving forces. These results support the importance of including the glacier-ice shelf relationship to accurately represent the contribution of Antarctica to future sea level rise.

3.2. Introduction

The mass balance of the Antarctic Ice Sheet is a dynamic interplay between the addition of mass through annual snow accumulation and mass loss through acceleration and calving (e.g. Rignot et al., 2008), surface melt, and basal melt. While the East Antarctic Ice Sheet (EAIS) remained in steady state, the West Antarctic Ice Sheet (WAIS) averaged a mass loss of 789±42 Gt a^{-1} from 2009-2017 (Rignot et al., 2019), primarily through tributary glacier acceleration. Ice shelves play an essential role in reducing

discharge from tributary glaciers by slowing glacier velocities through both their mass and resistance to flow at lateral margins. In the absence of ice shelves, glaciers can rapidly accelerate and retreat. For example, following the collapse of the Larson A Ice Shelf, its tributary glaciers underwent a 450% velocity increase over the following 8 months (Royston & Gudmundsson, 2016). Therefore, in order to accurately predict the future contribution of Antarctica to global sea level rise, I first must quantify and constrain the glacier-ice shelf relationship.

Several glacier-ice shelf systems have the potential to greatly contribute to sea level rise, however, Ross Ice Shelf (RIS) is the largest ice shelf in the world (500,800 km^2; Rignot et al., 2013), and lies between WAIS and EAIS, consequently draining portions of both ice sheets (e.g., Tinto et al., 2019). On the northwest lateral margin of RIS sits McMurdo Ice Shelf (MIS) (~1,500 km^2; Banwell et al., 2017) with several tributary glaciers including Skelton Glacier flowing north around Minna Bluff, Koettlitz Glacier flowing north from the Dry Valleys, and Terror and Aurora Glaciers flowing south off of Ross Island (Fig. 3.1). In comparison to other ice shelves in Antarctica, MIS is relatively thin (~6 – 200 m; Arcone et al., 2016; Campbell et al., 2017; Glasser et al., 2006b), allowing warm surface water to flow directly underneath (MacGregor et al., 2013; Rack et al., 2013; Tinto et al., 2019). Recent studies found MIS exhibits extensive teleconnections, whereby its thinning could induce immediate acceleration of MacAyeal and Bindschadler Ice Streams over 900 km away (Reese et al., 2018), and acceleration could continue up to 80 km above the grounding line (Anandakrishnan et al., 2003). However, specific features in the physical environment of ice shelf-glacier systems can provide stabilization and slow the contribution to sea level rise.

One of the dominant controls working to stabilize MSI and combat melt and thinning are topographic controls like pinning points, places where the ice shelf becomes grounded on bedrock, decreasing the velocity due to shearing of the ice against the bedrock. Pinning points on MIS include Ross Island, Minna Bluff, White Island, and Black Island, which impede the flow of ice, reducing its velocity and providing stabilization. On the contrary, RIS has few pinning points and ultimately a faster velocity, creating a

velocity gradient across the boundary between RIS and MIS, and producing a shear zone of extensively crevassed ice (Kaluzienski et al., 2019). This marginal friction provides internal resistance to flow, helping stabilize MIS (Kaluzienski et al., 2019; Khazendar et al., 2015; MacGregor et al., 2013).

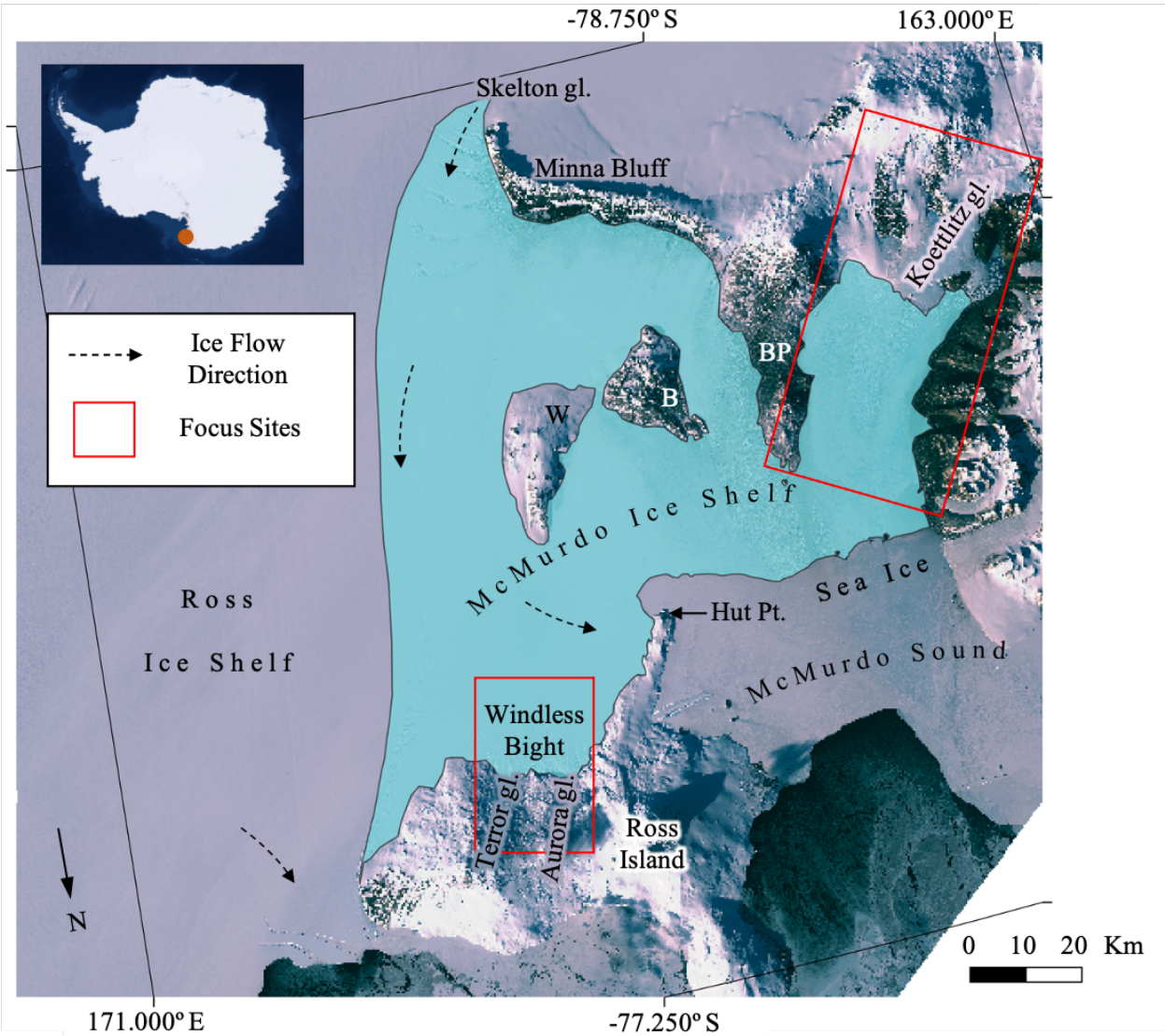

Figure 3.1. Map showing study region and focus study sites with major geographic points noted. McMurdo Ice Shelf (inset, orange circle; turquoise shading) is bound by RIS and McMurdo Sound. Noted are the locations of White Island (W), Black Island (B) and Brown Peninsula (BP). The red boxes define the focus study sites of Terror and Aurora Glaciers flowing into Windless Bight, and Koettlitz Glacier and its adjacent ice shelf area. Ice flow directions are denoted by dashed arrows (Campbell et al., 2017) with tributary glaciers (gl.) labeled. Background image collected from Sentinel-2 on 11 October 2019.

Surface velocity provides insight into the rate of mass transfer across the region, the system's sensitivity to changes in external forcings, and changes in stability. Therefore, this is an ideal metric for evaluating the relationship between glaciers and ice shelves. Velocity is controlled by the proportion and magnitude of different driving forces, including the degree of ice grounding and associated basal friction (Mayer & Siegert, 2000; Tikku et al., 2005), ice size and mass, ice composition (meteoric and marine ice), ice thickness (MacGregor et al., 2012; Rignot et al., 2013), pinning points and geologic restrictions (Berger et al., 2016), surface melt and pooling (Glasser et al., 2006), atmospheric temperatures (Bartholomew et al., 2010), and ocean temperatures and currents (Tinto et al., 2019). To evaluate the relationship between glaciers and ice shelves, I focus on MIS and its tributary glaciers, calculating velocity changes and deriving strain rates for both regions. I quantify glacier-ice shelf interactions on seasonal and annual time scales by analyzing the velocity results using three methods. While several current velocity products exist, not all are suitable for quantifying the seasonal and annual relationships between glaciers and ice shelves. MEaSUREs is a prominent velocity product comprised of multiple sources of remotely sensed imagery covering the polar regions. However, only one dataset is available covering MIS, and it presents 20-year average annual velocity from 1996 – 2016 (Fig. 3.2; Mouginot et al., 2012; Rignot et al., 2011). Thus, it is unable to resolve sub-annual changes. GoLIVE (Scambos et al., 2016) and ITS_LIVE (Gardner et al., 2019) velocity products have a higher temporal resolution, but struggle in the ice shelf region. Therefore, in this study, I use a combination of velocity products and newly derived velocities to address the science goal of quantifying the velocity across MIS and its tributary glaciers on seasonal and annual timescales.

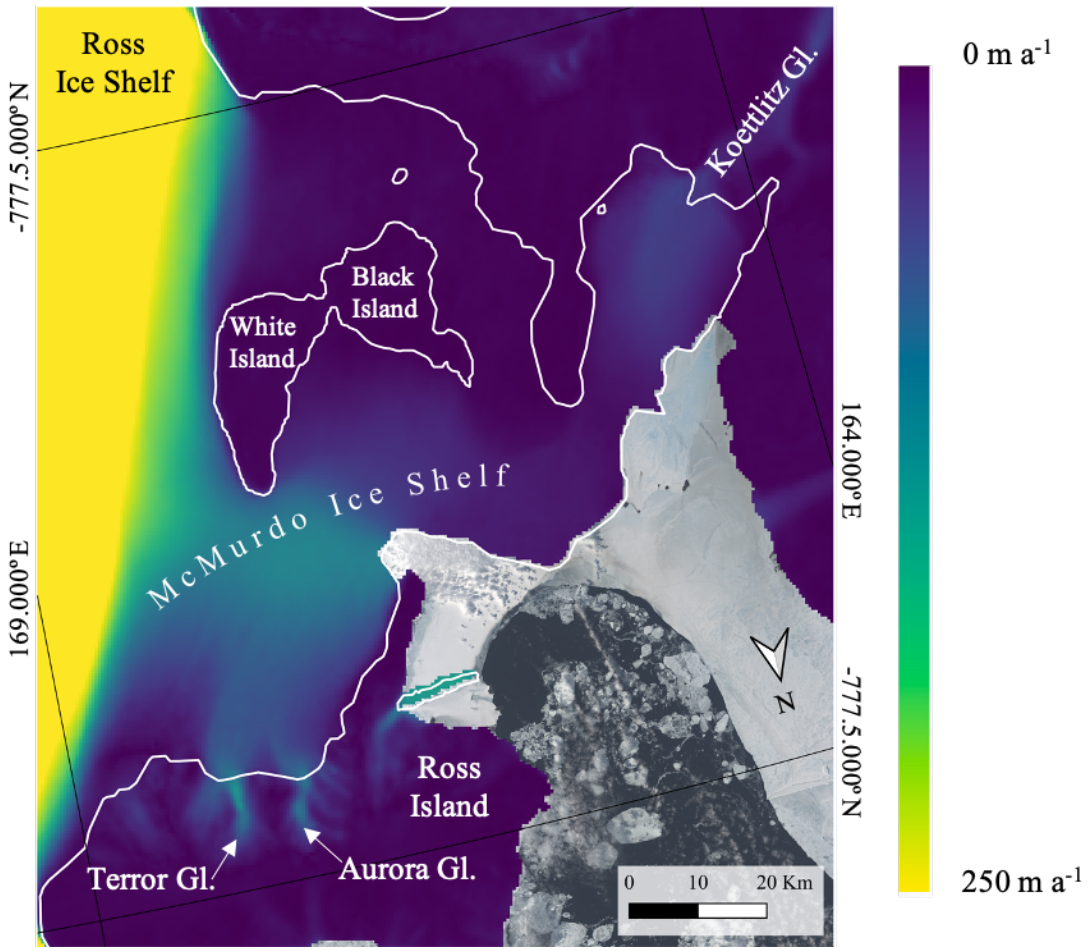

Figure 3.2. Map of annual average surface velocity in McMurdo Ice Shelf region from MEaSUREs. The white outline marks the boundary of Ross and McMurdo Ice Shelves. Values are very similar to those calculated using established methods and products detailed later in this thesis.

3.3. Methods

Glaciers and ice shelves often exhibit very different velocity regimes, making a single method of acquiring surface velocity values inadequate for glacier-ice shelf environments. To address this I separated glacier and ice shelf velocities (Fig. 3.3 A), calculated MIS surface velocities using COSI-Corr, a feature tracking extension used in ENVI, and used the Jet Propulsion Laboratory's ITS_LIVE (Gardner et al., 2019) and NASA's GoLIVE (Scambos et al., 2016) products for the velocity of the tributary glaciers. COSI-Corr successfully represents the velocity on the ice shelf (Fig. 3.3 B), but fails in regions of larger velocities (Fig. 3.3 B orange circles; Heid & Kääb, 2012). ITS_LIVE and GoLIVE can resolve these fast velocities, but

perform more poorly on the slower flowing ice shelf (Fig. 3.3 C). Consequently, I used both datasets to most accurately capture the surface velocity across the study area (Table 1; Heid & Kääb 2012).

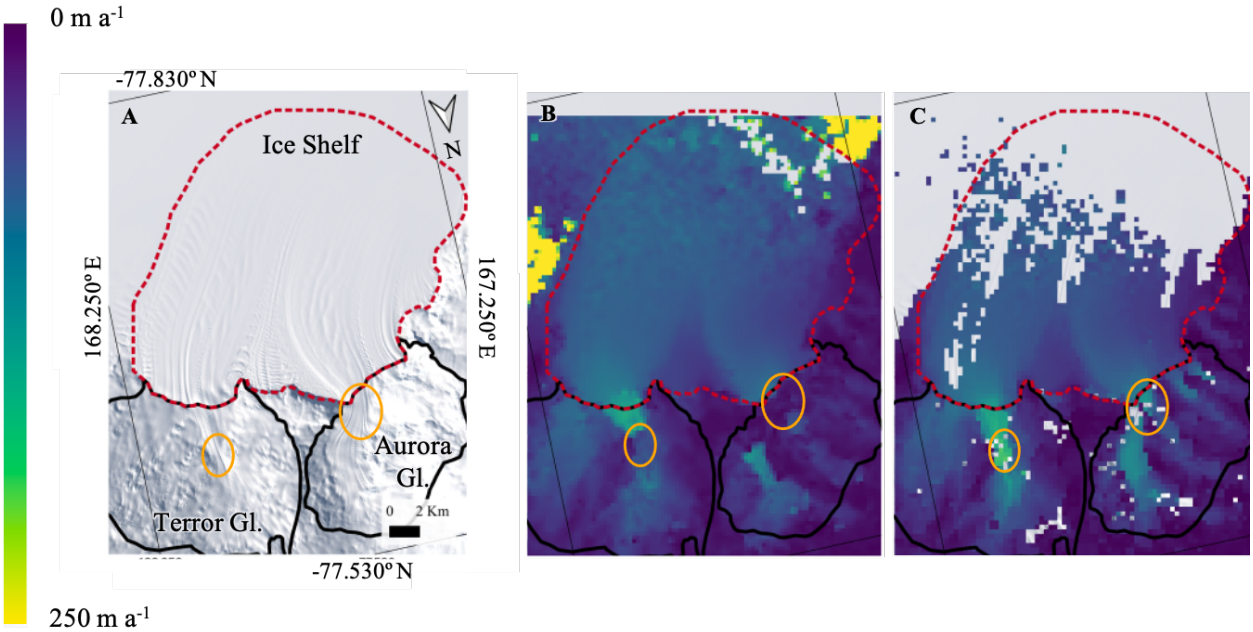

Figure 3.3. Comparison of COSI-Corr to ITS_LIVE and GoLIVE datasets in the Terror and Aurora Glacier and Windless Bight region. Panel A depicts the region in a true-color Landsat 8 image, while panel B shows the surface velocity (m a^{-1}) results from COSI-Corr, and panel C displays the GoLIVE velocity results (m a^{-1}). The orange circles indicate points of narrowing near the terminus of each glacier. The red dashed line indicates the boundary of the ice shelf area of interest, and the black lines indicate the area of interest for Terror and Aurora Glaciers.

3.3.1. Deriving velocities from feature tracking

On Terror, Aurora, and Koettlitz Glaciers I derived velocity values using COSI-Corr, where I applied a Fourier-based feature tracking algorithm to the panchromatic band of Landsat 8 imagery spanning 2013 – 2020. The feature tracking method relies on the identification of common surface features between the two images using a user-defined sliding window (generally twice the maximum expected surface velocity), providing spatial constraints when matching features between the two images. Consequently, this method will fail if too much movement places the features outside the bounds of the window, or if too little movement occurs and the displacement is within the uncertainty. I processed the COSI-Corr results using a combination of MATLAB and QGIS, removing values with a signal-to-noise ratio >0.9 (in both

directions; Ayoub et al., 2015), and outside two standard deviations of the mean. I calculated the error associated with the COSI-Corr method by looking at the velocity of a stationary region, the exposed bedrock adjacent to Koettlitz Glacier, and established an error range of 0.023 m a^{-1} – 11.25 m a^{-1}. For the velocity on the glaciers, I used ITS_LIVE (Gardner et al., 2019) and GoLIVE (Scambos et al., 2016) (Table 3.1), which have uncertainties of 1 m a^{-1} and 0.02 m d^{-1} – 1 m d^{-1} respectively.

Date Range	Koettlitz Ice Shelf Velocity and Strain Rate	Koettlitz Glacier Velocity	Windless Bight Velocity, Velocity Anomaly, and Strain Rate	Terror And Aurora Glaciers Velocity, and Velocity Anomaly
27 Dec. 2013 - 27 Oct. 2014	COSI-Corr	ITS_LIVE	COSI-Corr	ITS_LIVE
27 Oct. 2014 - 12 Nov. 2014	COSI-Corr	ITS_LIVE		
27 Oct. 2014 - 15 Oct. 2015	COSI-Corr	ITS_LIVE	COSI-Corr	ITS_LIVE
15 Oct. 2015 - 1 Dec. 2015			COSI-Corr	ITS_LIVE
1 Dec. 2015 - 3 Dec. 2016	COSI-Corr	ITS_LIVE	COSI-Corr	ITS_LIVE
3 Dec. 2016 - 5 Feb. 2017			COSI-Corr	ITS_LIVE
5 Feb. 2017 - 4 Nov. 2017			COSI-Corr	ITS_LIVE
4 Nov. 2017 - 7 Jan. 2018			COSI-Corr	ITS_LIVE
7 Jan. 2018 - 25 Oct. 2019	COSI-Corr		COSI-Corr	
25 Oct. 2019 - 27 Oct. 2020	COSI-Corr	GoLIVE	COSI-Corr	GoLIVE

Table 3.1. Data source used for each date, region, and calculation.

3.3.2. Quantifying glacier-ice shelf velocity behavior

To analyze the glacier-ice shelf behavior, I first spliced together the COSI-Corr and ITS_LIVE/GoLIVE data at the grounding line to create a single dataset of ice shelf and glacier velocities. I did not include time periods of glacier and ice shelf velocities where the COSI-Corr and ITS_LIVE/GoLIVE data did not align, as it was unclear which velocity calculation of the two datasets was accurate (Table 3.1). To quantify velocity behavior, I used three methods, as there is no single metric to highlight the surface velocity across both the ice shelf and the tributary glaciers: (1) average velocities across the entire glacier-ice shelf system, (2) centerline transect velocity, and (3) velocity distribution curves. The average velocity calculation computes the average of all data points on each ice shelf area and each glacier. The centerline transects

extract the velocity along multiple parallel transects running down the general flowline of each glacier and onto the ice shelf. As the transects generally run longitudinally, I averaged by latitude to the central transect line, so as not to place too much value on a single pixel (Fig. 3.4), producing the average centerline velocity. In this calculation, the ice shelf and glacier velocity data were spliced together at the location along the transect where the datasets are equal. I calculated the distribution of the velocity values by binning velocity values of all glacier and ice shelf data points, and plotting the frequency of velocity values over time.

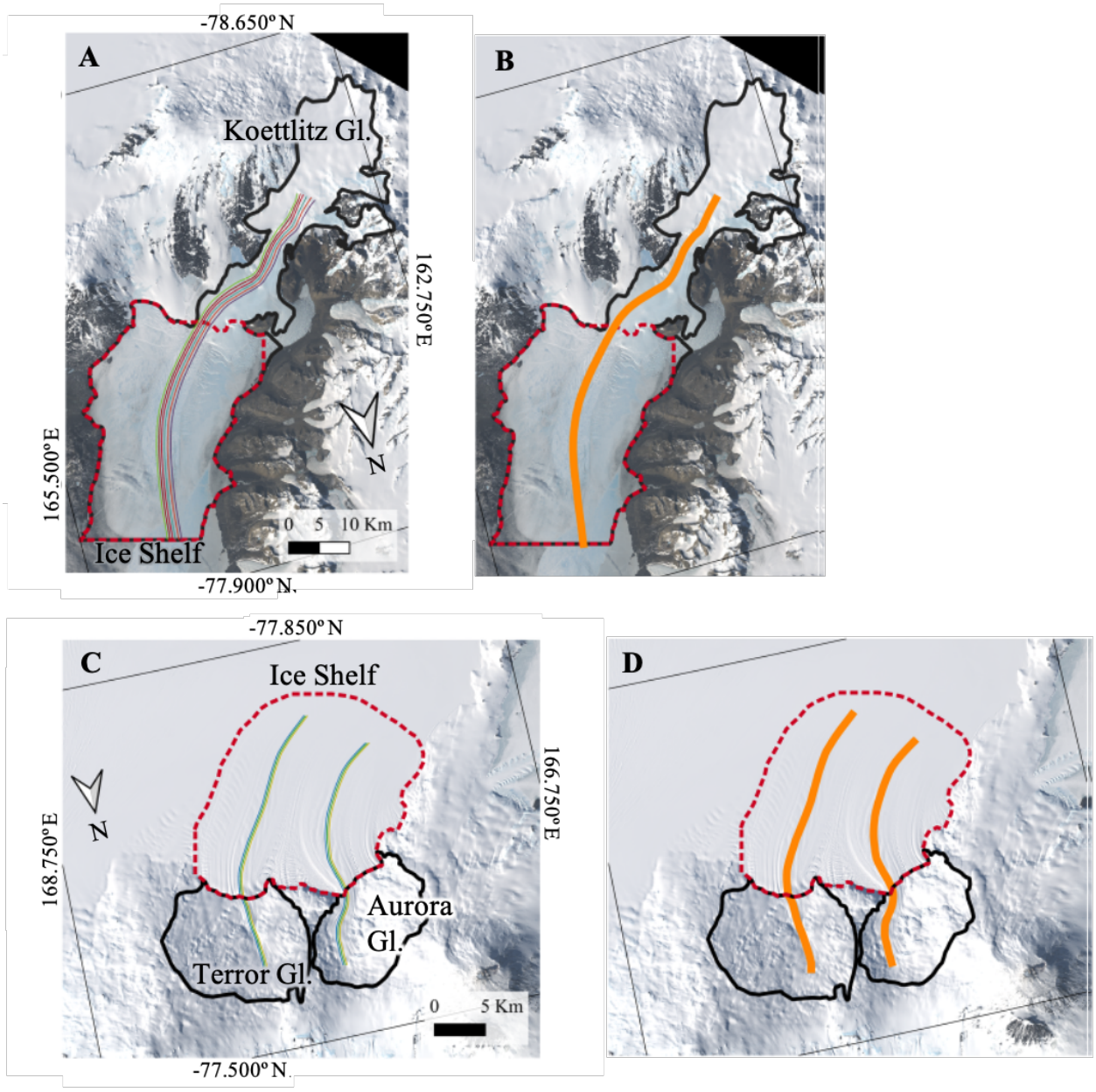

Figure 3.4. Location of transects over true-color image of focus regions, with ice shelf and glacier areas outlined discretely. Panels A and B show the Koettlitz Glacier focus site, with the black outline indicating the glacier extent and the red dashed line indicating the extent of the ice shelf area of interest. Panels C and D show the Terror and Aurora Glacier, and Windless Bight focus site. Panels A and C depict the transect lines along which the velocity data were extracted, and panels B and D depict the resulting area of the averaged transect lines for each focus site.

3.3.3. Anomalies

To analyze velocity changes between years, I calculated velocity anomalies by first establishing a baseline velocity raster. The baseline velocity was calculated using a time-weighted geospatial average of the surface velocity data. Due to limited image availability in the Koettlitz region (n=5), I focused on the Terror and Aurora systems, which have a continuous record (Table 3.1). I then calculated the velocity anomaly by subtracting the baseline velocity from each individual velocity time period.

3.3.4. Strain rates

To gain further insight into the dynamics of the glacier-ice shelf system, I calculated both the volumetric and shear strain rates on the ice shelf in both focus study sites using the derived velocity rasters in Golden Software Surfer. Before calculating the strain rates, I cropped the two ice shelf areas 2-3 pixels (480 m – 720 m) from the bedrock edge to eliminate translation at the ice-rock boundary. The volumetric strain rate describes the expansion and contraction of the ice due to normal strains, and is computed using the equation

$$Volumetric\ Strain\ Rate = 0.5\left(\frac{\partial Vx}{\partial x} - \frac{\partial Vy}{\partial y}\right), \qquad \text{Equation 1}$$

where Vx is the velocity in the x-direction and Vy is the velocity in the y-direction.

The shear strain rate describes the change in shape resulting from shear stress, or forces being applied to the ice in opposite directions, and is calculated using the equation

$$Shear\ Strain\ Rate = 0.5\left(\frac{\partial Vx}{\partial y} + \frac{\partial Vy}{\partial x}\right). \qquad \text{Equation 2}$$

In these calculations I set positive volumetric strain as expansion (when the y-component of the ice velocity increases in the positive y-direction) (Fig. 3.5 A), and negative volumetric strain as ice contraction (when the y-component of the ice velocity decreases in the positive y-direction) (Fig. 3.5 B). I set positive shear

strain as an increase in velocity when moving in the positive x-direction, and negative shear strain as a decrease in velocity when moving in the positive x-direction. Therefore, ice flowing through a confined channel creates positive shear strain along the left lateral margin, and negative shear strain along the right lateral margin, with the magnitude of shear strain decreasing towards the center (Fig. 3.5 C).

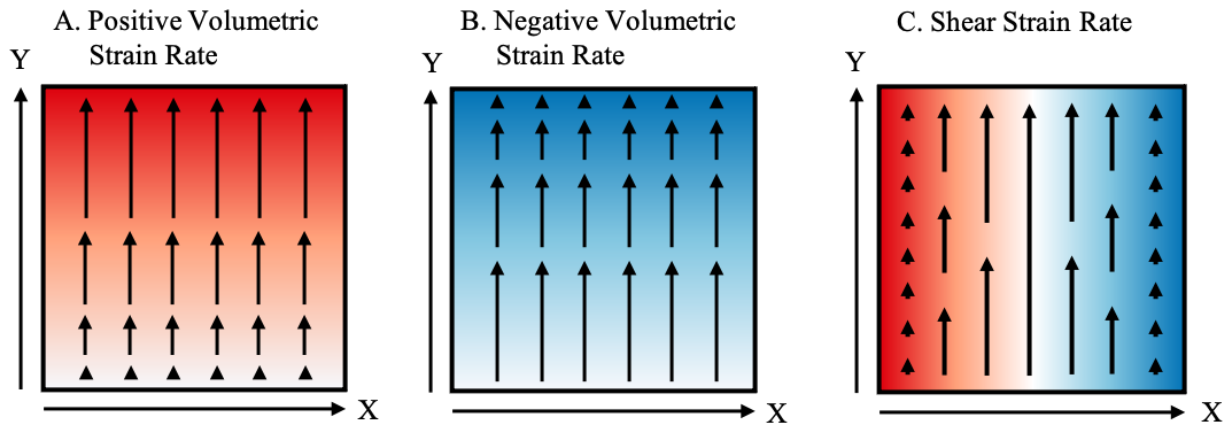

Figure 3.5. Idealized models of strain rate. The arrows within the x-y plain represent velocity vectors in an overhead view of ice flowing in the positive y-direction. The panels represent (A) positive volumetric strain rate with directional forces $\frac{\partial u}{\partial x} = 0; \frac{\partial v}{\partial x} = 0; \frac{\partial v}{\partial y} = +; \frac{\partial u}{\partial y} = 0$, (B) negative volumetric strain rate with directional forces $\frac{\partial u}{\partial x} = 0; \frac{\partial v}{\partial x} = 0; \frac{\partial v}{\partial y} = -; \frac{\partial u}{\partial y} = 0$, (C) shear strain rate with directional forces on the right half $\frac{\partial u}{\partial x} = 0; \frac{\partial v}{\partial x} = -; \frac{\partial v}{\partial y} = 0; \frac{\partial u}{\partial y} = 0$, and on the left half $\frac{\partial u}{\partial x} = 0; \frac{\partial v}{\partial x} = +; \frac{\partial v}{\partial y} = 0; \frac{\partial u}{\partial y} = 0$.

3.3.5. Identifying surface melt

To quantify changes in surface melt on MIS, I used Landsat 8 surface reflectance band ratios. Band ratios have been used successfully to track the drainage of supraglacial lakes >0.125 km^2 in Greenland with the Normalized Difference Lake Index (NDLI),

$$NDLI = \frac{R_r - R_{nir}}{R_{nir} + R_r} \qquad \text{Equation 3}$$

where R_r is the surface reflectance in the red band, and R_{nir} is the surface reflectance in the near-infrared band (Morriss et al., 2013; Schild et al., 2016). This ratio is used to identify the timing of melt onset, the length of the melt season, and the spatial extent of surface melt across MIS.

3.4. Results

3.4.1. Geospatial velocity patterns

All three study locations, Koettlitz, Terror, and Aurora, followed similar geospatial velocity patterns. The highest velocities were found along the centerline of the glaciers (Koettlitz: 100 m a^{-1}; Terror: 210 m a^{-1}; Aurora: 145 m a^{-1}), and approached 0 m a^{-1} along the glacier margins (Fig. 3.6; Fig. 3.7). The maximum velocities for each ice shelf occurred near the glacier termini, but were smaller in magnitude than their glacier counterparts (Koettlitz: 75 m a^{-1}; Windless Bight: 80 m a^{-1} – 120 m a^{-1}; Fig. 3.6; Fig. 3.7). Seasonally, glacier velocities were fairly consistent, while MIS displayed larger velocities in the summer than in the winter (Fig.3.6; Fig. 3.7). In addition to the velocity magnitude, the velocity direction also exhibits spatial and temporal variability. Koettlitz Glacier flows north onto the ice shelf where it curves slightly west (Fig. 3.6), and Terror and Aurora Glaciers flow south into Windless Bight before curving to the southwest, except during the summer when the flow is initially to the southeast across the grounding line before curving southeast (Fig. 3.7). Two scenes do not follow the behavior of the other time periods, 14 Oct. 2015 – 1 Dec. 2015 at Windless Bight (Fig. 3.7 C), and 27 Oct. 2014 – 12 Nov. 2014 at Koettlitz (Fig. 3.6 B). In these scenes, velocity vectors maintain unrealistic and conflicting directions of flow (to the southwest at Windless Bight, to the east at Koettlitz), and likely result from minimal displacement between Landsat images. This is a known limitation of the feature tracking method, and will produce false results with these characteristics. The 14 Oct. 2015 – 1 Dec. 2015 data at Windless Bight (Fig. 3.7 C) will not be considered during analysis, as other summer-only data exist in this location and show results that align with that which is expected.

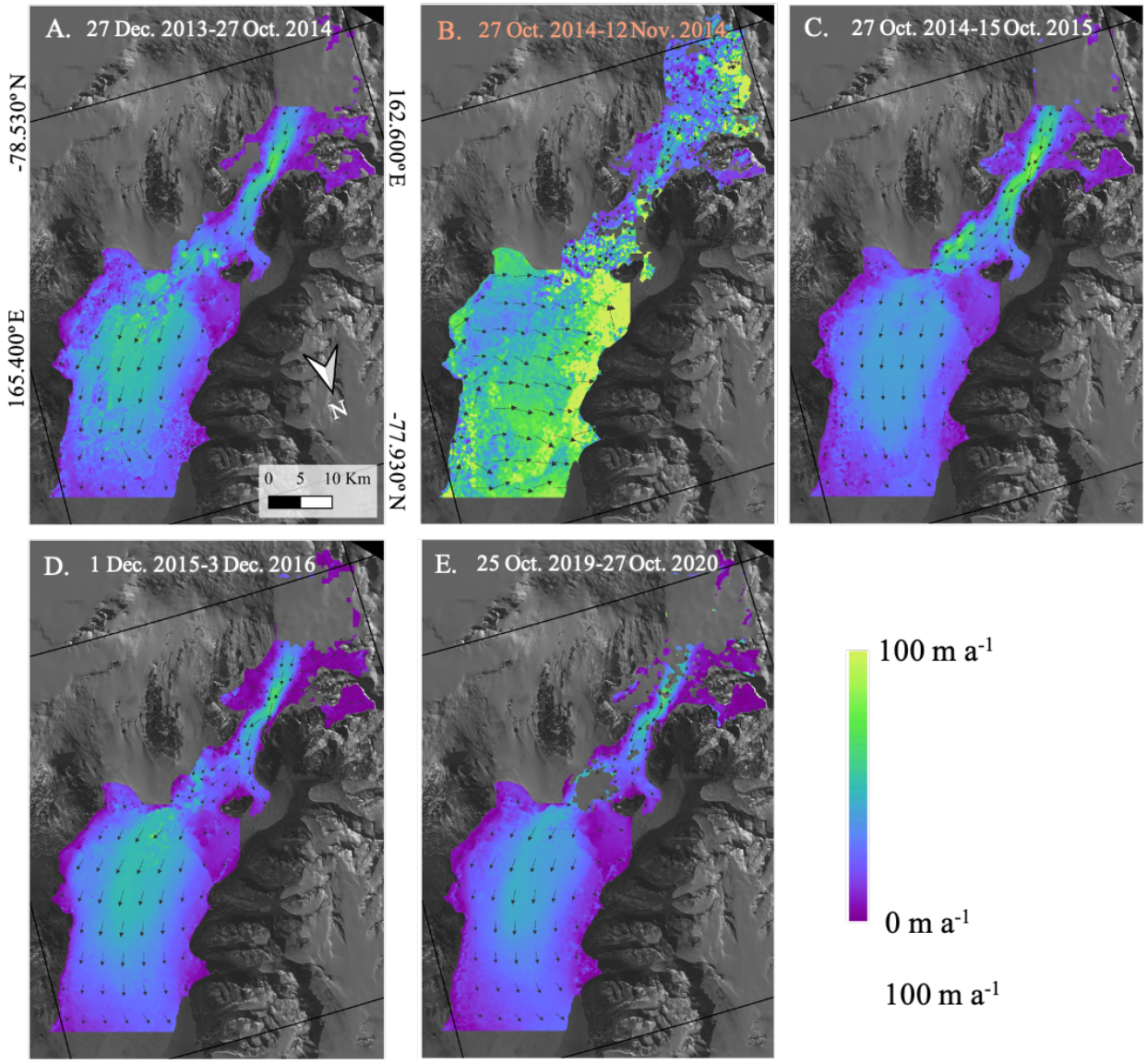

Figure 3.6. Surface velocity on Koettlitz Glacier and adjacent ice shelf. The surface velocity (m a^{-1}) from ITS_LIVE/GoLIVE covers the glacier and is spliced with the COSI-Corr surface velocity data (m a^{-1}) on the ice shelf. Black vector arrows overlay the velocity magnitude. Each panel (A-E) displays the surface velocity for the dates noted in each panel. The black box in panel A identifies the terminus region discussed in figure 3.20. The light red colored label identifies scenes that span only the summer months. Faster velocities occur towards the center of the ice shelf and glacier, while smaller velocities are found along the margins.

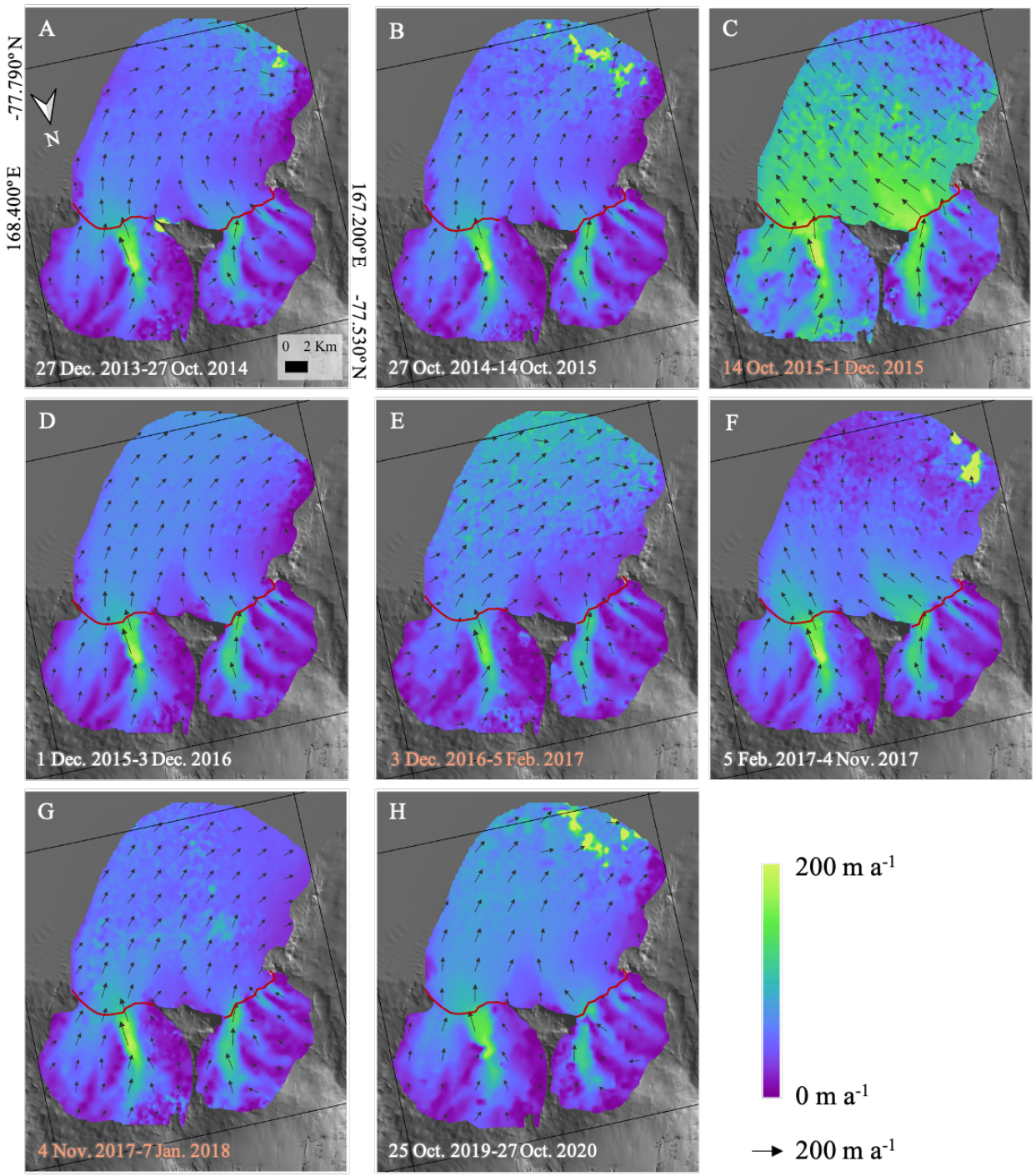

Figure 3.7. Surface velocity on Terror and Aurora Glaciers, and the ice shelf in the adjacent Windless Bight. The surface velocity (m a^{-1}) from ITS_LIVE/GoLIVE covers the glaciers and is spliced with the COSI-Corr surface velocity (m a^{-1}) data on the ice shelf. Black vector arrows overlay the velocity magnitude over the ice shelf. The dark red lines mark the approximate grounding line location. Each panel (A-E) displays the surface velocity for the dates noted in each panel. The black box in panel A identifies the terminus region discussed in figure 3.21. The light red colored label identifies scenes that span only the summer months. Larger velocities are found along the main glacier channels, and on the ice shelf near the glacier termini. The velocity decreases on the ice shelf with distance from the glaciers.

3.4.2. Average ice shelf and glacier surface speeds

When averaging all velocity measurements within each ice shelf region and tributary glacier, I found average ice shelf velocities between 10 m a^{-1} – 180 m a^{-1} (Koettlitz: 10 m a^{-1} – 70 m a^{-1}; Windless Bight: 55 m a^{-1} – 180 m a^{-1}; Fig. 3.8), and an average glacier speed between 16 m a^{-1} – 50 m a^{-1} (Koettlitz Glacier: 16 m a^{-1} – 50 m a^{-1}, Terror Glacier: 38 m a^{-1} – 48 m a^{-1}, Aurora Glacier: 38 m a^{-1} – 44 m a^{-1}; Fig. 3.8; Table 3.2). Ice shelf summer speeds are 2-3 times greater than winter speeds in Windless Bight, and 3-5 times greater near Koettlitz Glacier. The smaller speeds in the Koettlitz region also span a smaller range of values, only 55 m a^{-1}, in comparison to the speed values in Windless Bight, which have a range of 125 m a^{-1}. When directly comparing the spatially-averaged speed on the tributary glaciers and the ice shelf, the ice shelf speed is 2% - 43% greater than Koettlitz Glacier, with the greatest differences measured in the summer season (Fig. 3.9), 16% - 70% greater than on Terror Glacier, and 23% - 73% greater than on Aurora Glacier (Fig. 3.10). With the exception of Dec. 3, 2016 – Feb. 5, 2017, where the values are almost equal, the speed on Terror Glacier is greater than on Aurora Glacier (Fig. 3.10).

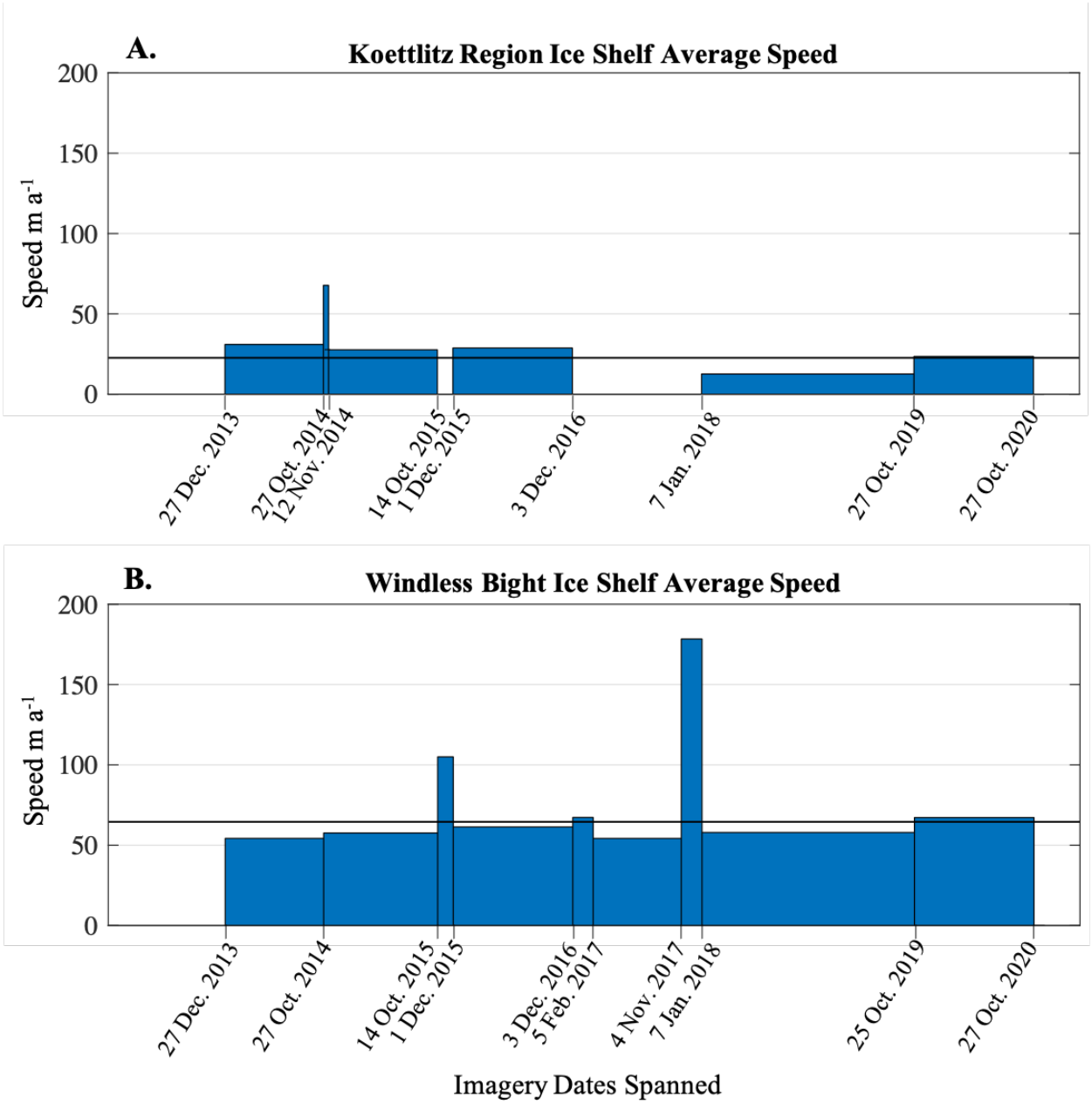

Figure 3.8. Comparison of the average surface speed on ice shelf in two study regions through time. Panel A shows the average speed (m a^{-1}) results from the ice shelf in front of Koettlitz Glacier. This is the area outlined by the red dashed line in Fig. 3.4 (A, B). Panel B shows the average speed (m a^{-1}) results from the ice shelf in front of Terror and Aurora Glaciers, also noted by the red dashed line in Fig. 3.4 (C, D). The horizontal black line cutting across both panels indicates the time-weighted velocity average of the. The speed in the Koettlitz region is less than the velocity in the Terror and Aurora region, and the summer speed is greater than the winter.

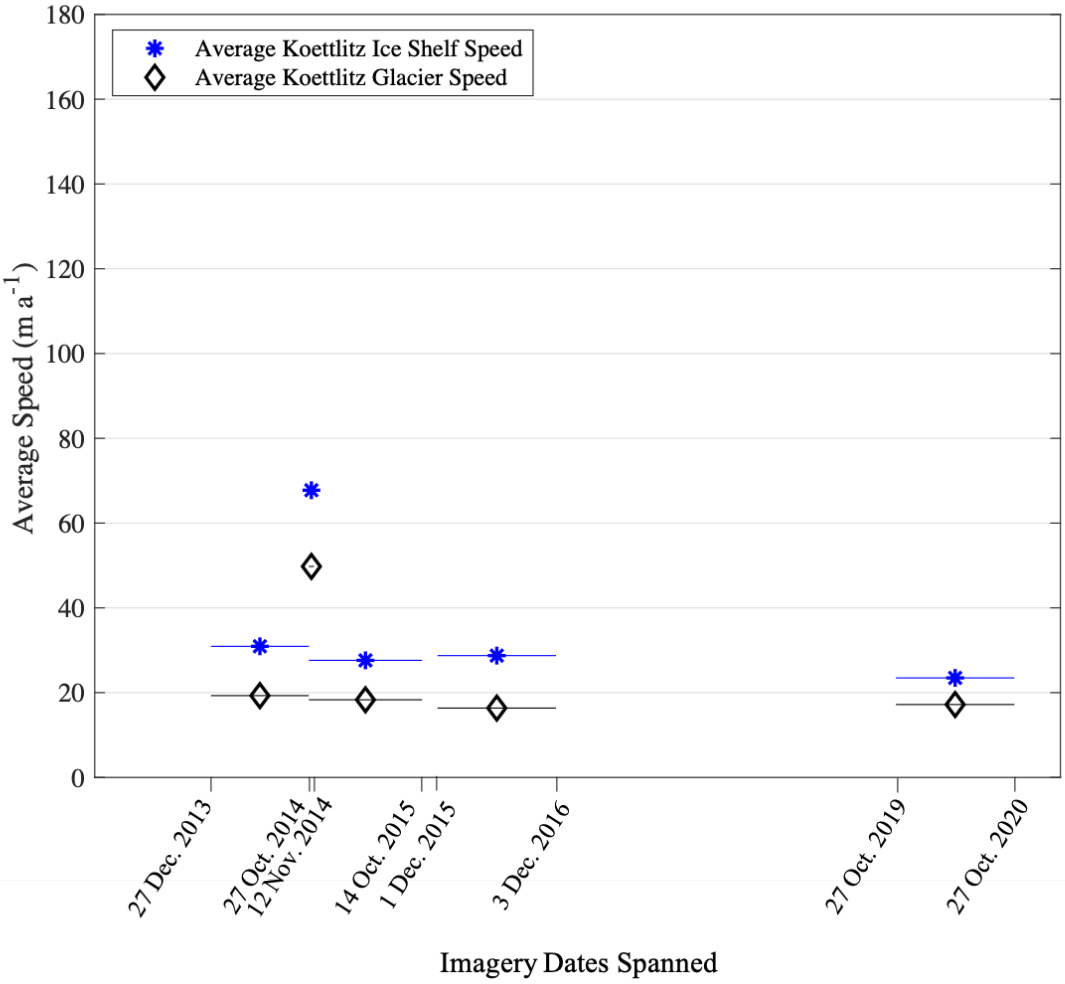

Figure 3.9. Comparison of average speed on Koettlitz Glacier, and the adjacent ice shelf area. The horizontal axis shows the dates of each image between which the speed was calculated. Over short, seasonal timescales, these lines are not noticeable as they are no wider than the points themselves.

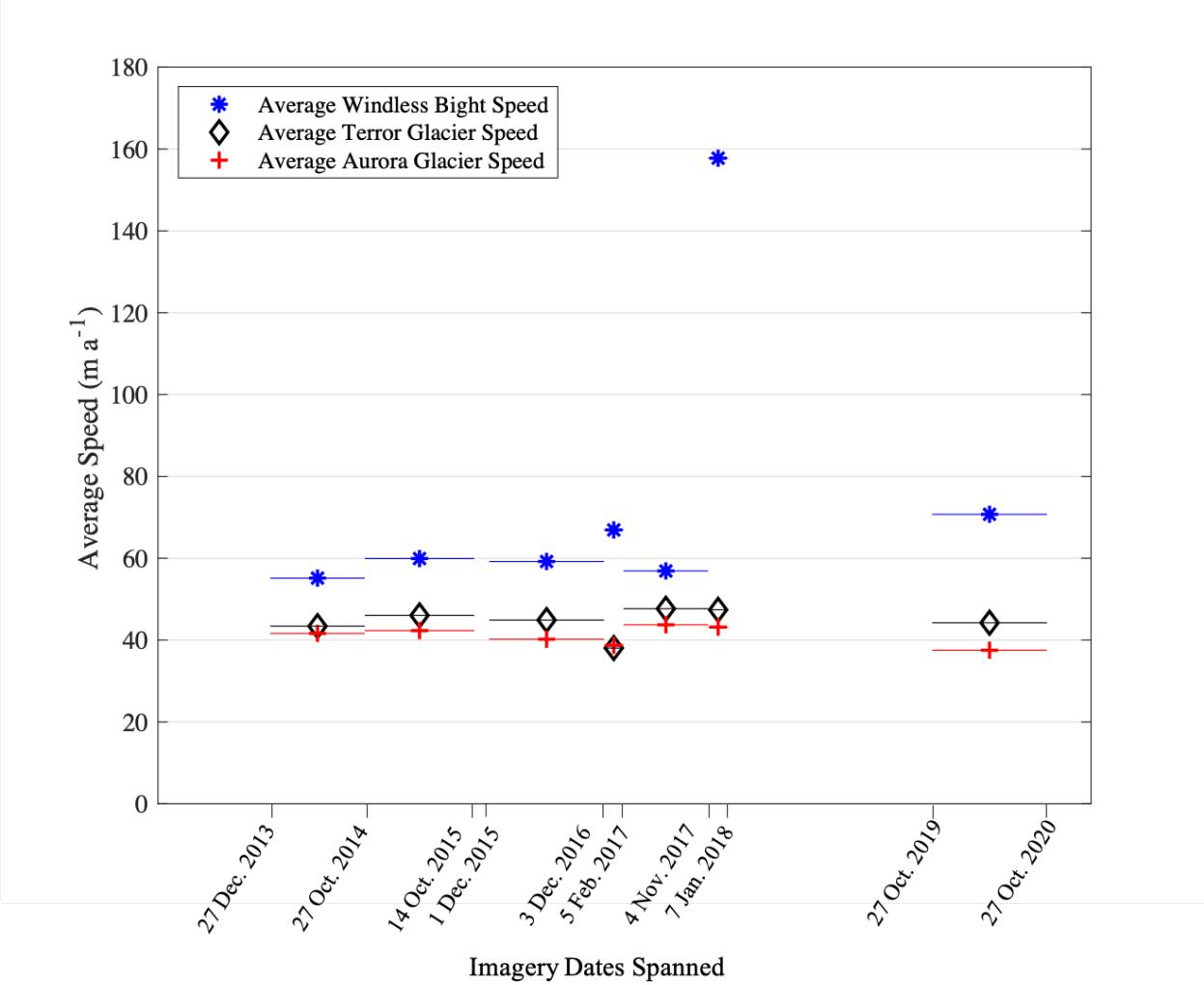

Figure 3.10. Comparison of average speed on Terror Glacier, Aurora Glacier, and the adjacent ice shelf area. The horizontal axis shows the dates of each image between which the speed was calculated. Over short, seasonal timescales, these lines are not noticeable as they are no wider than the points themselves.

3.4.3. Surface speed along central transects

The average centerline transects for Terror, Aurora, and Koettlitz all showed glacier velocities reaching their maximum speeds near their approximate grounding line. Those maximum average speeds ranged from 43 m a^{-1} – 225 m a^{-1} (Terror: 160 m a^{-1} – 225 m a^{-1}; Aurora: 105 – 200 m a^{-1}; Koettlitz: 43 m a^{-1} – 94 m a^{-1}; Fig. 3.11). The only deviation from this trend was during some of the summer-only averages, where speed continued to increase along the length of the transect.

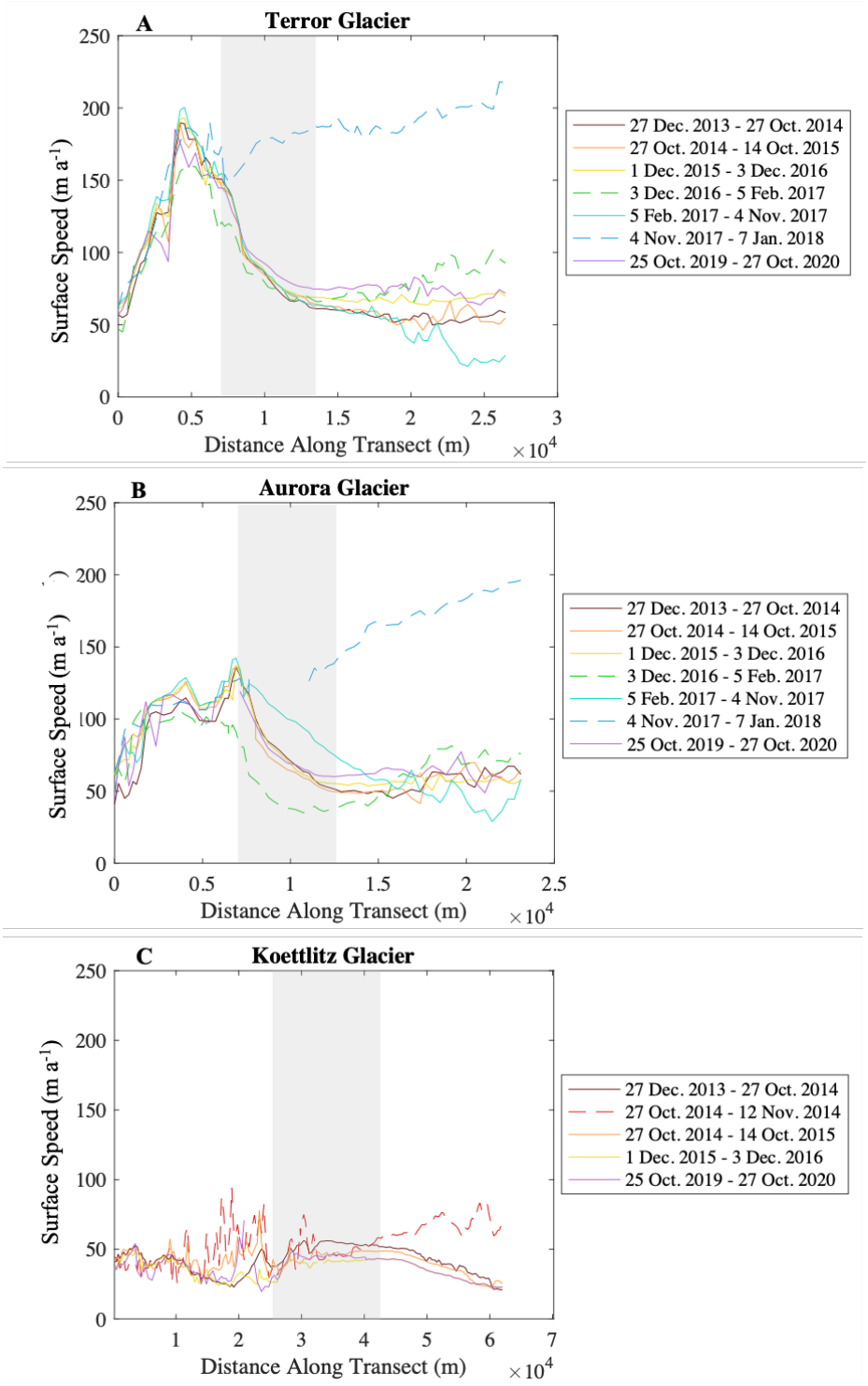

Figure 3.11. Surface speed along transects on each of the three glacier sites and their adjacent ice shelf areas. Panel A shows the speed (m a^{-1}) along the averaged transects on Terror Glacier and the ice shelf. Panels B and C displays data following the same methodology as that in A except on Aurora Glacier (B) and Koettlitz Glacier (C). The dashed lines indicate time periods that do not include winter months. The grey shaded regions denote the range of locations along the transects, which crosses from glacier to ice shelf, where and the COSI-Corr and ITS_LIVE/GoLIVE data were spliced together.

3.4.4. Surface speed frequency distribution

To establish if variability exists in geospatial velocity distribution, I compiled pixel speeds across each glacier and ice shelf region. I found that all ice shelf regions have greater mode surface speed than their tributary glaciers, and the mode speeds on Windless Bight and its tributary glaciers are greater than those in the Koettlitz region (Fig. 3.12), with ice shelf mode values ranging from <5 m a^{-1} – 95 m a^{-1} (Koettlitz: <5 m a^{-1}; Windless Bight: 55 m a^{-1} – 95 m a^{-1}), and glacier mode values ranging from <5 m a^{-1} – 25 m a^{-1} (Koettlitz: <5 m a^{-1}; Terror: 10 m a^{-1} – 30 m a^{-1}, Aurora: 15 m a^{-1} – 25 m a^{-1}). Additionally, maximum speeds occur during the summer, as the summer-only surface speeds are more evenly distributed across the range of values than those that span an entire year.

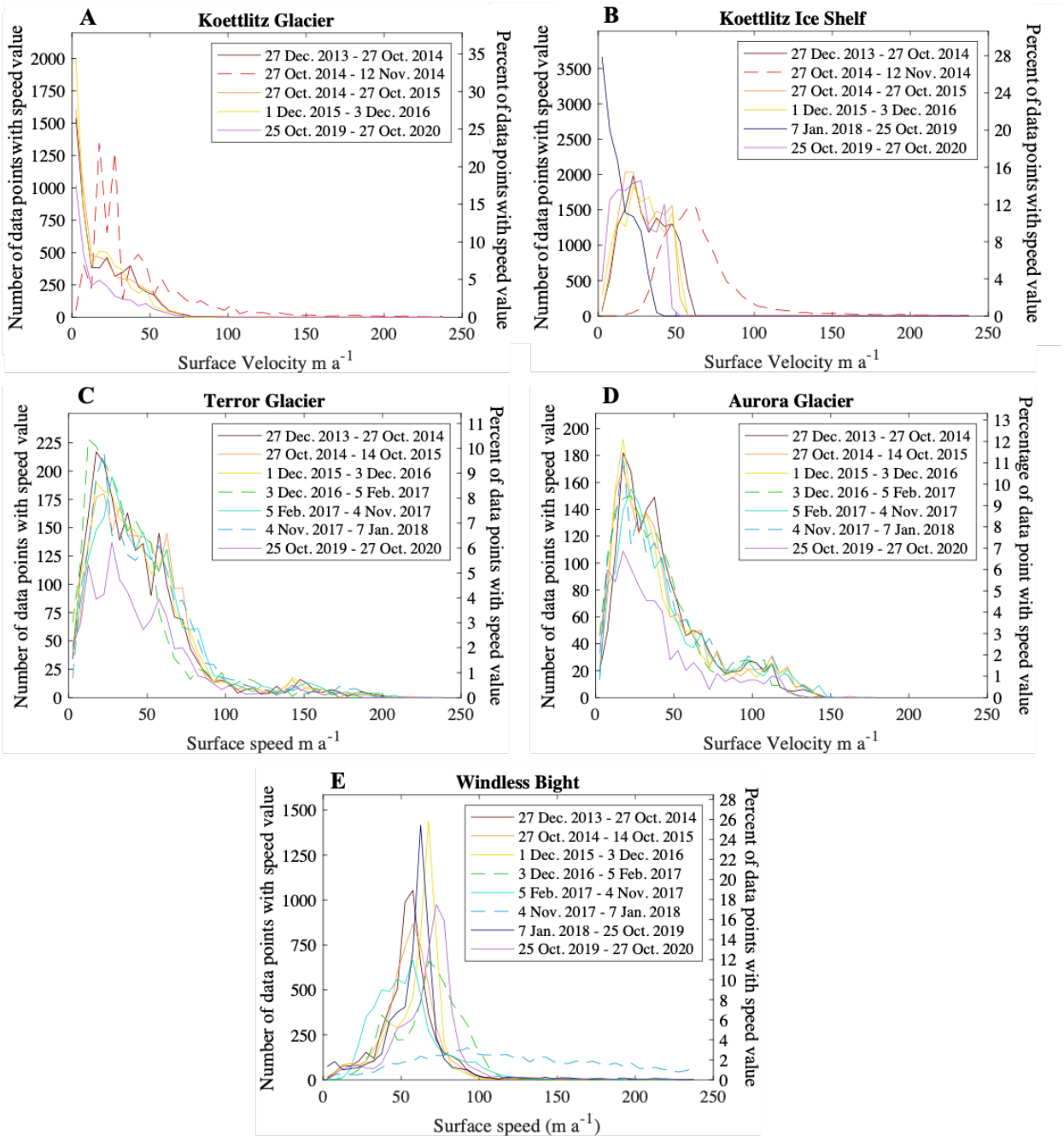

Figure 3.12. Surface speed distribution across Terror, Aurora, and Koettlitz Glaciers, and their adjacent ice shelf areas. Each line represents the number of data points with a surface speed value between a predefined range of values (left vertical axis) and the probability of a surface speed data point being within a predefined range of values. The dashed lines indicate time periods that do not include winter months. The surface speed distribution (m a^{-1}) is represented on Koettlitz Glacier (A), the ice shelf adjacent to Koettlitz Glacier (B), Terror Glacier (C), Aurora Glacier (D), and the in shelf in Windless Bight (E).

3.4.5. Surface speed anomalies

To isolate changes in speed on seasonal and annual time scales, I calculated anomalies using the geospatial velocity data. The weighted average velocity of all geospatial velocity data, hereafter referred to as the base, ranges from 11 m a^{-1} – 206 m a^{-1} at Windless Bight (Fig. 3.13), and 3 m a^{-1} – 196 m a^{-1} at Terror and Aurora Glaciers (Fig. 3.14). At Windless Bight, time periods that span close to a year have smaller anomalies (-20 m a^{-1} – 20 m a^{-1}) (Fig. 3.13 B, C, E, I, J), while those that represent seasonal velocities span a much larger range (-50 m a^{-1} – 250 m a^{-1}) (Fig. 3.13 F, G, H). Little spatial variability exists in the annual time periods, but the seasonal data display two spatial patterns. The summer data show a general trend of below average to above average anomaly when moving south from the grounding line (Fig. 3.13 F), while the time period that spans only the winter shows the opposite trend (Fig. 3.13 G). The values in the southwest corner of each scene show anomaly values up to 2.5x the magnitude of the values displayed in the rest of the scene, and have values far above and below the base that lie adjacent to each other, indicating the limits of the feature tracking method. The difference from the mean does not follow a distinguishable flow regime across the glacier, and there is little seasonal variability (±15 m a^{-1}), with the exception of one summertime period (Dec. 3, 2016 – Feb. 5, 2017) exhibiting velocity much below average (-41 m a^{-1}) (Fig. 3.14 F).

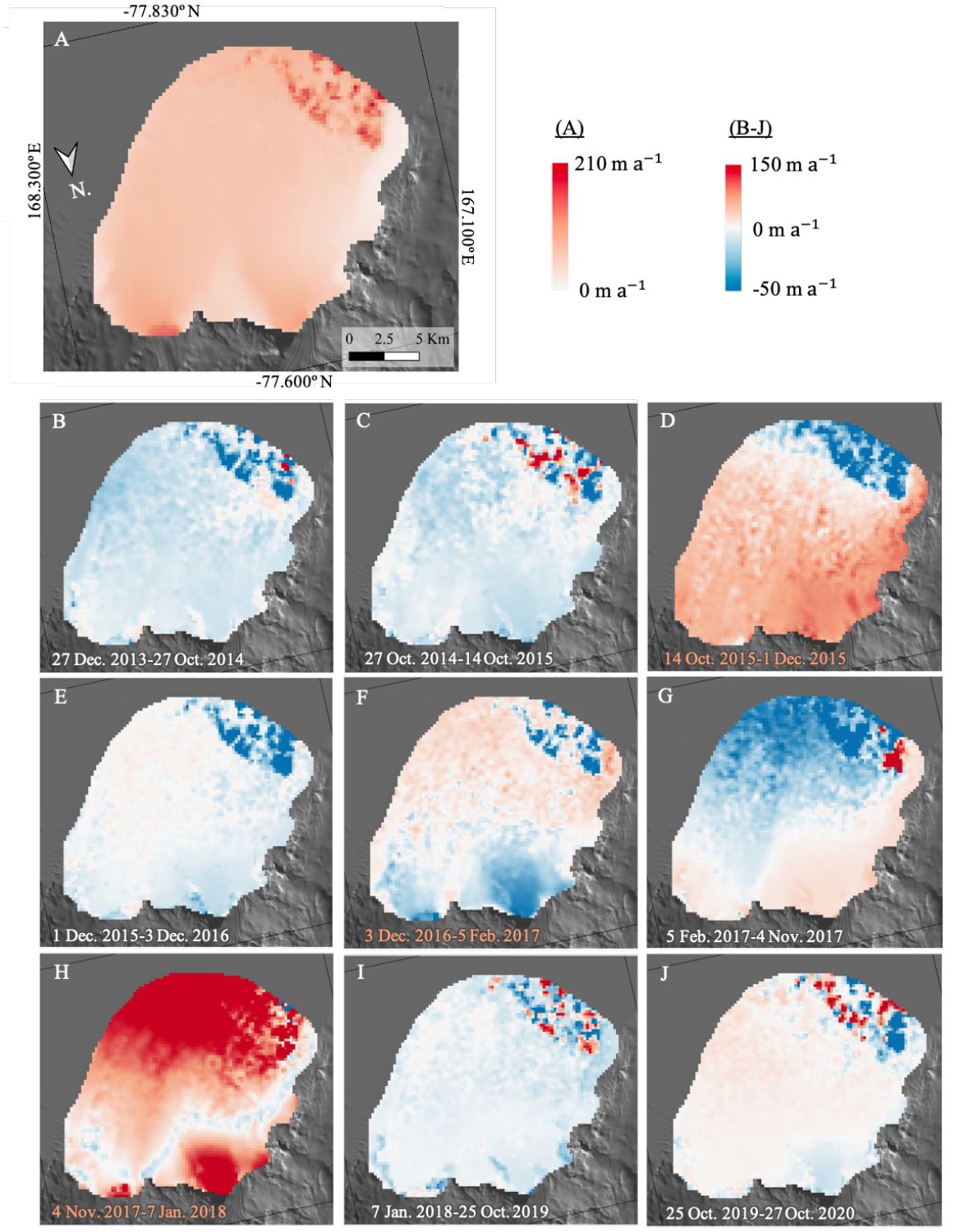

Figure 3.13. Ice shelf surface speed anomaly for region adjacent to Terror and Aurora Glaciers. The base image (A) shows the time-weighted average speed (m a^{-1}) for the ice shelf area from 2013 – 2020. Panels B – J show the surface speed anomaly (m a^{-1}) for the dates noted in each panel. The speed anomaly is consistent moving east-west, and forms a gradient moving north-south across the ice shelf.

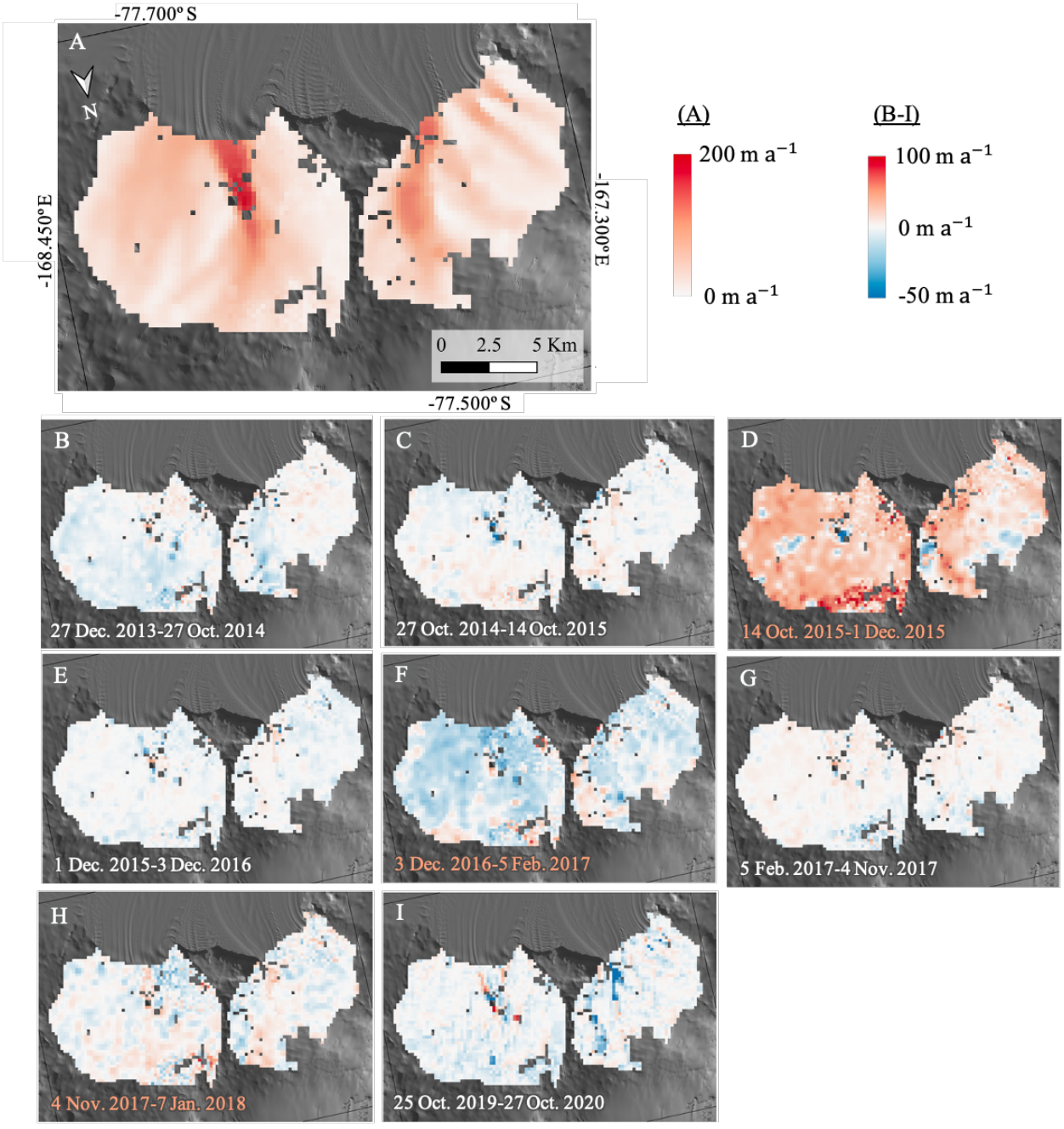

Figure 3.14. Surface speed anomaly for Terror and Aurora Glaciers. The base image (A) shows the time-weighted average speed (m a^{-1}) for the glaciers from 2013 – 2020. Panels B – I show the surface speed anomaly (m a^{-1}) for the dates noted in each panel. Most of the surface speed anomalies fall close to the base average with only one time period showing widely positive anomalies and only one time period showing widely negative anomalies.

3.4.6. Volumetric and shear strain rates

I found minimal areas of expansion and contraction on the ice shelf in front of Koettlitz Glacier (-0.001 a^{-1} – 0.001 a^{-1}; Fig. 3.15); however, northeast-southwest contraction occurs in the southern corner, and north-south expansion occurs in the western corner and along the northern edge (Fig. 3.15). The shear strain rate (Fig. 3.16) follows a similar distribution of equal magnitude values. Right-lateral shearing occurs in the southern corner and along the northern boundary of the study area, and left-lateral shearing occurs in the western corner (Fig. 3.16). Both volumetric and shear strain rate data show more pervasive higher magnitude values (10-100x above average), and higher signal to noise ratios in the earliest two time periods (Figs. 3.15 A, 3.16 A; Figs. 3.15 B, 3.16 B), than the four more recent time periods. These volumetric strain rate patterns suggest that the glacier accelerates across the grounding line, then decreases in speed when moving towards the front of the ice shelf, the direction of flow is dictated by the geometry of the sidewalls, and the speed is fastest towards the center and slowest along the margins.

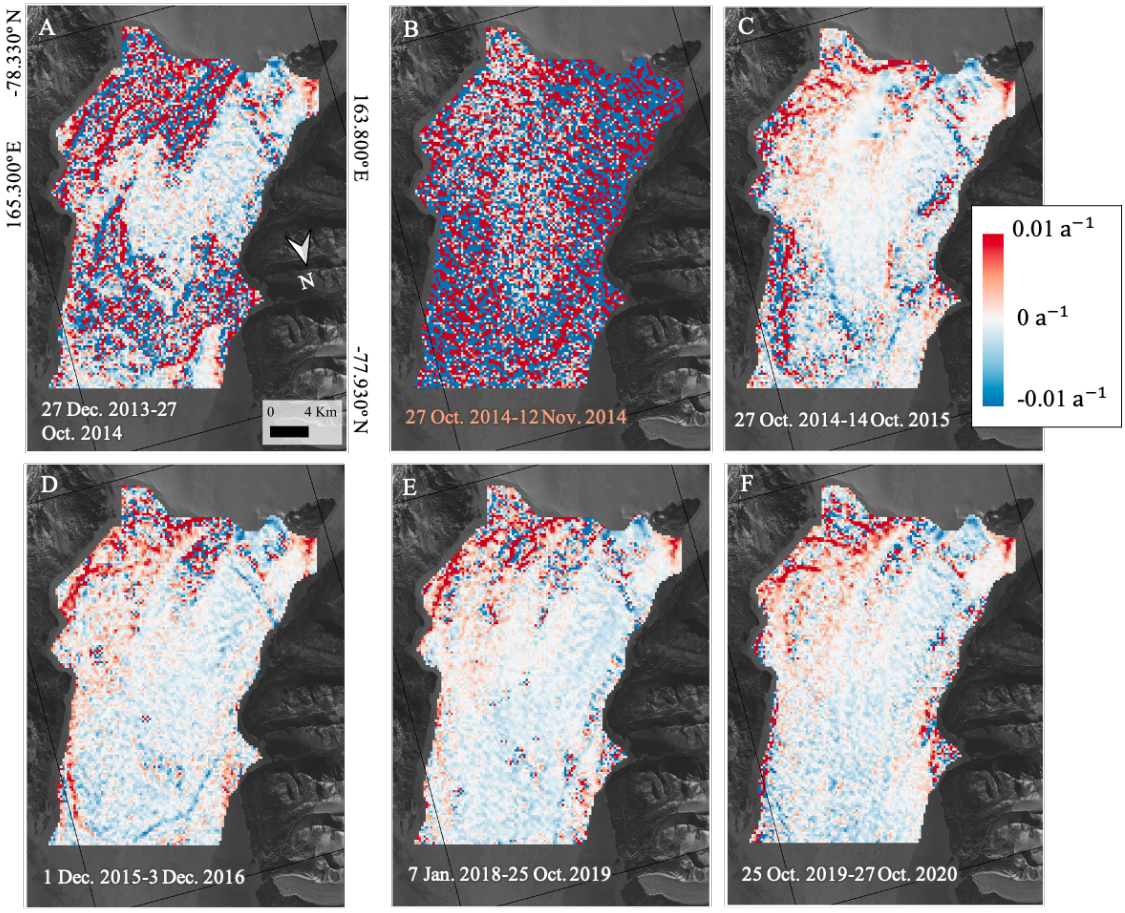

Figure 3.15. Volumetric strain rate on the ice shelf adjacent to Koettlitz Glacier. Panels A-F show the volumetric strain rate calculated for five different time periods spanning 2013 – 2020. Higher magnitude volumetric strain rate values are more abundant along the margins of the study area, while lower magnitude values are concentrated towards the center of the study area.

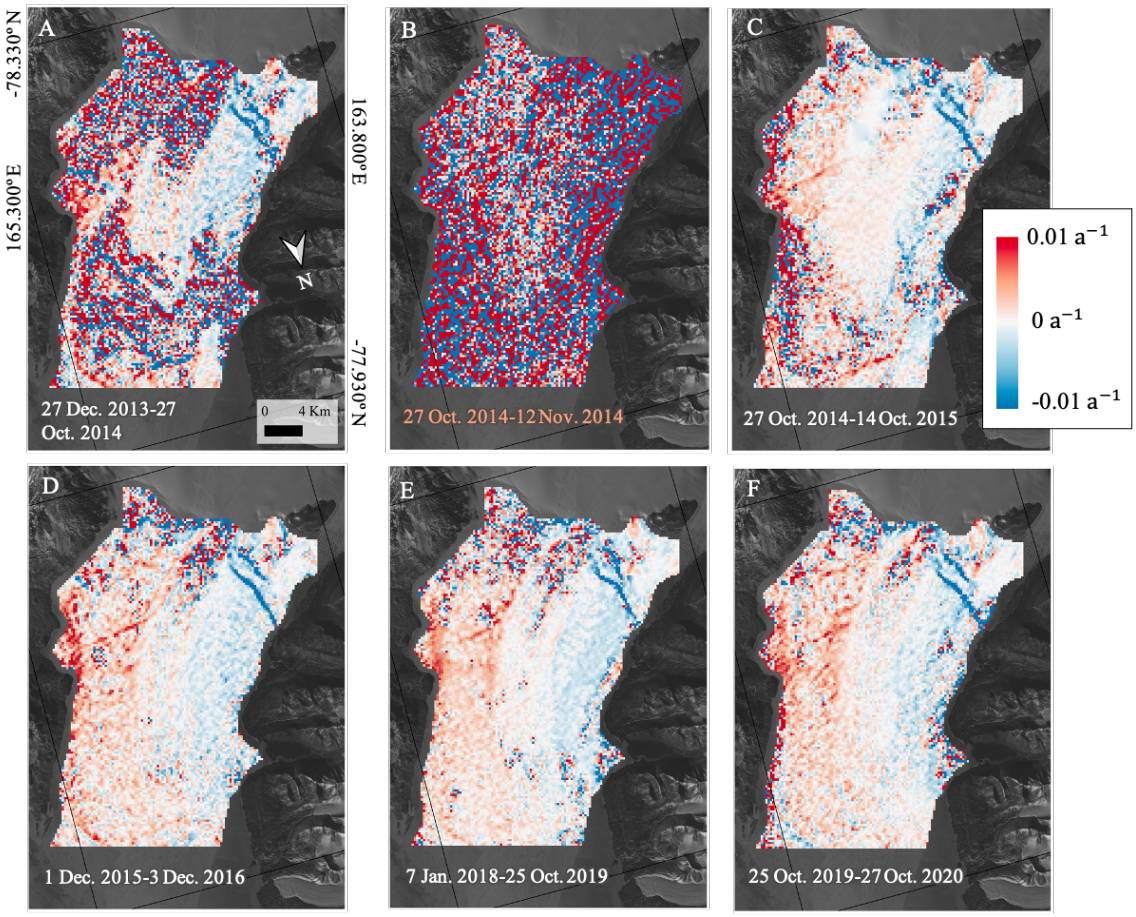

Figure 3.16. Shear strain rate on the ice shelf adjacent to Koettlitz Glacier. Panels A-F show the shear strain rate calculated for five different time periods spanning 2013 – 2020. Larger magnitude shear strain rate values are found along the margins of the study area while smaller values occur nearer the center.

In the Windless Bight region, most of the volumetric strain rate values range from -0.04 a^{-1} – 0.04 a^{-1} (Fig. 3.17). The flow patterns from the glaciers are distinguishable near the grounding line, with north-south contraction at the grounding line, and decreasing magnitude with distance from the grounding line. North-south expansion occurs at the margins of the faster outflow channels of Terror and Aurora Glaciers, and the slower flowing ice in between the two channels (Figs. 3.17). The shear strain rate values in Windless Bight fall within the same range as the volumetric strain rate values (Figs 3.18). The ice flowing from the main glacier channels experiences negative left lateral shearing, with magnitude decreasing with distance from the grounding line (Fig. 3.18), while the area between the outflow from Terror and Aurora Glaciers has a near-zero shear strain rate. The western margin with ice flowing off Aurora Glacier experiences negative left lateral shearing, while the eastern side adjacent to outflow from Terror Glacier undergoes positive right-

lateral shearing. The strain rate patterns indicate that the velocity is highest along the outflow from Terror and Aurora Glaciers, and slowest in the region in between, supporting the convergence of ice seen in the velocity vectors. Also, the greatest velocity gradient occurs crossing the grounding line, and between the two glacier outflows and the more stagnant ice in between.

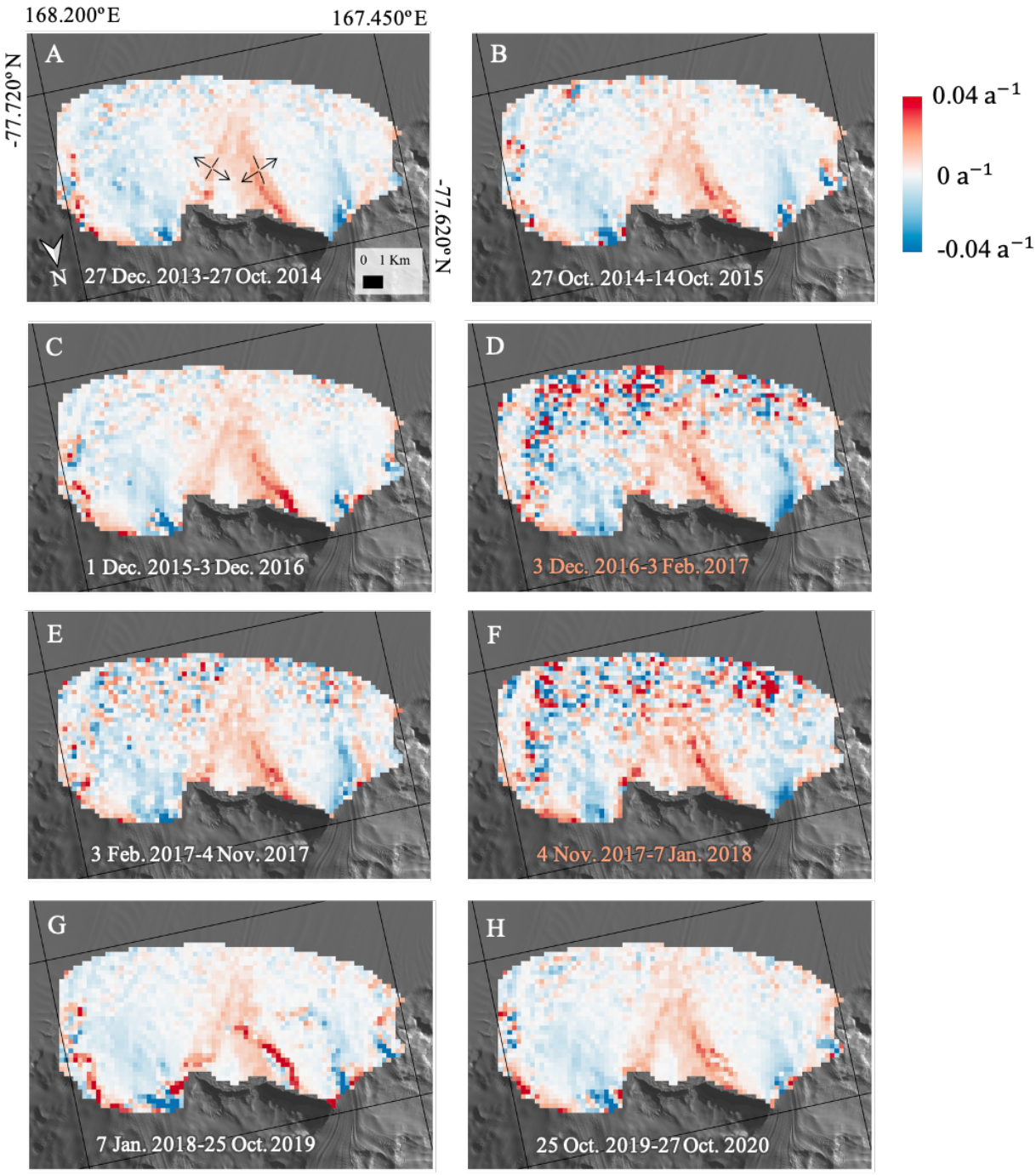

Figure 3.17. Volumetric strain rate on the ice shelf in the Windless Bight region. Panels A-F show the volumetric strain rate calculated for five different time periods spanning 2013 – 2020. The arrows and perpendicular lines in panel A indicate the direction of ice expansion.

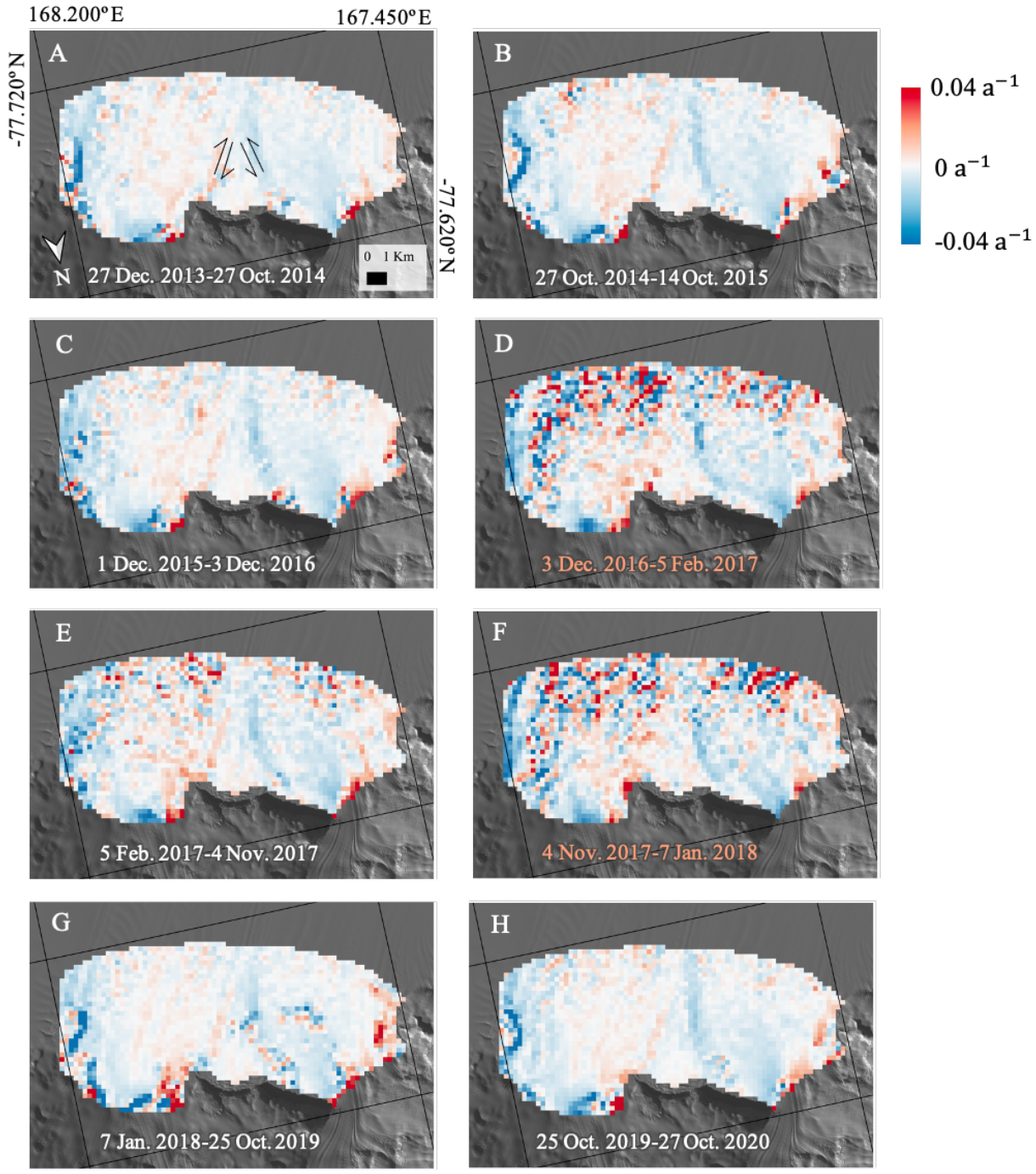

Figure. 3.18. Shear strain rate on the ice shelf in the Windless Bight region. Panels A-F show the shear strain rate calculated for five different time periods spanning 2013 – 2020. The black arrows in panel A indicate the direction of shearing.

3.4.7. Identifying surface melt

To quantify the change in surface melt across the study site, I applied the NDLI ratio to Landsat 8 imagery, also used for velocity calculations. While this ratio should exploit the differences in wavelength reflectance between the red and NIR bands on water, ice, and rock, the resulting NDLI imagery did not agree with the results of prior studies (e.g. Morriss et al., 2013; Schild et al., 2016). Specifically, in comparing what should have appeared dark (rock, red box; Fig. 3.19) to what should have appeared bright (water, purple box), both surfaces instead reflect very similar energy in both the infrared and red range, and consequently appear indistinguishable in the NDLI imagery. Additionally, sea ice should have a brightness between that of the surface water and the rocks, but instead appears comparable to the very bright rocks (sea ice, yellow box). The failure of this method to correctly identify surface water, and the misidentification of both bedrock and sea ice suggests that the atmospheric correction used in post-processing to obtain surface reflectance values is not well calibrated in this region. Thus, NDLI is not a viable method in this environment, and measurements of surface melt timing, duration, location, and area were not calculated.

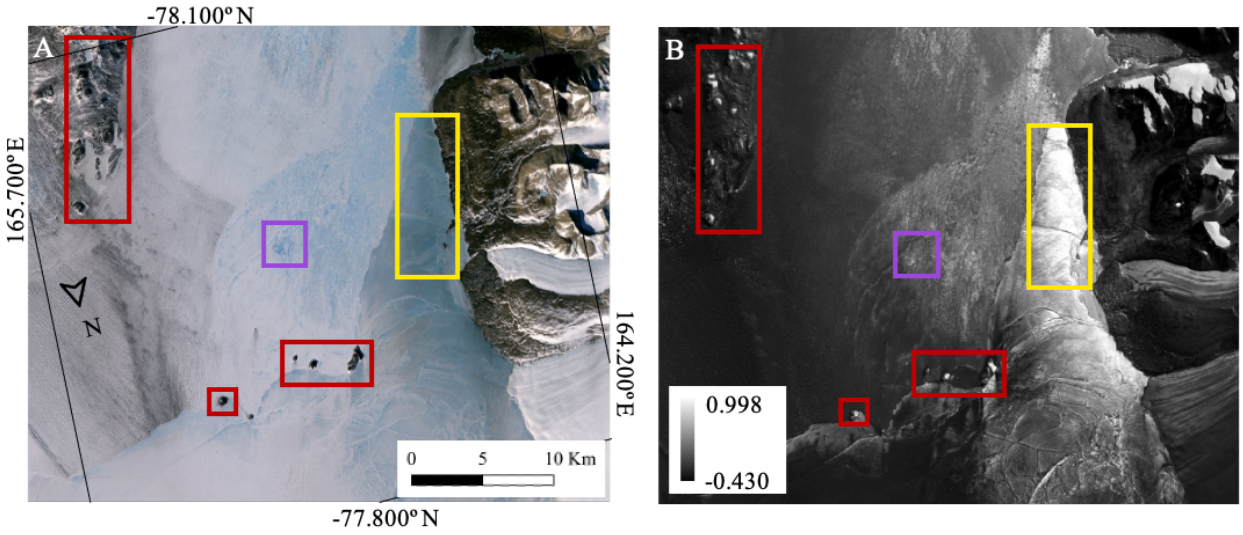

Figure 3.19. Example of poorly calibrated surface reflectance, resulting in false NDLI values on MIS. Panel A shows a true-color Landsat 8 image of the ice shelf edge on the north side of Koettlitz Glacier, and panel B shows the NDLI image. The red boxes identifying rock features in the landscape, the purple box identifies surface melt pooling, and the yellow box identifies sea ice.

3.5 Discussion

3.5.1. Comparison to other data

Surface velocity geospatial patterns presented in this chapter broadly agree with the 20-year annual average MEaSUREs results (Rignot et al., 2017). Both my and MEaSUREs's results show an increase in velocity through the narrowest portions of Terror and Aurora Glacier. Due to limitations in data coverage, direct comparisons between velocity values could not be calculated, but overall MEaSUREs velocity broadly agrees with the baseline average values calculated here, to within 19%.

3.5.2. Surface velocity patterns

Each of the three methods of surface speed analysis (total average speed, transect speed, and speed distribution) reveal greater summer velocity magnitudes than annual velocity magnitudes, and much more seasonal variability on the ice shelf than the glaciers. However, in comparing the average speed of the tributary glaciers relative to the ice shelf, two relationships are distinguishable: one in which the ice shelf dampens the summer effects on the glaciers (Terror and Aurora), and the other in which the glacier and ice shelf respond in concert (Koettlitz). At Terror Glacier, the annual ice shelf speed is 16% - 43% more than the annual glacier speed, however, in the summer, the ice shelf speed increases to 70% more than the glacier speed (Fig. 3.20 A). At Aurora Glacier, a similar trend emerges where the annual ice shelf surface speed is 23% - 47% larger than the annual glacier speed, and the summer average speed is 72% greater than the glacier (Fig. 3.20 B), suggesting the ice shelf may be dampening the summer changes. However, in the Koettlitz region, there are comparable seasonal velocity changes in both the glacier and the ice shelf speed, with the average annual ice shelf speed 27% - 43% greater than the average annual glacier speed, and the average summer ice shelf speed 27% greater than the glacier speed (Fig. 3.20 C), suggesting the glacier and ice shelf respond in tandem to seasonal variability in driving forces. When looking at centerline averages, which are less dependent upon user-defined study areas, the trends in glacier-ice shelf surface speeds are

very similar, except there is a greater difference between the summer ice shelf and glacier speeds in the Koettlitz region, and faster glacier speeds than ice shelf speeds on Terror and Aurora Glaciers (Fig. 3.21; Table 3.2). The differences in the relationship between the ice shelf and tributary glaciers between the methods likely stem from the inclusion of peripheral ice shelf data, which is not proportionally represented in the centerline transects.

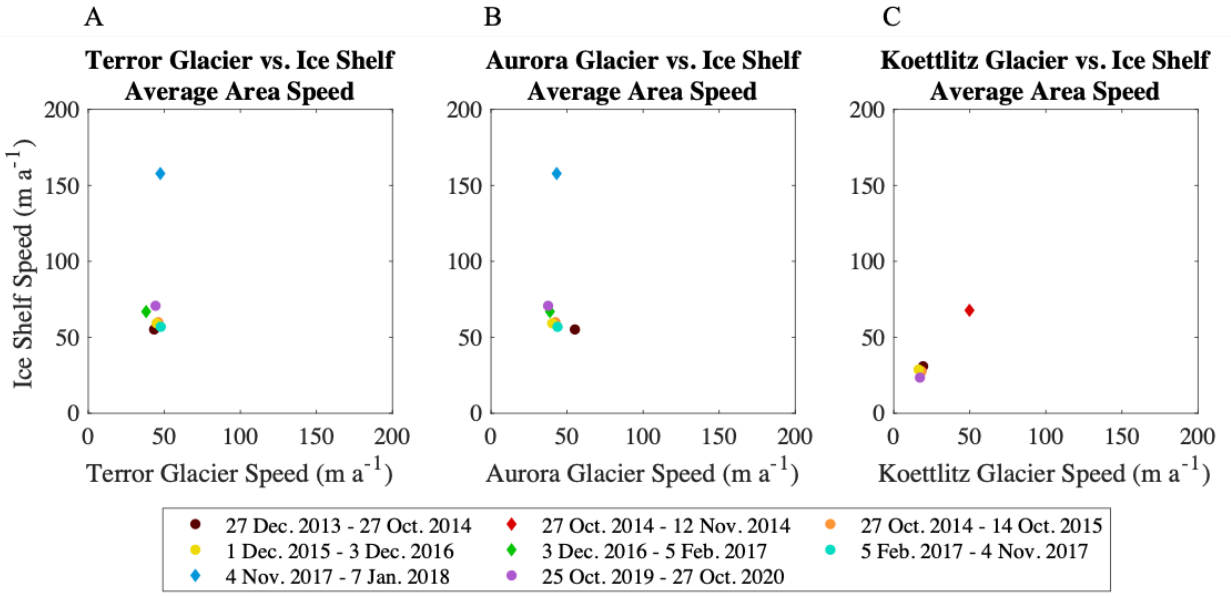

Figure 3.20. Comparing average surface speed on tributary glaciers to adjacent MIS area. Each colored point refers to a different time period. The circles represent time periods that include the winter, while the triangles represent those time periods that only span the summer season. The panels correspond to each of the three tributary glaciers, Terror (A), Aurora (B), and Koettlitz (C), and their adjacent ice shelf area.

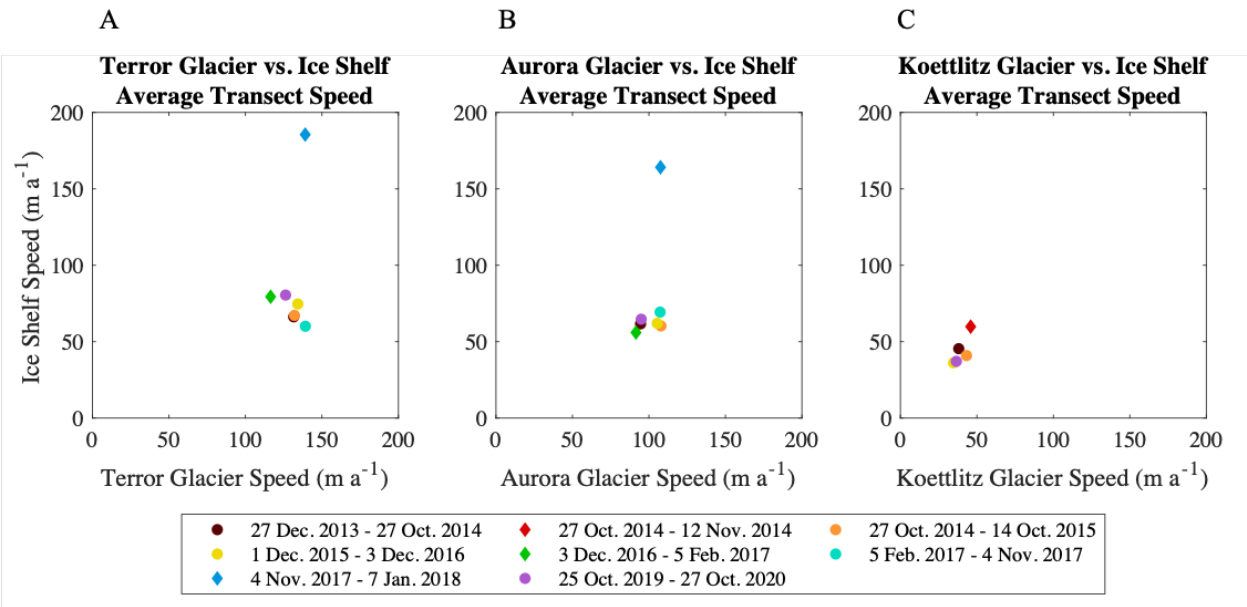

Figure 3.21. Comparing average centerline transect surface speed on tributary glaciers to adjacent MIS area. Each colored point refers to a different time period. The circles represent time periods that include the winter, while the triangles represent those time periods that only span the summer season. The panels correspond to each of the three tributary glaciers, Terror (A), Aurora (B), and Koettlitz (C), and their adjacent ice shelf area.

	Aurora Glacier	Aurora Ice Shelf	% Difference	Terror Glacier	Terror Ice Shelf	% Difference	Koettlitz Glacier	Koettlitz Ice Shelf	% Difference	Method
27 Dec. 2013 - 27 Oct. 2014	42	55	24	43	55	21	19	31	38	A
	95	62	35	132	66	50	38	45	16	T
27 Oct. 2014 - 12 Nov. 2014							50	68	27	A
							46	60	23	T
27 Oct. 2014 - 14 Dec. 2015	42	60	29	46	60	23	18	28	34	A
	108	60	44	132	67	49	43	41	5	T
1 Dec. 2015 - 3 Dec. 2016	40	59	32	45	59	24	16	29	43	A
	105	62	41	134	75	44	35	36	4	T
3 Dec. 2016 - 5 Feb. 2017	39	67	42	38	67	43				A
	92	56	39	116	79	32				T
5 Feb. 2017 - 4 Nov. 2017	44	57	23	48	57	16				A
	107	69	35	139	60	57				T
4 Nov. 2017 - 7 Jan. 2018	43	158	73	47	158	70				A
	108	164	34	186	139	25				T
25 Oct. 2019 - 27 Oct. 2020	38	71	47	44	71	37	17	23	27	A
	95	65	32	126	80	36	37	37	2	T

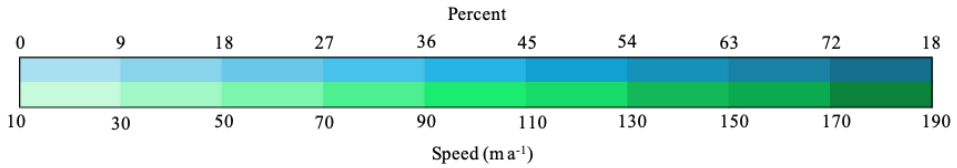

Table 3.2. Tributary glacier and ice shelf area averages, centerline transect averages, and glacier-ice shelf percent difference. The far-right column "Method" indicates whether the data stem from the area average (A) or the transect average (T).

The two different relationships observed between glaciers and ice shelves across our study site suggest that while each location may be experiencing similar environmental forcings, each system experiences different driving forces related to both environmental and physical variables. All of these variables likely contribute to the tendency of each of these glacier-ice shelf systems to preferentially align with one of these two regimes, however common physical features, such as grounded ice and ice composition, likely play a lesser role. I hypothesize that the difference in glacier-ice shelf behavior of the two regimes observed across the study site stems from three primary controls: (1) the proximity of bedrock features restricting ice shelf flow, (2) the number of tributary glaciers, and (3) spatial variability in ocean currents and consequently basal melting at the ice-ocean boundary. Windless Bight has two tributary glaciers flowing into it (Terror and Aurora), which are set farther back from the ice shelf front, and thus allows for more spatial variability or dispersion of warm ocean currents. Koettlitz is the only glacier that flows into its ice shelf area and is isolated from the rest of the ice shelf by Brown Peninsula, thereby decreasing the volume of ice supplying the ice shelf. Koettlitz is also located in a region of the ice shelf closer to the front and that is isolated from the rest of the ice shelf by Brown Peninsula, allowing for minimal spatial dispersion of ocean water.

3.5.3. Future work

Surface velocities on Koettlitz, Terror, and Aurora Glaciers, and their adjacent ice shelf areas revealed annual and seasonal patterns, and two relationships for glacier-ice shelf interactions. However, to resolve sub-seasonal changes, and test the scope of these two regimes across multiple seasons and locations, additional data are needed. To test my hypothesis concerning driving controls, *in situ* ocean temperature measurements beneath the ice shelf are needed, along with atmospheric data, additional study sites with variable ice shelf sizes, numbers of tributary glaciers, and distances from the ocean. To evaluate and refine the long-term behavior of the seasonal and annual glacier-ice shelf relationship, as well as quantify the impact of climate-driven changes on this relationship, data spanning both a longer time scale and at a finer temporal resolution is required. Additionally, increased calibration of coastal Antarctic remote sensing

imagery would enable analysis of surface melt, which could also be considered a driver of seasonal variability in surface velocity.

3.6. Conclusion

Ice shelves provide a buttressing force against the flow of glaciers, restricting the mass loss to the ocean, and consequently regulating the rate of Antarctica's contribution to global sea level rise. Here I focused on the surface velocity of MIS and its tributary glaciers between 2013 – 2020. Using results from COSI-Corr, ITS_LIVE, and GoLIVE, I found greater surface speeds during the summer and smaller speeds during the winter and across annual time scales. The area average speed and the speed distribution both reveal larger magnitude ice shelf velocities than glacier velocities, while the centerline transects show larger glacier speeds, highlighting the method-dependency of these types of velocity studies, as well as the difficulties of classifying the surface velocity of this dynamic system. Comparison of glacier-ice shelf behavior reveals two ice shelf-glacier regimes: (1) seasonal fluctuation of both the ice shelf and the tributary glacier speeds, and (2) seasonal fluctuation of the ice shelf speed and consistent tributary glacier speeds, suggesting spatial variability in location-dependent driving forces. Future work should focus on combining remotely sensed data with *in situ* measurements to resolve sub-seasonal glacier-ice shelf behavior changes. These findings demonstrate the importance of the physical environment in controlling glacier-ice shelf behavior, and necessitates the inclusion of this relationship in predictive models.

3.7. Acknowledgements

Funding for this work was supported by the National Science Foundation Office of Polar Programs award 1842021, and the University of Maine School of Earth and Climate Sciences Teaching Assistantship.

CHAPTER FOUR

CONCLUSION

4.1. Summary

This work provides insight into the dynamic relationship between McMurdo Ice Shelf (MIS) and its tributary glaciers. McMurdo Ice Shelf provides a buffer to both its tributary glaciers, as well as the northwest corner of Ross Ice Shelf, into which glaciers from both East and West Antarctica flow. It also serves as a runway for planes arriving at both the McMurdo Station (United States) and Scott Base (New Zealand), thus playing a critical role in the logistics of the scientific work conducted by these two countries. Concerningly, MIS is vulnerable to collapse due to its thinness and consequential susceptibility to subglacial melt, understanding the transfer of mass from grounded glaciers to floating ice shelf is essential in predicting its longevity.

The results presented in chapter two identify a key logistics vulnerability in Pegasus Road, which connects the runways on MIS to the research bases on Ross Island. Further retreat of MIS to Hut Point Peninsula could impact the road segment connecting the ice shelf to Hut Point Peninsula, making McMurdo Station and Scott Base inaccessible. We suggest relocating the road to connect with Ross Island at a point farther northeast, bypassing this area of high vulnerability. Chapter three examines the relationship between surface velocity on MIS and its tributary glaciers using three methods (average surface velocity, velocity along central transects, and velocity frequency distribution), identifying seasonal and annual patterns. All three methods reveal greater overall surface speeds during the summer and slower speeds in the winter, with the greatest speeds located near the grounding line along the central flow line. In the Windless Bight region, the seasonal speed fluctuation is seen most strongly on the ice shelf, and to a lesser extent on the tributary glaciers whose velocities remain more consistent throughout the year, while in the Koettlitz region, the surface speed of both glacier and ice shelf fluctuates together. Therefore, the difference in seasonal behavior

between regions suggests that driving forces vary spatially across MIS, creating these two regimes. I hypothesize that the most prominent controls creating these two regimes include the degree of restriction by bedrock features, the number of tributary glaciers flowing into each ice shelf region, and differences in ocean circulation and temperature.

4.2. Future work

While this research provides a foundation to understanding the connection between MIS and its tributary glaciers, additional data would help further explore this relationship. For instance, a lack of agreement between several of the COSI-Corr and ITS_LIVE/GoLIVE datasets in the Koettlitz region made it challenging to determine which dataset is a more accurate representation of surface velocity. Therefore, time periods were not included, and less data was available to analyze the Koettlitz Glacier-ice shelf relationship. The availability of *in situ* GPS measurements spanning both the tributary glacier and the adjacent ice shelf could resolve this discrepancy and help to refine the feature tracking algorithms, and therefore ultimately increase our understanding of the potential long-term stability of this system.

Gathering thickness measurements in the terminus region of each glacier would provide the information necessary to quantify the mass transfer from the glaciers to the ice shelf, linking these velocity and elevation change results to sea level contribution. Previous MIS thickness measurements have produced conflicting results, especially with regard to the mass lost to subglacial melt. Collecting *in situ* measurements could resolve some of these uncertainties; using seismic surveying, capable of penetrating the meteoric ice-marine ice interface and reaching the marine ice-ocean interface could provide the clarifying data. Repeat measurements of ice shelf thickness would allow quantification of basal melt rates and identification of specific regions especially susceptible to melt from warm water circulation. This thesis aimed to quantify surface changes on MIS by examining the relationship between MIS and its tributary glaciers through analyzing changes in ice surface elevation, and surface velocity between 2013 – 2020, and highlights the

vitality of understanding the glacier-ice shelf relationship in predicting the future contribution of ice shelf tributary glaciers to sea level rise.

BIBLIOGRAPHY

Anandakrishnan, S., Voigt, D. E., Alley, R. B., & King, M. A. (2003). Ice stream D flow speed is strongly modulated by the tide beneath the Ross Ice Shelf. *Geophysical Research Letters*, *30*(7), Article 7. https://doi.org/10.1029/2002GL016329

Arcone, S. A., Lever, J. H., Ray, L. E., Walker, B. S., Hamilton, G., & Kaluzienski, L. (2016). Ground-penetrating radar profiles of the McMurdo Shear Zone, Antarctica, acquired with an unmanned rover: Interpretation of crevasses, fractures, and folds within firn and marine ice. *GEOPHYSICS*, *81*(1), WA21–WA34. https://doi.org/10.1190/geo2015-0132.1

Ayoub, F., Leprince, S., & Avouac, J.-P. (2015). *User's Guide to COSI-CORR Co-registration of Optically Sensed Images and Correlation* (p. 49).

Bamber, J. L., Westaway, R. M., Marzeion, B., & Wouters, B. (2018). The land ice contribution to sea level during the satellite era. *Environmental Research Letters*, *13*(6), 063008. https://doi.org/10.1088/1748-9326/aac2f0

Banwell, A. F., MacAyeal, D. R., & Sergienko, O. V. (2013). Breakup of the Larsen B Ice Shelf triggered by chain reaction drainage of supraglacial lakes. *Geophysical Research Letters*, *40*(22), 5872–5876. https://doi.org/10.1002/2013GL057694

Banwell, A. F., Willis, I. C., Macdonald, G. J., Goodsell, B., Mayer, D. P., Powell, A., & Macayeal, D. R. (2017). Calving and rifting on the McMurdo Ice Shelf, Antarctica. *Annals of Glaciology*, *58*(75pt1), 78–87. https://doi.org/10.1017/aog.2017.12

Bartholomew, I., Nienow, P., Mair, D., Hubbard, A., King, M. A., & Sole, A. (2010). Seasonal evolution of subglacial drainage and acceleration in a Greenland outlet glacier. *Nature Geoscience*, *3*(6), 408–411. https://doi.org/10.1038/ngeo863

Berger, S., Favier, L., Drews, R., Derwael, J.-J., & Pattyn, F. (2016). The control of an uncharted pinning point on the flow of an Antarctic ice shelf. *Journal of Glaciology*, *62*(231), 37–45. https://doi.org/10.1017/jog.2016.7

Brunt, K. M., King, M. A., Fricker, H. A., & MacAyeal, D. R. (2010). Flow of the Ross Ice Shelf, Antarctica, is modulated by the ocean tide. *Journal of Glaciology*, *56*(195), 157–161. https://doi.org/10.3189/002214310791190875

Bulthuis, K., Arnst, M., Sun, S., & Pattyn, F. (2019). Uncertainty quantification of the multi-centennial response of the Antarctic ice sheet to climate change. *The Cryosphere*, *13*(4), 1349–1380. https://doi.org/10.5194/tc-13-1349-2019

Campbell, S., Courville, Z., Sinclair, S., & Wilner, J. (2017). Brine, englacial structure and basal properties near the terminus of McMurdo Ice Shelf, Antarctica. *Annals of Glaciology*, *58*(74), 1–11. https://doi.org/10.1017/aog.2017.26

Cazenave, A., Meyssignac, B., Ablain, M., Balmaseda, M., Bamber, J., Barletta, V., Beckley, B., Benveniste, J., Berthier, E., Blazquez, A., Boyer, T., Caceres, D., Chambers, D., Champollion, N., Chao, B., Chen, J., Cheng, L., Church, J. A., Chuter, S., … Wouters, B. (2018). Global sea-level budget 1993-present [Application/pdf]. *Earth System Science Data*, *10*(3), 1551–1590. https://doi.org/10.3929/ETHZ-B-000287786

Cook, A. J., Holland, P. R., Meredith, M. P., Murray, T., Luckman, A., & Vaughan, D. G. (2016). Ocean forcing of glacier retreat in the western Antarctic Peninsula. *Science*, *353*(6296), 283–286. https://doi.org/10.1126/science.aae0017

Das, I., Padman, L., Bell, R. E., Fricker, H. A., Tinto, K. J., Hulbe, C. L., Siddoway, C. S., Dhakal, T., Frearson, N. P., Mosbeux, C., Cordero, S. I., & Siegfried, M. R. (2020). Multidecadal Basal Melt Rates and Structure of the Ross Ice Shelf, Antarctica, Using Airborne Ice Penetrating Radar. *Journal of Geophysical Research: Earth Surface*, *125*(3). https://doi.org/10.1029/2019JF005241

de Juan, J., Elósegui, P., Nettles, M., Larsen, T. B., Davis, J. L., Hamilton, G. S., Stearns, L. A., Andersen, M. L., Ekström, G., Ahlstrøm, A. P., Stenseng, L., Khan, S. A., & Forsberg, R. (2010). Sudden increase in tidal response linked to calving and acceleration at a large Greenland outlet glacier. *Geophysical Research Letters*, *37*(12), n/a-n/a. https://doi.org/10.1029/2010GL043289

DeConto, R. M., & Pollard, D. (2016). Contribution of Antarctica to past and future sea-level rise. *Nature*, *531*(7596), 591–597. https://doi.org/10.1038/nature17145

Doake, C. S. M., Corr, H. F. J., Nicholls, K. W., Gaffikin, A., Jenkins, A., Bertiger, W. I., & King, M. A. (2002). Tide-induced lateral movement of Brunt Ice Shelf, Antarctica. *Geophysical Research Letters*, *29*(8), 67-1-67–4. https://doi.org/10.1029/2001GL014606

Edwards, T. L., Brandon, M. A., Durand, G., Edwards, N. R., Golledge, N. R., Holden, P. B., Nias, I. J., Payne, A. J., Ritz, C., & Wernecke, A. (2019). Revisiting Antarctic ice loss due to marine ice-cliff instability. *Nature*, *566*(7742), 58–64. https://doi.org/10.1038/s41586-019-0901-4

Farinotti, D., Huss, M., Fürst, J. J., Landmann, J., Machguth, H., Maussion, F., & Pandit, A. (2019). A consensus estimate for the ice thickness distribution of all glaciers on Earth. *Nature Geoscience*, *12*(3), 168–173. https://doi.org/10.1038/s41561-019-0300-3

Frederikse, T., Landerer, F., Caron, L., Adhikari, S., Parkes, D., Humphrey, V. W., Dangendorf, S., Hogarth, P., Zanna, L., Cheng, L., & Wu, Y.-H. (2020). The causes of sea-level rise since 1900. *Nature*, *584*(7821), 393–397. https://doi.org/10.1038/s41586-020-2591-3

Gardner, Alex, Fahnestock, Markand, & Scambos, Theodore. (2019). *MEASURES ITS_LIVE Regional Glacier and Ice Sheet Surface Velocities* [Data set]. NASA National Snow and Ice Data Center DAAC. https://doi.org/10.5067/6II6VW8LLWJ7

Glasser, N., Goodsell, B., Copland, L., & Lawson, W. (2006). Debris characteristics and ice-shelf dynamics in the ablation region of the McMurdo Ice Shelf, Antarctica. *Journal of Glaciology*, *52*(177), 223–234. https://doi.org/10.3189/172756506781828692

Hanna, E., Pattyn, F., Navarro, F., Favier, V., Goelzer, H., van den Broeke, M. R., Vizcaino, M., Whitehouse, P. L., Ritz, C., Bulthuis, K., & Smith, B. (2020). Mass balance of the ice sheets and glaciers – Progress since AR5 and challenges. *Earth-Science Reviews*, *201*, 102976. https://doi.org/10.1016/j.earscirev.2019.102976

Heid, T., & Kääb, A. (2012). Evaluation of existing image matching methods for deriving glacier surface displacements globally from optical satellite imagery. *Remote Sensing of Environment*, *118*, 339–355. https://doi.org/10.1016/j.rse.2011.11.024

Heine, A. J. (1967). The McMurdo Ice Shelf, Antarctica: A preliminary report. *New Zealand Journal of Geology and Geophysics*, *10*(2), 474–478. https://doi.org/10.1080/00288306.1967.10426751

Horgan, H. J., Walker, R. T., Anandakrishnan, S., & Alley, R. B. (2011). Surface elevation changes at the front of the Ross Ice Shelf: Implications for basal melting. *Journal of Geophysical Research*, *116*(C2). https://doi.org/10.1029/2010JC006192

Jakobs, C. L., Reijmer, C. H., Kuipers Munneke, P., König-Langlo, G., & van den Broeke, M. R. (2019). Quantifying the snowmelt–albedo feedback at Neumayer Station, East Antarctica. *The Cryosphere*, *13*(5), 1473–1485. https://doi.org/10.5194/tc-13-1473-2019

Jakobs, C. L., Reijmer, C. H., van den Broeke, M. R., van de Berg, W. J., & van Wessem, J. M. (2021). Spatial Variability of the Snowmelt-Albedo Feedback in Antarctica. *Journal of Geophysical Research: Earth Surface*, *126*(2). https://doi.org/10.1029/2020JF005696

Kaluzienski, L., Koons, P., Enderlin, E., Hamilton, G., Courville, Z., & Arcone, S. (2019). Crevasse initiation and history within the McMurdo Shear Zone, Antarctica. *Journal of Glaciology*, *65*(254), 989–999. https://doi.org/10.1017/jog.2019.65

Khazendar, A., Borstad, C. P., Scheuchl, B., Rignot, E., & Seroussi, H. (2015). The evolving instability of the remnant Larsen B Ice Shelf and its tributary glaciers. *Earth and Planetary Science Letters*, *419*, 199–210. https://doi.org/10.1016/j.epsl.2015.03.014

Levermann, A., Winkelmann, R., Nowicki, S., Fastook, J. L., Frieler, K., Greve, R., Hellmer, H. H., Martin, M. A., Meinshausen, M., Mengel, M., Payne, A. J., Pollard, D., Sato, T., Timmermann, R., Wang, W. L., & Bindschadler, R. A. (2014). Projecting Antarctic ice discharge using response functions from SeaRISE ice-sheet models. *Earth System Dynamics*, *5*(2), 271–293. https://doi.org/10.5194/esd-5-271-2014

MacGregor, J. A., Catania, G. A., Conway, H., Schroeder, D. M., Joughin, I., Young, D. A., Kempf, S. D., & Blankenship, D. D. (2013). Weak bed control of the eastern shear margin of Thwaites Glacier, West Antarctica. *Journal of Glaciology*, *59*(217), 900–912.

MacGregor, J. A., Catania, G. A., Markowski, M. S., & Andrews, A. G. (2012). Widespread rifting and retreat of ice-shelf margins in the eastern Amundsen Sea Embayment between 1972 and 2011. *Journal of Glaciology*, *58*(209), 458–466. https://doi.org/10.3189/2012JoG11J262

Mayer, C., & Siegert, M. J. (2000). Numerical modelling of ice-sheet dynamics across the Vostok subglacial lake, central East Antarctica. *Journal of Glaciology*, *46*(153), 197–205. https://doi.org/10.3189/172756500781832981

Meier, M. F., Dyurgerov, M. B., Rick, U. K., O'Neel, S., Pfeffer, W. T., Anderson, R. S., Anderson, S. P., & Glazovsky, A. F. (2007). Glaciers Dominate Eustatic Sea-Level Rise in the 21st Century. *Science*, *317*(5841), 1064–1067. https://doi.org/10.1126/science.1143906

Morlighem, M., Rignot, E., Binder, T., Blankenship, D., Drews, R., Eagles, G., Eisen, O., Ferraccioli, F., Forsberg, R., Fretwell, P., Goel, V., Greenbaum, J. S., Gudmundsson, H., Guo, J., Helm, V., Hofstede, C., Howat, I., Humbert, A., Jokat, W., … Young, D. A. (2020). Deep glacial troughs and stabilizing ridges unveiled beneath the margins of the Antarctic ice sheet. *Nature Geoscience*, *13*(2), 132–137. https://doi.org/10.1038/s41561-019-0510-8

Morlighem, M., Williams, C. N., Rignot, E., An, L., Arndt, J. E., Bamber, J. L., Catania, G., Chauché, N., Dowdeswell, J. A., Dorschel, B., Fenty, I., Hogan, K., Howat, I., Hubbard, A., Jakobsson, M., Jordan, T. M., Kjeldsen, K. K., Millan, R., Mayer, L., … Straneo, F. (2017). BedMachine v3: Complete bed topography and ocean bathymetry mapping of Greenland from multi-beam echo sounding combined with mass conservation. *Geophysical Research Letters*, *44*(21), 11051–11061.

Morriss, B. F., Hawley, R. L., Chipman, J. W., Andrews, L. C., Catania, G. A., Hoffman, M. J., Lüthi, M. P., & Neumann, T. A. (2013). A ten-year record of supraglacial lake evolution and rapid drainage in West Greenland using an automated processing algorithm for multispectral imagery. *The Cryosphere*, *7*(6), 1869–1877. https://doi.org/10.5194/tc-7-1869-2013

Pattyn, F., & Morlighem, M. (2020). The uncertain future of the Antarctic Ice Sheet. *Science*, *367*(6484), 1331–1335. https://doi.org/10.1126/science.aaz5487

Podolskiy, E. A., Sugiyama, S., Funk, M., Walter, F., Genco, R., Tsutaki, S., Minowa, M., & Ripepe, M. (2016). Tide-modulated ice flow variations drive seismicity near the calving front of Bowdoin Glacier, Greenland. *Geophysical Research Letters*, *43*(5), 2036–2044. https://doi.org/10.1002/2016GL067743

Rack, W., Haas, C., & Langhorne, P. J. (2013). Airborne thickness and freeboard measurements over the McMurdo Ice Shelf, Antarctica, and implications for ice density. *Journal of Geophysical Research: Oceans*, *118*(11), 5899–5907. https://doi.org/10.1002/2013JC009084

Reese, R., Gudmundsson, G. H., Levermann, A., & Winkelmann, R. (2018). The far reach of ice-shelf thinning in Antarctica. *Nature Climate Change*, *8*, 7. https://doi.org/10.1038/s41558-017-0020-x

Rignot, E., Bamber, J. L., van den Broeke, M. R., Davis, C., Li, Y., van de Berg, W. J., & van Meijgaard, E. (2008). Recent Antarctic ice mass loss from radar interferometry and regional climate modelling. *Nature Geoscience*, *1*(2), 106–110. https://doi.org/10.1038/ngeo102

Rignot, E., Jacobs, S., Mouginot, J., & Scheuchl, B. (2013). Ice-Shelf Melting Around Antarctica. *Science*, *341*(6143), 266–270. https://doi.org/10.1126/science.1235798

Rignot, E., Mouginot, J., & Scheuchl, B. (2017). *MEaSUREs InSAR-Based Antarctica Ice Velocity Map, Version 2* [Data set]. NASA National Snow and Ice Data Center DAAC. https://doi.org/10.5067/D7GK8F5J8M8R

Rignot, E., Mouginot, J., Scheuchl, B., van den Broeke, M., van Wessem, M. J., & Morlighem, M. (2019). Four decades of Antarctic Ice Sheet mass balance from 1979–2017. *Proceedings of the National Academy of Sciences*, *116*(4), 1095–1103. https://doi.org/10.1073/pnas.1812883116

Royston, S., & Gudmundsson, G. H. (2016). Changes in ice-shelf buttressing following the collapse of Larsen A Ice Shelf, Antarctica, and the resulting impact on tributaries. *Journal of Glaciology*, *62*(235), 905–911. https://doi.org/10.1017/jog.2016.77

Scambos, T. A. (2004). Glacier acceleration and thinning after ice shelf collapse in the Larsen B embayment, Antarctica. *Geophysical Research Letters*, *31*(18), L18402. https://doi.org/10.1029/2004GL020670

Scambos, T., Fahnestock, M., Moon, T., Gardner, A., & Klinger, M. (2016). *Global Land Ice Velocity Extraction from Landsat 8 (GoLive)* (1st ed.). NSIDC: National Snow and Ice Data Center.

Schild, K. M., Hawley, R. L., & Morriss, B. F. (2016). Subglacial hydrology at Rink Isbræ, West Greenland inferred from sediment plume appearance. *Annals of Glaciology*, *57*(72), 118–127. https://doi.org/10.1017/aog.2016.1

Smith, B., Fricker, H. A., Gardner, A. S., Medley, B., Nilsson, J., Paolo, F. S., Holschuh, N., Adusumilli, S., Brunt, K., Csatho, B., Harbeck, K., Markus, T., Neumann, T., Siegfried, M. R., & Zwally, H. J. (2020). Pervasive ice sheet mass loss reflects competing ocean and atmosphere processes. *Science*, eaaz5845. https://doi.org/10.1126/science.aaz5845

Spence, P., Holmes, R. M., Hogg, A. McC., Griffies, S. M., Stewart, K. D., & England, M. H. (2017). Localized rapid warming of West Antarctic subsurface waters by remote winds. *Nature Climate Change*, *7*(8), 595–603. https://doi.org/10.1038/nclimate3335

Stern, A. A., Dinniman, M. S., Zagorodnov, V., Tyler, S. W., & Holland, D. M. (2013). Intrusion of warm surface water beneath the McMurdo Ice Shelf, Antarctica. *Journal of*

Geophysical Research: Oceans, *118*(12), 7036–7048. https://doi.org/10.1002/2013JC008842

Sugiyama, S., Sakakibara, D., Tsutaki, S., Maruyama, M., & Sawagaki, T. (2015). Glacier dynamics near the calving front of Bowdoin Glacier, northwestern Greenland. *Journal of Glaciology*, *61*(226), 223–232. https://doi.org/10.3189/2015JoG14J127

Tikku, A. A., Bell, R. E., Studinger, M., Clarke, G. K. C., Tabacco, I., & Ferraccioli, F. (2005). Influx of meltwater to subglacial Lake Concordia, East Antarctica. *Journal of Glaciology*, *51*(172), 96–104. https://doi.org/10.3189/172756505781829494

Tinto, K. J., Padman, L., Siddoway, C. S., Springer, S. R., Fricker, H. A., Das, I., Caratori Tontini, F., Porter, D. F., Frearson, N. P., Howard, S. L., Siegfried, M. R., Mosbeux, C., Becker, M. K., Bertinato, C., Boghosian, A., Brady, N., Burton, B. L., Chu, W., Cordero, S. I., … Bell, R. E. (2019). Ross Ice Shelf response to climate driven by the tectonic imprint on seafloor bathymetry. *Nature Geoscience*, *12*(6), 441–449. https://doi.org/10.1038/s41561-019-0370-2

van der Veen, C. J. (2007). Fracture propagation as means of rapidly transferring surface meltwater to the base of glaciers. *Geophysical Research Letters*, *34*(1), L01501. https://doi.org/10.1029/2006GL028385

Zemp, M., Huss, M., Thibert, E., Eckert, N., McNabb, R., Huber, J., Barandun, M., Machguth, H., Nussbaumer, S. U., Gärtner-Roer, I., Thomson, L., Paul, F., Maussion, F., Kutuzov, S., & Cogley, J. G. (2019). Global glacier mass changes and their contributions to sea-level rise from 1961 to 2016. *Nature*, *568*(7752), 382–386. https://doi.org/10.1038/s41586-019-1071-0

APPENDIX

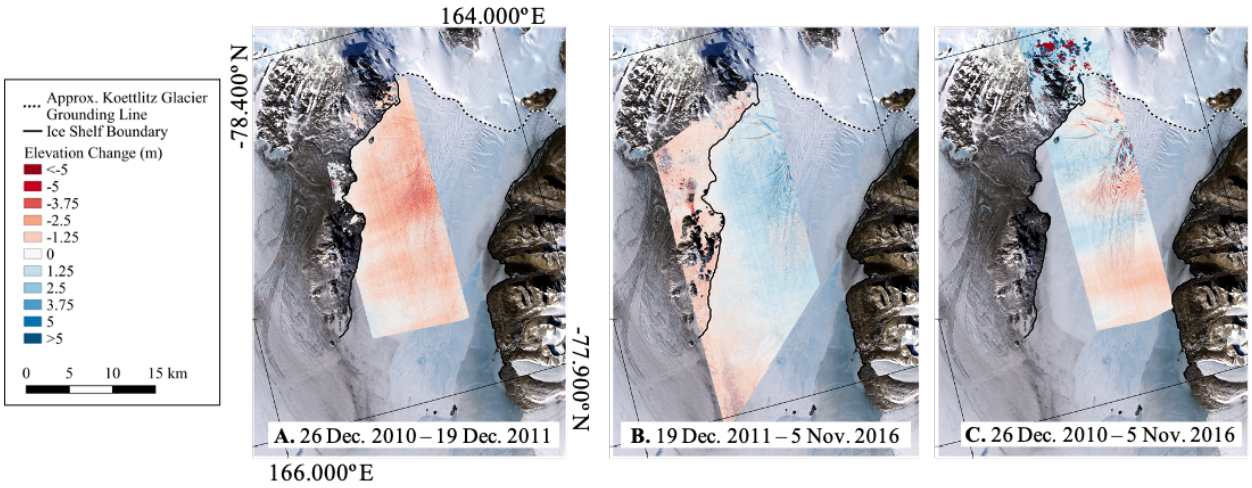

Figure A.1. Surface elevation change on McMurdo Ice Shelf (MIS) adjacent to Koettlitz Glacier. Elevation change between three dates, 26 Dec. 2010 – 19 Dec. 2011, 19 Dec. 2011 – 5 Nov. 2016, 26 Dec. 2010 – 5 Nov. 2016, calculated by differencing DEMs. The solid black line marks the boundary between the ice shelf and land, while the black and white dashed line indicates the approximate location of the Koettlitz Glacier grounding line. The banding visible on panels A and C results from poor calibration of sensors on the WorldView satellite, from which the DEMs were derived. Background image from Landsat 8 captured on 27 Oct. 2020.

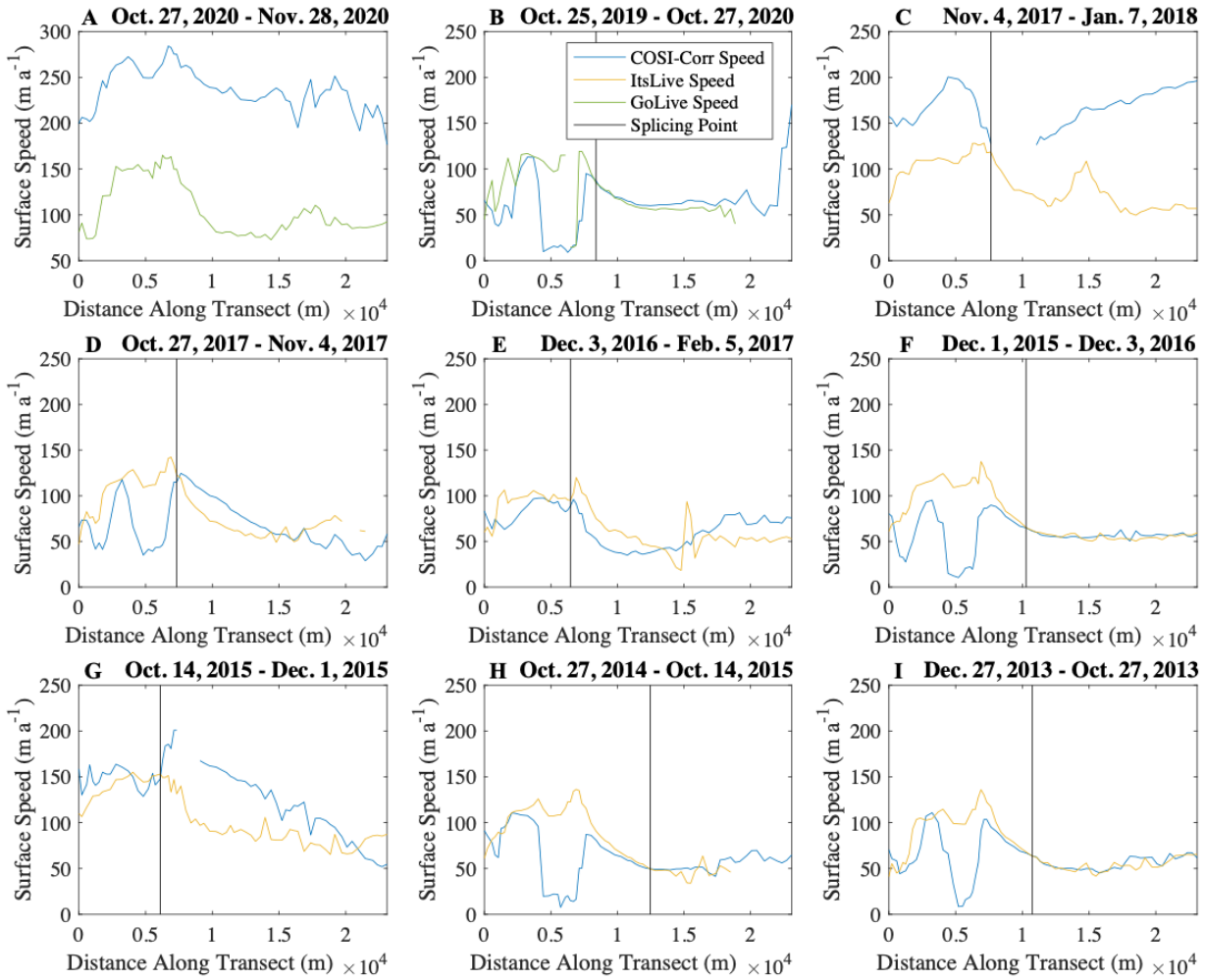

Figure A.2. Location of COSI-Corr and ITS_LIVE/GoLIVE data splicing along the Aurora Glacier transect. The blue line indicates the speed along a transect on COSI-Corr data, the yellow line indicates the speed along a transect on ITS_LIVE data, the green line indicates the speed along a transect on GoLIVE data, and the black vertical line indicates the distance along the transect at which the two datasets were spliced. Each panel (A-I) represents a different time period over which data was available, spanning 2013 – 2020. The time periods where the two datasets have no overlapping speed values were eliminated, as which dataset was more accurate was unknown.

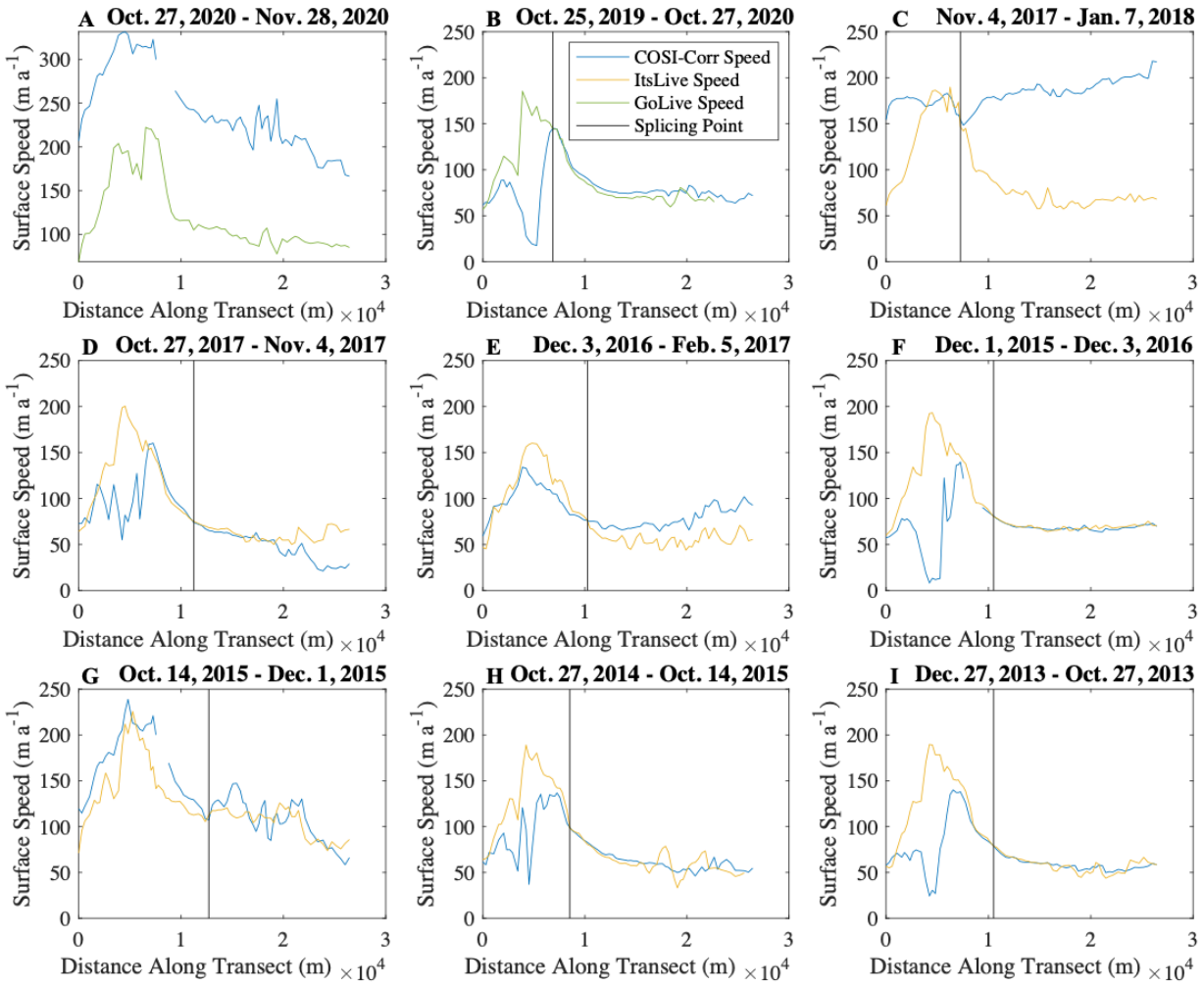

Figure A.3. Location of COSI-Corr and ITS_LIVE/GoLIVE data splicing along the Terror Glacier transect. The blue line indicates the speed along a transect on COSI-Corr data, the yellow line indicates the speed along a transect on ITS_LIVE data, the green line indicates the speed along a transect on GoLIVE data, and the black vertical line indicates the distance along the transect at which the two datasets were spliced. Each panel (A-I) represents a different time period over which data was available, spanning 2013 – 2020. The time periods where the two datasets have no overlapping speed values were eliminated, as which dataset was more accurate was unknown.

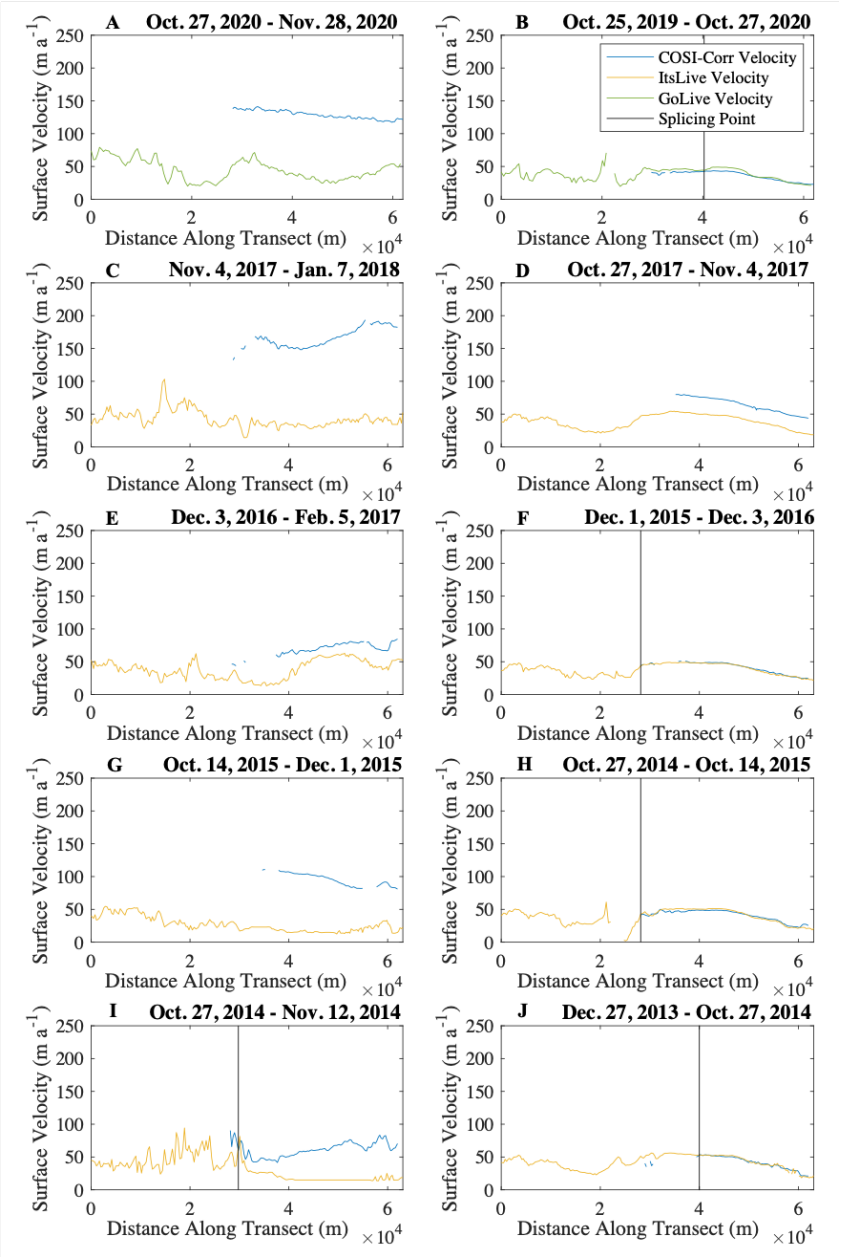

Figure A.4. Location of COSI-Corr and ITS_LIVE/GoLIVE data splicing along the Koettlitz Glacier transect. The blue line indicates the speed along a transect on COSI-Corr data, the yellow line indicates the speed along a transect on ITS_LIVE data, the green line indicates the speed along a transect on GoLIVE data, and the black vertical line indicates the distance along the transect at which the two datasets were spliced. Each panel (A-I) represents a different time period over which data was available, spanning 2013 – 2020. The time periods where the two datasets have no overlapping speed values were eliminated, as which dataset was more accurate was unknown.

Imagery	File/Scene Name	Figures Used In
GoLIVE	L8_053_116_368_2019_298_2020_301_T2T2_v1.1	3.3; 3.6; 3.7; 3.8; 3.9; 3.10; 3.11; 3.12; 3.14; 3.20; 3.21; A.2; A.3; A.4
GoLIVE	L8_053_116_032_2020_301_2020_333_T2T2_v1.1	A.2; A.3; A.4
ITS_LIVE	LC08_L1GT_053116_20141027_20170418_01_T2_X_LC08_L1GT_053116_20131227_20170427_01_T2_G0240V01_P038	3.6; 3.7; 3.8; 3.9; 3.10; 3.11; 3.12; 3.14; 3.20; 3.21; A.2; A.3; A.4
ITS_LIVE	LC08_L1GT_053116_20141112_20170417_01_T2_X_LC08_L1GT_053116_20141027_20170418_01_T2_G0240V01_P084	3.6; 3.8; 3.9; 3.11; 3.12; 3.20; 3.21; A.4
ITS_LIVE	LC08_L1GT_053116_20151014_20170403_01_T2_X_LC08_L1GT_053116_20141027_20170418_01_T2_G0240V01_P047	3.6; 3.7; 3.8; 3.9; 3.10; 3.11; 3.12; 3.14; 3.20; 3.21; A.2; A.3; A.4
ITS_LIVE	LC08_L1GT_053116_20151201_20170401_01_T2_X_LC08_L1GT_053116_20151014_20170403_01_T2_G0240V01_P091	3.7; 3.8; 3.14; A.2; A.3; A,3
ITS_LIVE	LC08_L1GT_053116_20161203_20170317_01_T2_X_LC08_L1GT_053116_20151201_20170401_01_T2_G0240V01_P052	3.6; 3.7; 3.8; 3.9; 3.10; 3.11; 3.12; 3.14; 3.20; 3.21; A.2; A.3; A.4
ITS_LIVE	LC08_L1GT_053116_20170205_20170216_01_T2_X_LC08_L1GT_053116_20161203_20170317_01_T2_G0240V01_P092	3.7; 3.8; 3.10; 3.11; 3.12; 3.14; 3.20; 3.21; A.2; A.3; A.4
ITS_LIVE	LC08_L1GT_053116_20171104_20171120_01_T2_X_LC08_L1GT_053116_20170205_20170216_01_T2_G0240V01_P049	3.7; 3.8; 3.10; 3.11; 3.12; 3.14; 3.20; 3.21; A.2; A.3; A.4
ITS_LIVE	LC08_L1GT_053116_20180107_20180119_01_T2_X_LC08_L1GT_053116_20171104_20171120_01_T2_G0240V01_P093	3.7; 3.8; 3.10; 3.11; 3.12; 3.14; 3.20; 3.21; A.2; A.3; A.4
Landsat 8	LC08_L1GT_053116_20131227_20170427_01_T2	3.6; 3.7; 3.8; 3.9; 3.10; 3.11; 3.12; 3.13; 3.15; 3.16; 3.17; 3.18; 3.20; 3.21; A.2; A.3; A.4
Landsat 8	LC08_L1GT_053116_20141027_20170418_01_T2	3.6; 3.7; 3.8; 3.9; 3.10; 3.11; 3.12; 3.13; 3.15; 3.16; 3.17; 3.18; 3.20; 3.21; A.2; A.3; A.4
Landsat 8	LC08_L1GT_053116_20141112_20170417_01_T2	3.6; 3.8; 3.9; 3.11; 3.12; A.2; A.3; A.4
Landsat 8	LC08_L1GT_053116_20151014_20170403_01_T2	3.6; 3.7; 3.8; 3.9; 3.10; 3.11; 3.12; 3.13; 3.15; 3.16; 3.17; 3.18; 3.20; 3.21; A.2; A.3; A.4
Landsat 8	LC08_L1GT_053116_20151201_20170401_01_T2	3.6; 3.7; 3.8; 3.9; 3.10; 3.11; 3.12; 3.13; 3.15; 3.16; 3.17; 3.18; 3.20; 3.21; A.2; A.3; A.4
Landsat 8	LC08_L1GT_053116_20161203_20170317_01_T2	3.6; 3.7; 3.8; 3.9; 3.10; 3.11; 3.12; 3.13; 3.15; 3.16; 3.17; 3.18; 3.20; 3.21; A.2; A.3; A.4
Landsat 8	LC08_L1GT_053116_20170205_20170216_01_T2	3.6; 3.11; 3.7; 3.8; 3.9; 3.10; 3.16; 3.17; A.2; A.3; A.4
Landsat 8	LC08_L1GT_053116_20171104_20171120_01_T2	3.6; 3.11; 3.7; 3.8; 3.9; 3.10; 3.16; 3.17; A.2; A.3; A.4
Landsat 8	LC08_L1GT_053116_20180107_20180119_01_T2	3.6; 3.11; 3.7; 3.8; 3.9; 3.10; 3.16; 3.17; A.2; A.3; A.4
Landsat 8	LC08_L1GT_053116_20191025_20191030_01_T2	3.6; 3.7; 3.8; 3.9; 3.10; 3.11; 3.12; 3.13; 3.15; 3.16; 3.17; 3.18; 3.20; 3.21; A.2; A.3; A.4
Landsat 8	LC08_L1GT_053116_20201027_20201106_01_T2	3.2; 3.3; 3.4; 3.6; 3.7; 3.8; 3.9; 3.10; 3.11; 3.12; 3.13; 3.14; 3.15; 3.16; 3.17; 3.18; 3.19; 3.20; 3.21; A.1; A.2; A.3; A.4
Landsat 8	LC08_L1GT_053116_20201128_20201211_01_T2	A.2; A.3; A.4
MEaSUREs	antarctica_ice_velocity_450m_v2	3.2
Sentinel-2	2019-10-11-00/00_2019-10-11-23/59_Sentinel-2_L2A	1.2; 2.1; 3.1
WorldView-1	WV01_20110206_1020010011B44200_10200100119AE500_2m	2.4
WorldView-1	W1W1_20111219_1020010017965600_1020010018891300_seg1_2m_dem	A.1
WorldView-2	WV02_20101226_103001000842A200_1030010008338C00_seg1_2m_dem	A.1
WorldView-2	W2W2_20161105_1030010060790F00_1030010060C50A00_2m_lsf_seg1_dem	A.1
WorldView-3	WV03_20151125_1040010014396600_1040010015B86F00_2m	2.4

Table A.1. Imagery used in thesis and specific figures.

BIOGRAPHY OF THE AUTHOR

Ann M. Hill was born and raised in Minneapolis, MN. She attended Skidmore College in Saratoga Springs, NY where she became interested in Glaciology and consequently spent a semester at the University Center in Svalbard and a summer on the Juneau Icefield Research Program. She graduated with a Bachelor of Arts in Geosciences in May 2018. This interest in the cryosphere led her to pursue a graduate degree in Earth and Climate Sciences at the University of Maine. Ann is a candidate for the Master of Science degree in Earth and Climate Sciences at the University of Maine in August 2021.